OCS Study
BOEM 2024-034

Landfast Ice Climatology within the Arctic OCS

U.S. Department of the Interior
Bureau of Ocean Energy Management
Alaska OCS Region, Anchorage, AK

OCS Study
BOEM 2024-034

Landfast Ice Climatology within the Arctic OCS

August 2024

Authors:
Andrew R. Mahoney
Peter Bieniek
Seth Danielson
Andrew H. Einhorn
Kate S. Hedstrom
Joshua M. Jones
Thilo Klenz

Prepared under Cooperative Agreement M19AC00021
By
University of Alaska Fairbanks
Fairbanks, AK, 99775

U.S. Department of the Interior
Bureau of Ocean Energy Management
Alaska OCS Region, Anchorage, AK

DISCLAIMER

Study collaboration and funding were provided by the U.S. Department of the Interior, Bureau of Ocean Energy Management (BOEM), Environmental Studies Program, Washington, DC, under Agreement Number M19AC00021. This report has been technically reviewed by BOEM, and it has been approved for publication. The views and conclusions contained in this document are those of the authors and should not be interpreted as representing the opinions or policies of BOEM, nor does mention of trade names or commercial products constitute endorsement or recommendation for use.

REPORT AVAILABILITY

CITATION

Mahoney AR, Bieniek P, Danielson S, Einhorn AH, Hedstrom KS, Jones JM, Klenz, T (University of Alaska, Fairbanks, AK). 2024. Landfast ice climatology within the Arctic OCS. Anchorage (AK): U.S. Department of the Interior, Bureau of Ocean Energy Management. 121 p. Report No.: OCS Study BOEM 2024-034. https://espis.boem.gov/Final%20Reports/BOEM_2024-034.pdf.

ABOUT THE COVER

A recently refrozen lead at the landfast sea ice edge near Point Barrow on January 17, 2020. Photograph by A. Mahoney

ACKNOWLEDGMENTS

We are grateful to personnel at the U.S. National Ice Center (NIC) and the National Weather Service's Alaska Sea Ice Program (ASIP) for cooperation and assistance with questions regarding their sea ice chart products. We also thank the staff of Ukpeagvik Iñupiaq Corporation (UIC) Science in Utqiagvik, and Michael Tuzroyluck from the community of Point Hope for assistance with field activities. We are also grateful to Hilcorp for assistance with our attempted deployment of equipment near Deadhorse in 2020. Lastly, we thank Dr. Wilbert Weijer, from Los Alamos National Laboratory for providing the graphic used in Figure 3-37.

Contents

List of Figures

List of Tables

List of Abbreviations and Acronyms

ADCP	Acoustic Doppler current profiler
ASF	Alaska Satellite Facility
ARDEM	Alaska Regional Digital Elevation Model
ALOS	Advanced Land Observing Satellite
ASIP	Alaska Sea Ice Program
BOEM	Bureau of Ocean Energy Management
CIOD	Coupled ice-ocean driver
EM2024	The Einhorn-Mahoney (2024) landfast sea ice climatology dataset (1996–2023)
ERA5	European Centre for Medium-Range Weather Forecasts reanalysis version 5
GEBCO	General bathymetric chart of the oceans
GloFAS	Global Flood Advisory System
GLORYS	Global Ocean Physics Reanalysis
GNSS	Global Navigation Satellite System
IARPC	Interagency Arctic Research Policy Committee
InSAR	Interferometric synthetic aperture radar
ISRO	Indian Space Research Organization
JRA55	Japanese 55-year reanalysis
MMS	Minerals Management Service
M2014	The Mahoney et al., (2014) landfast sea ice climatology dataset (1996–2008)
MOM6	Modular ocean model version 6
NIC	National Ice Center
NASA	North Aeronautics and Space Administration
NISAR	NASA ISRO Synthetic Aperture Radar
NCEP	National Centers for Environmental Prediction
NWS	National Weather Service
OCS	Outer Continental Shelf
PAMS	Pan-Arctic MOM6-SIS2 model
PAROMS	Pan-Arctic Regional Ocean Modelling System
PALSAR	Phased Array L-band Synthetic Aperture Radar
ROMS	Regional Ocean Modelling System
SAR	Synthetic aperture radar
SIMB	Seasonal ice mass-balance buoy
SIS2	Sea ice simulator version 2
SLIE	Seaward landfast ice edge
SLP	Sea Level Pressure
SOM	Self organizing map
WMO	World Meteorological Organization
WOA	World Ocean Atlas

Abstract

The Arctic Ocean is currently undergoing a dramatic transition toward a seasonally ice-free state, with some of the greatest losses of sea ice in recent decades occurring in the Beaufort and Chukchi Seas. These changes are expected to have substantial impacts on landfast ice within the U.S. Arctic Outer Continental Shelf (OCS), which is used as a platform for hunting and travel by members of coastal communities and for exploration and production operations by the offshore oil and gas industry. Landfast ice also affects hydrographic processes in the nearshore zone and serves to protect the coast from mechanical erosion by waves. In this report we present findings from a coordinated series of tasks designed to improve our understanding of recent changes in landfast ice with the Arctic OCS and their potential drivers while improving our ability to simulate and forecast landfast ice. The individual tasks were:

Task 1: Development of a landfast ice climatology database for the BOEM Alaska OCS Region

Task 2: In-situ instrumentation of landfast ice

Task 3: Analysis of landfast ice change and atmospheric forcing

Task 4: Improved parameterization of landfast ice in an ice/ocean model

Task 5: Long term forecasting of landfast ice extent and seasonality

Task 6: Documentation of human impacts of landfast ice change

Task 7: Establishment of Scientific Review Board

Task 1 involved updating the results from two prior BOEM-supported research projects: MMS OCS Study 2005-068 (Mahoney et al., 2006) and BOEM OCS Study 2012-067 (Mahoney et al., 2012). To do so, we extracted landfast ice extent identified in ice charts prepared by the U.S. National Ice Center (NIC) and the National Weather Service's Alaska Sea Ice Program (ASIP). In doing so, we have created a 27-year climatology of landfast ice extent in the Arctic OCS[1], which refer to as the EM2024 dataset. This record shows there are significant trends toward later formation of landfast ice across the region. In the Chukchi Sea, we find landfast ice is forming an average 1.6 days yr^{-1} later, while in the Beaufort Sea the trend is 1.1 days yr^{-1}. Landfast ice in the Chukchi Sea also shows significant trends toward earlier break up (-0.6 days yr^{-1}), earlier ice-free conditions (-0.8 days yr^{-1}), and reduced landfast ice width throughout the winter (-0.09 to -0.27 km yr^{-1} from January to May). Trends toward reduced landfast ice width in the Beaufort Sea are primarily driven by an absence of stable extensions since 2006, but we caution that this result could be an artifact of the use of ice charts in the latter half of the record. As a result of these changes in width we note a significant reduction in the fraction of the Arctic OCS occupied by landfast ice over the duration of the EM2024 dataset. Over the first nine years (1996–2005) the median April landfast ice extent occupied 3.8% of the Arctic OCS area, where in the final nine year (2014–2024) this percentage had dropped to 2.0%.

We also explore the use of interferometric synthetic aperture radar (InSAR) as a more automatable approach for mapping landfast ice and extending the dataset into the future. Although our results indicate this would currently be problematic during the key stages of formation and breakup, we find that InSAR

---

[1] Please note that our study area includes small regions of the outer continental shelf in Canada and Russia adjacent to the U.S. Arctic OCS

products can provide useful information about different stability regimes within landfast ice, which may help improve our overall understanding of recent and future changes in landfast ice extent.

To further improve our understanding of the processes driving recent changes, we carried out a program of in-situ field observations of landfast ice. We investigated the specific role that storms may play in destabilizing landfast ice and we simulated 25 years of past landfast ice extent within the Arctic OCS by implementing a basal shear stress parameterization in a pan-Arctic coupled ice-ocean model. Despite relatively few successful deployments of in-situ instruments, we were able to collect valuable data capturing an abrupt change in sub-ice ocean temperature profile associated with a breakout event at Point Hope. The sudden increase in water temperature immediately below the ice shortly after it detached from the coast suggests that the ice was effectively sheltered from this warm water while it was still landfast. This demonstrates that the ocean heat flux below landfast ice may be substantially lower than below adjacent drifting ice and illustrates the importance of accurately resolving ocean processes in shallow water for modeling landfast ice behavior. However, we acknowledge that without coincident water temperature data from further offshore, we cannot rule out the possibility that the detachment coincided with the arrival of warm water in the region that would also have found its way under the landfast ice.

We explored the role of storms in promoting mid-season breakouts of landfast ice by compiling a catalog of breakout events from the EM2024 dataset and using this as a basis to track storms and analyze patterns of sea level pressure (SLP) in ERA5 reanalysis data. Composite SLP fields derived from days associated with breakout events shows significantly anomalous low pressures in the Bering Sea. A self-organizing map (SOM) analysis shows that the SLP pattern most commonly associated with breakout events corresponds to the occurrence of storms in the northern Bering Sea. Together, these results suggest that low pressure centers in the southeast Bering Sea may be a key component of some landfast ice breakout events, which is consistent with previous suggestions that storm-triggered shelf waves may destabilize landfast ice. These waves have length scales over 100 km and can propagate with phase speeds of >1,000 km day^{-1}, causing local sea level at the coast to fluctuate by tens of centimeters.

Lastly, we implemented a basal shear stress parameterization in a pan-Arctic coupled ice-ocean model to simulate the effect of ridge keels interacting with seafloor in shallow water. We refer this as the “PAMS” model, as explained in Section 2.7) We performed multiple models runs forced by JRA55-do atmospheric reanalysis data for the 15-year period from 1993 to 2017. Although the PAMS model is able to qualitatively reproduce the annual cycle of landfast ice extent, our results cannot be described as realistic simulations of landfast ice in the Arctic OCS over this period. Nonetheless, we anticipate continued development of the PAMS model and our results demonstrate that the Alaska Arctic OCS is an ideal test ground for refining model parameter choices and the EM2024 dataset represents a valuable benchmark for quantifying model performance.

1 Introduction

1.1 Note on prior related research

This project represents the extension of the landfast ice component of two prior projects supported by the Bureau of Ocean Energy Management (BOEM), or its predecessor the Minerals Management Service (MMS). Both of these prior projects were titled “Mapping and Characterization of Recurring Spring Leads and Landfast Ice in the Beaufort and Chukchi Seas”. The first project (MMS OCS Study 2005-068; Eicken et al., 2006) produced a climatology of landfast in the Beaufort and eastern Chukchi Sea from 1996–2004. Here we used the term climatology in the context of landfast ice to refer to a consistent multi-decadal dataset of landfast ice extent that allows the identification of key events with the annual cycle. The second project (BOEM OCS Study 2012-067; Mahoney et al., 2012) expanded the spatial domain of the landfast ice analysis to include a second study region encompassing the remainder of the Chukchi Sea and extended the overall time period up July 2008. In both of these previous studies, the extent of landfast sea ice was mapped through a systematic analysis of consecutive synthetic aperture radar (SAR) images. In this study we adopt the same two study regions and extend the timeline to July 2023 by incorporating landfast ice extent delineated in ice charts compiled by the U.S. National Ice Center (NIC) and the National Weather Service (NWS) Alaska Sea Ice Program (ASIP). See below for more details on study regions (Section 1.4) and data sources and methods for identifying landfast ice (Sections 2.1–2.4). This project exceeds the scope of the preceding work related to landfast ice by including a program of field observations (Section 2.5), a reanalysis-based study of storm impacts (Section 2.6), and a pan-Arctic ice-ocean modeling component designed to improve Arctic-wide simulation of landfast ice (Section 2.7). The modeling component is also builds on prior BOEM and MMS projects, including most recently “Development of a Very High-Resolution Regional Circulation Model of Beaufort Sea Nearshore Areas” (OCS Study BOEM 2018-018; Curchitser et al., 2018 and references therein).

1.2 Background

Landfast ice is an essential component of the coastal sea ice system and is found along coastlines wherever sea ice occurs. In the Arctic as a whole, landfast ice typically reaches an average annual maximum extent of 1.8 million km^2 (Yu et al., 2014), or approximately 12% of the total Northern Hemisphere wintertime sea ice cover. Acting as a floating extension of the land, it is the most accessible form of sea ice and the one most often encountered by people. Of particular relevance to BOEM, landfast ice serves as a platform for the oil and gas industry, which relies on ice roads across landfast ice to access nearshore production and exploration facilities (Masterson 2009; Potter et al., 1981). Additionally, members of Arctic coastal communities travel across landfast ice and hunt marine mammals and birds that are commonly found at its seaward edge (George et al., 2004; Laidre et al., 2015; Lovvorn et al., 2018). Additionally, landfast ice serves as an important habitat for ringed seals (*pusa hispida*; or *nachiq* in Iñupiat), which are uniquely adapted to thrive in landfast ice through their ability to create and maintain breathing and access holes (Smith et al., 1991) and polar bear (*ursus maritimus*; or nanuq in Iñupiat) who prey upon them (Pilfold et al., 2014).

Landfast ice also plays an important role in the sediment dynamics of coastal waters (Eicken et al., 2005) and can buffer the coast against the erosive action of waves (Lantuit and Pollard 2008; Ravens et al., 2023). By isolating the underlying ocean from wind mixing, landfast ice allows river plumes to extend farther than they would under open water or pack ice (Granskog et al., 2005; Ingram and Larouche 1987; Kasper and Weingartner 2015). In some cases, the hydrographic influence of landfast ice extends well beyond the coastal zone (Itkin et al., 2015), affecting the locations of upwelling such as in the Beaufort Sea (Pickart et al., 2009) and deep convection on the Eurasian Arctic shelf (Dmitrenko et al., 2005).

Landfast sea ice is typically a seasonal phenomenon in the Arctic, forming each fall and breaking up the following spring. A quantitative definition of the beginning and end of the landfast ice season is discussed in Section 2.2.5, but from hereon when we refer to the landfast ice season in general, we are considering the 304-day period from October 1 to July 31 during which landfast ice could conceivably be found within our study region. The seasonal maximum extent of landfast ice is largely controlled by coastal bathymetry (e.g, Mahoney et al., 2014 and references therein) and, consequently, most previous studies have found little or no change over time. One notable exception is the Chukchi Sea, where Mahoney et al., (2014) found that the annual maximum width of landfast ice reduced by an average of 13 km (~50%) between the periods 1973–76 and 1996–2008. However, the observed landfast ice season has been shortening throughout the Arctic as a result of later formation and earlier breakup. For example, ice charts from Russia's Arctic and Antarctic Research Institute (AARI) show a declining trend in Laptev Sea landfast ice duration of almost 3 d yr^{-1} (Selyuzhenok et al., 2015). Similarly, Canadian Ice Service charts show similar trends in the Alaska Beaufort Sea and Mackenzie Delta area, and a shorter landfast ice season throughout the Canadian Arctic Archipelago (Galley et al., 2012). In Alaska waters, the landfast ice season in the Chukchi and Beaufort Seas has shortened by approximately 38 days (~1.4 d yr^{-1}) and 53 days (~2 d yr^{-1}), respectively, between 1973–77 and 1996–2008 (Mahoney et al., 2014; Mahoney et al., 2012).

Due to its connection with other components of the changing Arctic system, landfast ice has been identified as a potentially valuable indicator of Arctic change for a variety of stakeholders, including the oil and gas industry and coastal communities (Mahoney 2018). However, despite the dramatic changes that have affected Arctic sea ice in the last decade (Fox-Kemper et al., 2021), there have been very few studies of landfast ice that document this period. To facilitate planning and ensure the safety of on-ice activities, there is an urgent need for updated information and improved ability to forecast the extent, stability, and seasonality of the landfast ice, particular along the U.S. Arctic coast, which have seen some of the most extensive changes in seasonal sea ice extent in recent years (Peng and Meier 2018).

1.3 Regional hydrography, bathymetry, and sea ice characteristics

The Chukchi and Beaufort Seas lie north of Alaska and together contain the entire U.S. Arctic outer continental shelf (OCS). Typically, Point Barrow, the northernmost point of the North American mainland, is taken as the demarcation between the two bodies of water, which have distinct hydrographic and bathymetric characteristics (Figure 1-1). The Chukchi Sea is dominated by a broad, shallow shelf (the Chukchi Shelf) mostly less than 60 m deep with shoals such as Hanna Shoal and Herald Shoal rising to around 20 m. In contrast, water shallower than 60 m in the Beaufort Sea occupies only a narrow strip less than 100 km from the coast. Most of the Beaufort Sea is more than 1,000 m deep and is part of the Canada Basin.

Figure 1-1 also shows the predominant current directions. In the Chukchi Sea, there is a net northward flow, which enters through Bering Strait and branches into different bathymetrically constrained currents (Ovall et al., 2021; Stabeno and McCabe 2023; Weingartner et al., 2005). The heat flux associated with this northward flow enhances the early loss of ice in the Chukchi Sea, particular in the vicinity of the primary currents illustrated in Figure 1-1 (Danielson et al., 2020a; Woodgate et al., 2010). In comparison, ocean circulation in the Beaufort Sea is dominated by the anticyclonic (clockwise) motion of the Beaufort Gyre, which transports some of the oldest and thickest ice in the Arctic from the region north of the Canadian Archipelago into the Beaufort Sea. This motion is driven by atmospheric circulation around a persistent region of high pressure (the Beaufort High). The strength of the Beaufort Gyre can vary from year to year and the ocean current and ice motion can sometimes reverse for periods of a few days. However, in winter the average ice drift is approximately parallel to the coastline.

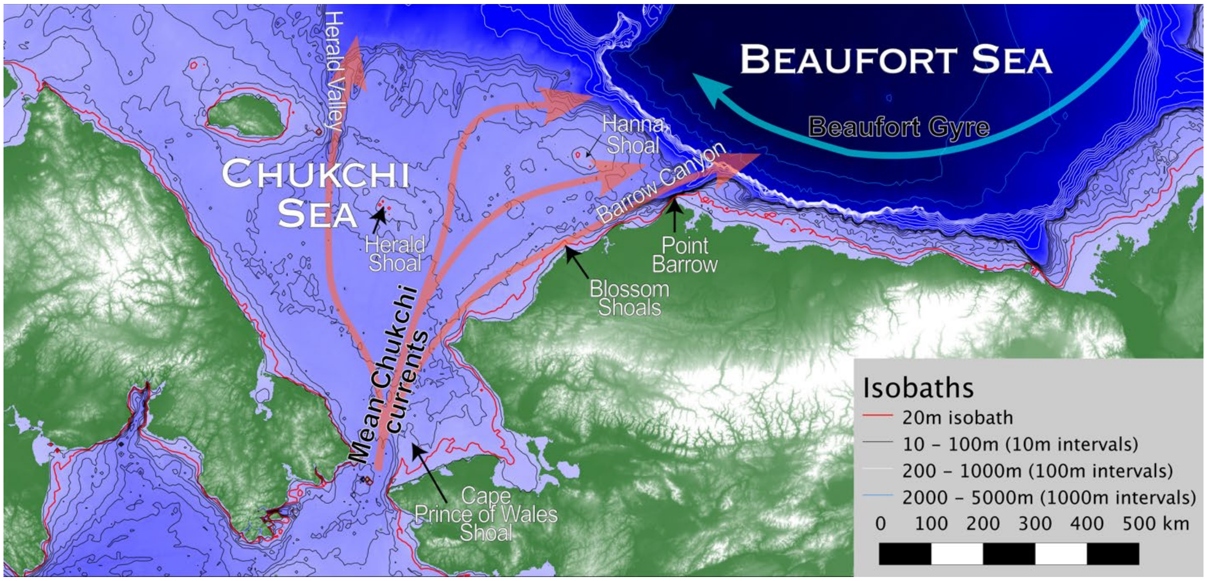

Figure 1-1: The bathymetry of the Chukchi and Beaufort Seas based on the Alaska Regional Digital Elevation Model (ARDEM), compiled by Danielson et al., (2015). The red contour indicates the location of the 20 m isobath. Colored arrows are schematic representations of mean surface currents, from Weingartner (2005).

The differences in bathymetry, hydrography, and ocean currents between the Chukchi and Beaufort Seas lead to marked differences in the character of sea ice in these two regions. The U.S. Beaufort Sea receives an influx of multiyear sea ice from the Canadian Arctic and, although a substantial fraction now melts before it can recirculate in the Beaufort Gyre (Mahoney et al., 2019), this multiyear ice can become incorporated in landfast ice along the Beaufort Coast. Multiyear sea ice is rarely seen very far south of Point Barrow in the Chukchi Sea, which typically has a thinner ice pack than the Beaufort Sea. This is due to the Chukchi Sea's more southerly location and the inflow of heat through Bering Strait, which delays freeze-up in the fall and promotes breakup in the spring. In addition, the orientation of the Beaufort and Chukchi Sea coastlines relative to the direction of prevailing winds induces a contrasting response of ocean and ice circulation behavior between the two regions.

1.4 Study regions

As introduced in Section 1.1, this study uses the same study region used in the previous BOEM study on landfast ice in the Arctic OCS (BOEM OCS Study 2012-067; Mahoney et al., 2012). This comprises a western region, occupying most of the Alaska Chukchi coast and the northern coastline of the Russian Chukotka Peninsula, and an eastern region extending from just west of Wainwright on Alaska's Chukchi coast to the Mackenzie Delta in Canada (Figure 1-2). For convenience, we will refer to the western and eastern regions as the Chukchi and Beaufort regions, respectively. We recognize that these regions do not align with conventional definitions of the Chukchi and Beaufort seas, but they are effectively a legacy of our former work, and we adopt them for historical consistency. By way of explanation, the Beaufort region corresponds to the study region for the first SAR-derived landfast sea ice climatology project (MMS OCS Study 2005-068; Eicken et al., 2006), while the Chukchi region corresponds to the area that was added to the study region in the subsequent project (BOEM OCS Study 2012-067; Mahoney et al., 2012).

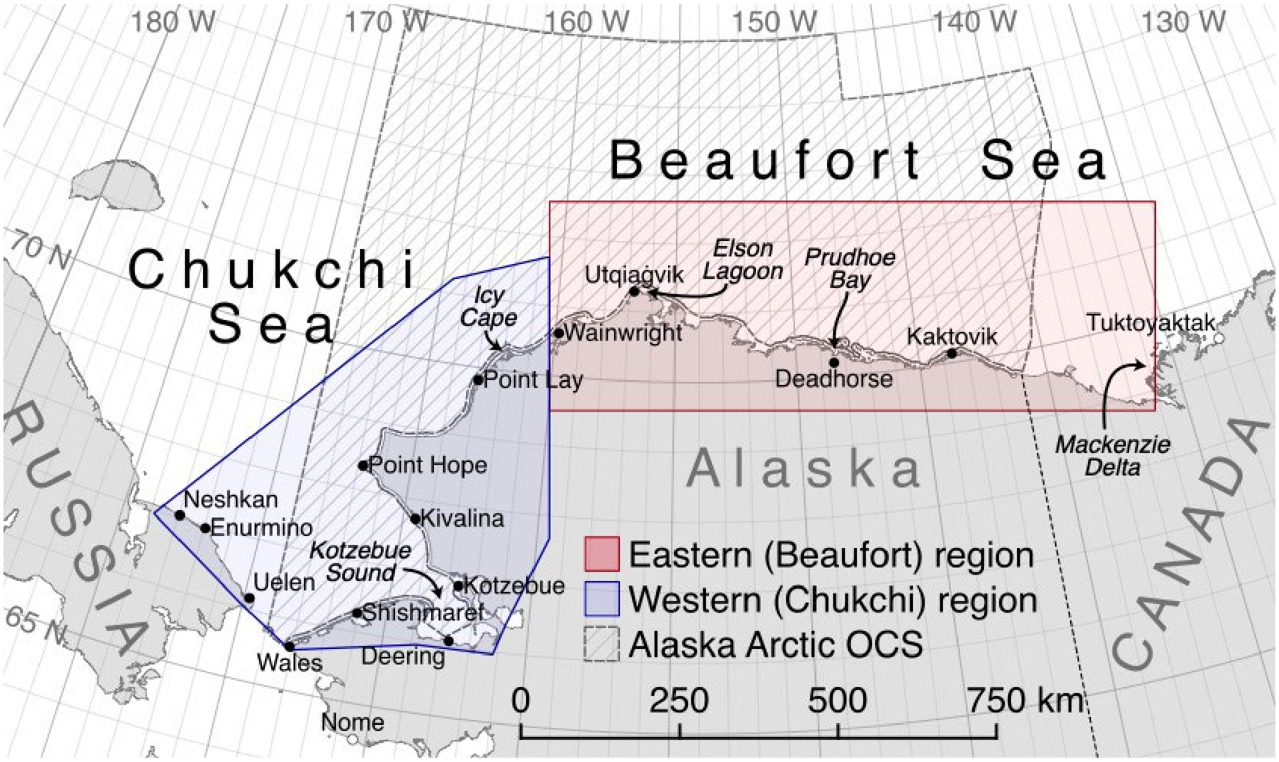

Figure 1-2: Map showing extent of the study areas used for analysis of landfast sea ice extent in this project. See Sections 1.1 and 1.4 for an explanation of the origins of these study regions.

2 Data and methods

2.1 Existing landfast ice extent data sources

2.1.1 Rationale for using existing data sources

In this study, we combine three separate observation-based data sources that partly overlap in time to produce a single continuous climatology of landfast ice extent. These data sources are described below in Sections 2.1.2 to 2.1.4, but two features they all share is that they each identify landfast ice extent without any additional interpretation and they existed prior to this study commencing. This allowed us to compile 16 more years of data in considerably less time than it took to create the previous 12-year dataset. Due to gaps in satellite data availability in the intervening years, it would have more challenging to produce a continuous dataset had we attempted to analyze landfast ice extent ourselves from original imagery.

2.1.2 M2014 landfast ice data

As noted in Section 1.1, the aforementioned BOEM OCS Study 2012-067 project (Mahoney et al., 2012) resulted in a dataset of landfast ice extent spanning the Chukchi and Beaufort Seas from 1996–2008. From here on, we refer to this dataset as the M2014 dataset, in reference to the authorship and date of the peer-reviewed publication in which it was first presented and described (Mahoney et al., 2014). In brief, the M2014 dataset was produced by analyzing sequences of SAR imagery to identify landfast sea ice based on the following two criteria:

1. *Sea ice that is contiguous with the shoreline*
2. *Sea ice that lacks detectable motion for ~20 days*

Each image sequence consisted of three SAR mosaics spanning a total time period of approximately 20 days. Motion was detected through visual inspection assisted by the generation of a composite gradient difference image, that highlighted edges that remained constant across all three SAR images. This resulted in the delineation of the seaward landfast ice edge (SLIE) for each 3-mosaic sequence. The region between each SLIE and the coastline was then rasterized to create a binary image that defined the extent of landfast with a pixel resolution of 100 m. A mosaic of SAR images spanning the entire study area typically requires images acquired several days apart and so separate mosaics were assembled for the Chukchi and Beaufort study regions. Accordingly, SLIEs were also delineated separately for these two regions. Although each sequence of 3 SAR mosaics spanned ~20 days, SLIEs were delineated every ~10 days. As a result, there were typically 27–28 SLIEs delineated in each landfast ice season in the Beaufort region. In the Chukchi region, where the landfast ice season is somewhat shorter, each season was typically represented by 26–27 SLIEs. Up until early 2008, the SAR mosaics were compiled exclusively from Radarsat imagery. However, Radarsat ceased to be available March 2008 and from this point on we used Envisat SAR instead. This resulted in fewer mosaics overall for the 2007–08 season, with some being incomplete. In total, the M2014 dataset consists of 316 SLIE images for the Chukchi region and 331 SLIE images for the Beaufort region.

2.1.3 U.S. National Ice Center (NIC) ice charts

The National Ice Center (NIC) produces operational ice charts primarily used for navigation in and around icy seas. These ice charts are archived in SIGRID-3 format at the National Snow and Ice Data Center (U.S. National Ice Center 2022). These ice charts were provided as shape files with vector features containing attributes corresponding to sea ice characteristics identified by NIC analysts. The NIC analysis used a variety of data including SAR, visible, and infrared satellite imagery to identify sea ice characteristics such as ice concentration, stage of development, ice age, and ice thickness. When the analysts were identifying a vector feature as landfast, the analyst primarily used SAR to identify areas which exhibit no motion over multiple days. In addition to a lack of motion, NIC analysts looked for characteristic shapes within landfast ice in Alaska such as ridges, which appear bright in SAR images, separated by smooth ice. Areas with homogenous characteristics were outlined by vector features with attributes corresponding to each characteristic. Throughout the duration of the dataset, the attributes and attribute values vary. Of particular importance to this study, prior to March of 2006 the attribute used to identify landfast ice was the form variable CF. When the CF variable was set to "0899" the analysis identified the area as landfast ice. We found this definition to be inconsistent within the ice charts resulting in the exclusion ice charts prior to March of 2006 in our analysis. From March 2006 onward NIC adopted the World Meteorological Organization (WMO) "Egg Code" which defined standard attributes and attribute values corresponding to specific sea ice characteristics. The Egg Code identifies landfast ice using the primary form (FP or FA) attribute with a value of "08". Multiple instances were found where the primary form attribute indicated the vector feature was landfast ice (FP = 08), but also indicated the ice concentration was less than 100%. This error was attributed to mislabeling by the analyst thus we implemented a secondary attribute requirement for a vector feature to be considered landfast. In addition to the primary form being 08, the ice concentration must represent 100% concentration, total concentration (CT) is 92 or 93. In addition to the varying attribute values throughout the NIC ice charts, the frequency at which an ice chart was released also changed.

From 2003 through the 2013–2014 season NIC produced one ice chart for the whole Arctic every 2 weeks. The frequency increased to weekly in 2014. When retrieving the digitized ice charts from NIC an issue occurred where the 2017–2018 and 2018–2019 seasons were incomplete, such that charts we absent during March–July 2018 and January–April 2019. Since this represented a substantial fraction of the season, both seasons were excluded in their entirety. Additionally, we identified a small number of charts (24 in total) that contained polygons designated as landfast ice, but were not contiguous with the coast.

These affected the Beaufort region only, so they were excluded on a regional basis. In total, the NIC ice charts yielded 501 SLIE images in the Chukchi region and 477 SLIE images in the Beaufort region.

2.1.4 Alaska Sea Ice Program (ASIP) ice charts

The National Weather Services'(NWS) Alaska Sea Ice Program (ASIP) produced digitized ice charts for the Beaufort and Chukchi Seas from 2007–2023 (Alaska Sea Ice Program (ASIP) 2023). The area which ice charts extend is 55–85° N and 150°E–105°W. These ice charts were provided as shape files with vector features containing attributes corresponding to sea ice characteristics identified by ASIP analysts. At ASIP, analysts use multiple satellite-based sensors, including SAR, visible bands, and infrared, to identify landfast ice. The ASIP analyst look for no sea ice motion in response to winds or currents. Sea ice which exhibited no motion and was contiguous with the coast was classified as landfast. In general, the analysts waited to classify immobile sea ice attached to the coast until it achieves a thickness of 4–12 inches. This additional parameter implemented by the ASIP analyst was done since the majority of ASIP ice chart users require information with the intent to travel on or through the sea ice. Similar to the NIC ice charts, the attributes which defined sea ice characteristics changed during the duration of the dataset. Prior to January 1, 2015, ASIP used the attributes "Form" and "Label Age" to identify vector features as landfast. A vector feature was identified as landfast when the Form attribute was "Fast," and Label Age was "Shorefast." From 2015 onward, ASIP used the WMO Egg Code where landfast ice was identified by the primary form "FP" was "08". We added the secondary attribute requirement of total concentration "CT" represents 100% (92 or 93) similar to the NIC ice charts. The year 2015 also marked a change in the frequency with which ASIP charts were produced. Up to the end of 2014, charts were produced on a two-to-four-day interval on Mondays, Wednesdays, and Fridays. From 2015 onward ice charts were produced daily. In total, the ASIP ice charts consisted of 4,322 SLIE images in the Chukchi region and 4,323 SLIE images in the Beaufort region.

Table 2-1: Number of SLIE images produced in the Beaufort and Chukchi regions and landfast ice seasons for which SLIE were produced from each dataset

Dataset	Number of SLIE Images in Beaufort Region	Number of SLIE Images in Chukchi Region	Landfast ice Seasons
M2014	331	316	1996–2008
ASIP	4,323	4,322	2007–2023
NIC	477	501	2005–2017, 2019–2022

2.2 Standardized analysis of SLIE data

2.2.1 Overview of SLIEalyzer tools

SLIEalyzer is the name we have given to a package of software tools written in Matlab that allow standardized analysis of SLIE data from each dataset and subregion. The underlying code and associated documentation can be found at https://github.com/armahoney/SLIEalyzer and key processes are described in detail in the following subsections. However we will first provide an overview of the inputs provided to SLIEalyzer, the primary processing involved and the data products it produces.

As its primary input, SLIEalyzer takes a series of GeoTIFF files containing SLIE images together with a configuration file that specifies details such as the size of the images, the number seasons to be analyzed and the locations of ancillary files necessary for the analysis. These ancillary files include GeoTIFFs providing a coast mask and bathymetry as well as ASCII files specifying coast vector information (see Section 2.2.3) and subregion boundaries. In practice, SLIEalyzer is configured so that it just needs to be given the name of the dataset to be analyzed. The first step in the analysis is the calculation of landfast ice width in each SLIE image using a predefined set of quasi shore-normal “coast vectors” (see Section 2.2.3). This facilitates temporal analysis of the data including the determination of key events in the annual landfast ice cycle (Section 2.2.5), the derivation of monthly landfast ice extents (Section 2.2.5) and the detection of mid-season breakout events (Section 2.2.7). At the same time that width of the landfast ice is measured, SLIEalyzer also determines the water depth at the SLIE based on a data from the ARDEM bathymetric digital elevation model (Danielson 2013; Danielson et al., 2015) regridded to study region at 100-m resolution.

2.2.2 A note on assigning dates to SLIE observations

Assigning a specific date to a SLIE observation is not entirely straightforward, since each observation spans a multiple-day period of time, rather than a specific day. In the M2014 data set, each SLIE represents the extent of landfast ice identified in three consecutive SAR mosaics, each approximately 10 days apart, spanning a total period of approximately 20 days. Mahoney et al., (2014; 2007) were able to narrow down the appropriate date for individual points along a SLIE by determining whether the landfast ice was advancing or retreating at the location. If the SLIE was advancing, then the observation ought to correspond to a date toward the beginning of the ~20-day period, while if it was retreating then the appropriate date should be toward the end of the period. However, there are a number of reasons to reconsider this approach for the updated climatology developed in this project.

First, this approach becomes problematic when applied to a gridded landfast ice product, since the SLIE might advance or retreat at different locations during the same period. The approach also depends on a perfectly consistent dataset in which there should not be any instance of a local minimum in landfast ice extent lasting fewer than 20 days. We found a small number of cases where this occurs (<1%), indicating a minor level of inconsistency in our subjective technique for determining of landfast ice extent. Lastly, unlike the M2014 dataset, the chart-based products we are using post-2008 do not use an overlapping set of three consecutive mosaics.

For these reasons, we have chosen not to follow our previous approach for assigning dates to SLIEs. Instead, we simply assign a date to each SLIE based on the rounded-up mid-date of the time period over which SLIE is defined. For the M2014 data, this will be mid-point between the dates of the first and last mosaic, while for the NIC- and ASIP-derived datasets, we will use the mid-point between the publication date of the ice chart and the day following the publication of the previous chart. For daily ice charts, this will equate to the publication date of the chart.

2.2.3 Measurement of landfast ice width

The first step in the process of combining landfast ice extent data from the three different datasets described in Section 2.1 is to measure the width of landfast ice width from a series of fixed points along the coastline. The approach we follow is described in detail by Mahoney et al., (2014; 2007) and involves the use of a discrete set of vectors approximately normal to the coastline (Figure 2-1). Hereinafter we refer to these vectors, as “coast vectors” and we defined 8,892 of them in total: 6,956 in the Chukchi region and 1,936 in the Beaufort region. Collectively, they serve to establish a common 1-dimensonal curvilinear coordinate scheme for defining the position of SLIE in terms of its distance from the origin of each vector. This distance equates to the width of the landfast and is generally defined by the seawardmost pixel of landfast intersected by each vector. In places where the SLIE or the coastline are particularly convoluted, a coast vector may intersect the SLIE more than once and, in such cases, the width measurement will therefore include some region on open water or non-landfast ice. In the deep embayment of Kotzebue Sound, it is also possible for a coast vector to intersect landfast ice attached to the opposite shoreline. In this case, the landfast width is defined by the pixel on the landfast ice edge that is farthest from the coast.

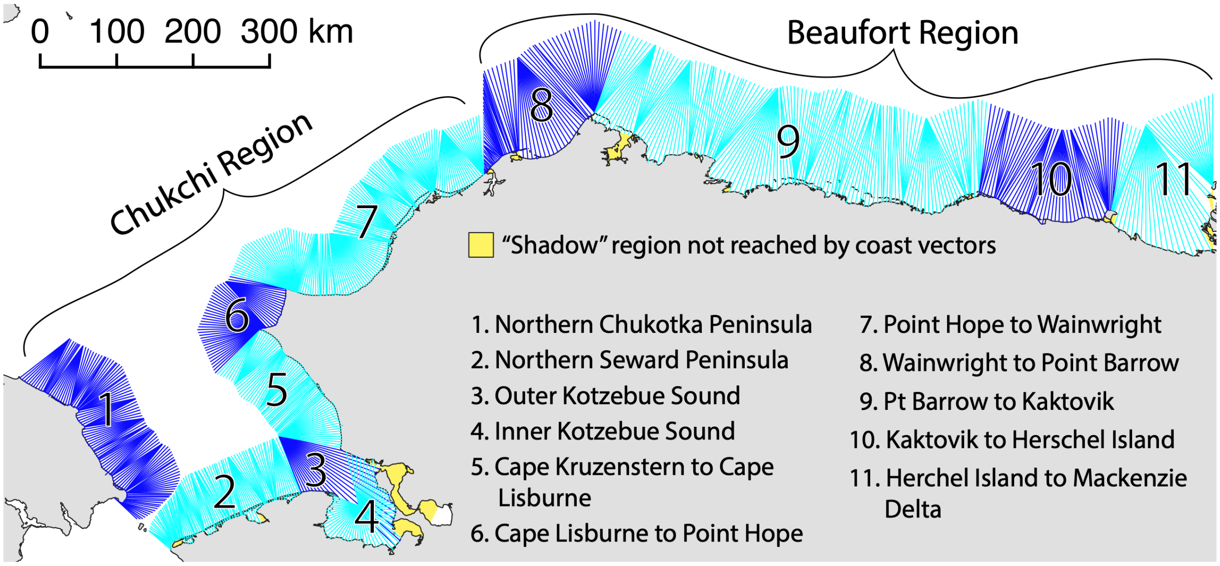

Figure 2-1: Pre-defined set of approximately coast-normal vectors (hereinafter known as coast vectors) used to measure the width of landfast ice within our study area. Note that the coast vectors are further group into subregions used in later analysis.

Notwithstanding the few exceptions described above, the measurement of landfast along the predefined set of coast vectors illustrated in Figure 2-1 allows us to reconstruct the SLIE using a fixed set of 1-dimensional coordinates. This greatly simplifies the task of interpolating over time, which is essential for producing a dataset with a common daily sampling frequency (see Section 2.3). The computation of landfast ice width also allows us to interpolate across missing segments of data and facilitates temporal analysis of the data as described in Sections 2.2.5–2.2.7. By grouping coast vectors into subregions, we can also analyze spatial variability in landfast ice. For some of the analysis that follows, we identified 11 different subregions based on primarily on the orientation of the coastline and separated by prominent headlands or other coastal features. These subregions also used in the process reconstructing the SLIE from the measurements of landfast ice width (Section 2.2.4).

2.2.4 Reconstruction of SLIE images from landfast ice width measurements

In what is effectively the inverse process of measuring landfast ice width, we can use the coast vectors to reconstruct a SLIE image from landfast ice width measurements. This is useful for creating statistically derived SLIE images, such as monthly means (Section 2.2.6) or interpolating SLIE data over time (Section 2.3). The coast vectors allow the width measurements to be converted into an ordered sequence of spatial coordinates defining the vertices of the SLIE. By joining this SLIE with the coastline, we define a polygon that can be filled and rasterized to create a SLIE image of the same format as those used as inputs to SLIEalyzer. The coastline and associated land mask used here and throughout the study is the same as that used in the original landfast climatology project (MMS OCS Study 2005-068; Eicken et al., 2006). It is a 100-m resolution rasterization of the National Geospatial Intelligence Agency (NGA)'s World Vector Shoreline product in an Alaska Albers NAD83 projection (EPSG:3338).

This process is relatively straightforward, but there are a few details of worth noting. First, it is necessary to group coast vectors into contiguous segments of coast so that the SLIE does not bridge discontinuities in the coastline like Bering Strait. This is accomplished using the subregions illustrated in Figure 2-1. Second, we also had to apply a special rule for subregions 3 (Outer Kotzebue Sound) and 4 (Inner Kotzebue Sound), where there are intersecting coast vectors. In such cases, averaging or interpolation on a per-vector basis can result in different SLIE locations for each set of coast vectors. We overcome this by using the mid-points between the two SLIEs in these regions. Lastly, there are certain "shadow" zones (shown in yellow in Figure 2-1), which represent waters where the coast vectors do not reach due to convolutions in the coastline. In SLIE images reconstructed from landfast ice width measurements, these regions are treated as unknown.

2.2.5 Key events within the landfast ice cycle

Following the approach of Mahoney et al., (2014; 2007), we determine the timing of three key events in the annual cycle of landfast ice based on seasonal timeseries of width (Figure 2-2):

First landfast ice on coast (first ice). We define the first occurrence of landfast ice as the date of the first non-zero width measurement that immediately precedes a width measurement ≥500 m. This allows us to exclude any early season, short-lived landfast ice that fails to reach a width of at least 500 m before detaching.

Breakup. We use the term breakup to refer to the season-ending retreat of landfast ice that results in a coastline free of landfast ice. We define the timing of breakup as the time of most rapid retreat during the tail end of the season once the landfast ice width ceases to make any increases.

Last landfast ice on coasts (last ice). Similar to the definition of first ice above, we define the last occurrence of landfast ice as the last non-zero width measurement after the last measurement >500 m. Short-lived landfast events are less common at the end of the season than at the beginning, but we exclude them for consistency.

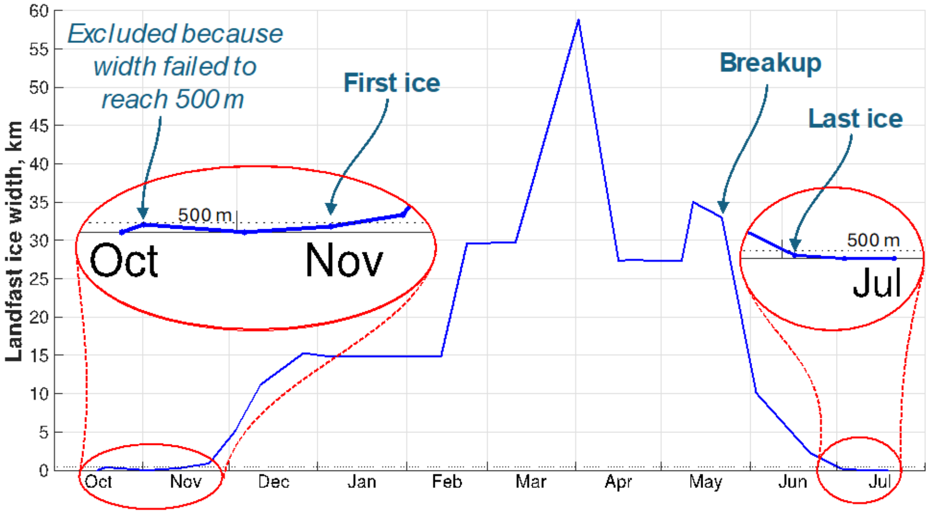

Figure 2-2: One annual cycle of landfast ice width at a location in the Beaufort Sea, illustrating the definition of the three key events (first ice, breakup, and last ice).

On occasion, the annual cycle of landfast ice width measured at a coast vector does not fit the example shown in Figure 2-2 and the determination of one or more key events fails. For example, the determination of first ice will fail if there is already landfast ice present at a location at the first observation for a given landfast ice season. Similarly, if the record for a season ends before the landfast ice width reaches zero at a location, the determination of last ice will fail. Also, if the tail end of the landfast ice season is not well defined (i.e. landfast ice width does not decline monotonically) it may not be possible to uniquely determine the timing of breakup. Overall, these make up a small percentage of all cases as listed in Table 2-2.

Table 2-2: Percentage of cases where calculation of annual landfast ice event date failed

Region	First ice	Breakup	Ice free
Chukchi	6.6%	6.5%	6.5%
Beaufort	8.0%	0.5%	0.5%

In addition to these three key annual events derived from the landfast ice width data, we also derived the dates of the onset of freezing and thawing air temperatures using data from National Center for Environmental Prediction (NCEP) Reanalysis 1 data (NCEP 2023), following the approach of Mahoney et al., (2014; 2007). This involved creating timeseries of air temperature at origin point of each coast vector by interpolating the 4x daily gridded near surface (sigma level 0.995) air temperature data product. For each year, we then find the first day with a daily mean temperature below 0°C that was also the first day of a 15-day period with a mean temperature below 0°C. The onset of thawing was calculated in a similarly using positive temperatures.

2.2.6 Calculation of monthly SLIE extents

Using the mid-point dates assigned to each SLIE observation (Section 2.2.2) we binned landfast ice width measurements by calendar month and computed the minimum, median, mean, maximum and lower and upper quartile values for each coast vector. The width values were then used to reconstruct monthly SLIE images for each statistical measure, following the approach described in Section 2.2.4. Since these images are reconstructed from width measurements, the shadow zones are coded as unknown.

2.2.7 Identification of mid-season breakout events

We use the term breakout to refer to mid-season events in which the landfast ice undergoes a sudden and substantial retreat. It is important to note that breakout events are different from breakup (Section 2.2.5), which occurs toward the end of every season. Breakout events are identified from the landfast ice width measurements based on four criteria, listed below and illustrated in Figure 2-3:

1. *The landfast ice width decreases by at least one third of the median width for a given coast vector*
2. *The width of remaining ice is less than 50% of climatology median width*
3. *The event affects at least 25 consecutive coast vectors (~5 km)*
4. *The event occurs between January and April (typically the most stable period)*

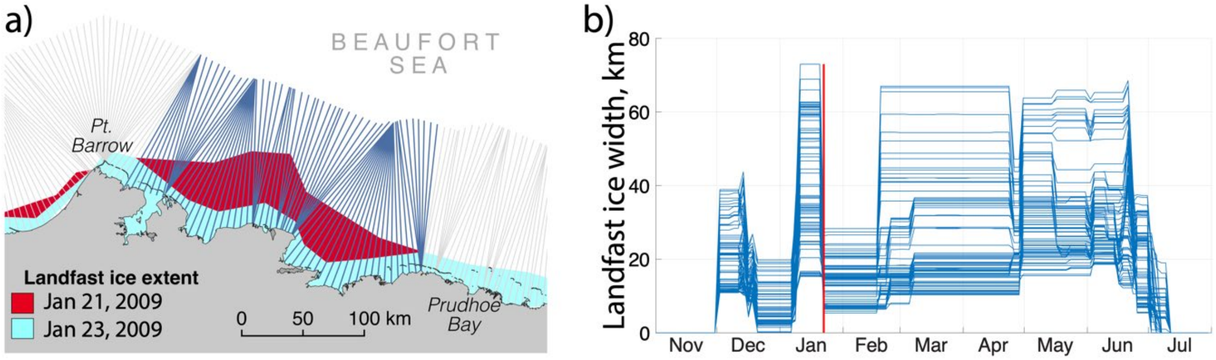

Figure 2-3: Illustration of detection of a breakout event in Beaufort Sea in January 2009. a) Spatial extent of landfast ice from January 21 and January 23, 2009. Areas of retreat over this time are shown in red. Coast vectors within the breakout region are shown in blue. Those outside are shown in gray. Note that the red region to the west of Pt Barrow does not qualify as a breakout event because the reduction in landfast ice width is insufficient. b) Seasonal variation in landfast ice width measurements along the coast vectors within the region of breakout. The timing of the breakout is illustrated by the vertical red line.

Using these criteria, we developed a catalog of individual breakout events that lists the time, location, and size of each breakout, which is specified as total area, coastline length, and mean width. We treat all breakouts as separate events, even if events overlap in space and occur within the same season. In total, there are 133 such events, but in most cases the spatial extents of the two events are substantially different (in 75% of cases there is <50% overlap in extent along the coast). The analysis that follows does not require that breakouts are strictly independent events and instead benefits from a more exhaustive catalog. Also note that when calculating the size of a breakout, we include any contiguous regions that retreated over the same time period, but did not meet criteria 1–3 above. For example, in the two breakout regions illustrated in Figure 2-3, criteria 1 and 2 may not be met for all coast vectors, particular at either of their coastal extent where the breakout width tapers. However, each region contains at least 25 consecutive coast vectors that do meet these criteria, then the region as whole is treated as a breakout.

2.3 Compilation of extended landfast ice climatology

We combined the M2014, ASIP and NIC datasets into a single 27-year climatology, which will refer to from hereinafter as the EM2024 dataset, in reference to its two primary authors (Einhorn and Mahoney) and the year in which it was completed. Compilation of the EM2024 dataset was a three-step process performed on the measurements of landfast ice width (Section 2.2.3) derived from each parent dataset individually. Since each dataset was sampled at a different rate, the first compilation step was to interpolate all observations to a consistent, daily sampling interval. This was achieved through a single nearest neighbor scheme, such that if there was no observation on a given date, we assign the value from the closest date when there was an observation. We applied this interpolation over time to data from each coast vector to create staircase-like timeseries that effectively preserve the underlying temporal resolution, which is important when computing the occurrence dates of key events (Section 2.2.5). In addition to unifying sampling rates between datasets, interpolation also allows us to fill-in missing data from incomplete SAR mosaics in M2014 dataset (Section 2.1.2) and missing polygons in ASIP and NIC ice charts (Sections 2.1.3 and 2.1.4).

The second step in the compilation process is to apply a running 20-day minimum filter to the ASIP and NIC datasets. As noted in Section 2.1.2, the definition of landfast ice used in the M2014 dataset includes an implicit 20-day minimum, so this step allows us to achieve a similar definition across all three datasets. The third and final step is to combine the datasets into a single timeseries following a relatively simple set of rules, as illustrated in Figure 2-4. The first rule is simply to use the M2014 when available, since this is most consistent and well understood of the three datasets. After the 2007–08 season, we then take either the average of the ASIP and NIC datasets, if both are available, or just the ASIP data when the NIC charts are unavailable. As with the other steps, this averaging takes place on a per-coast vector basis. Daily SLIE images are then reconstructed from the resulting landfast ice width data, as per the method described in Section 2.2.4.

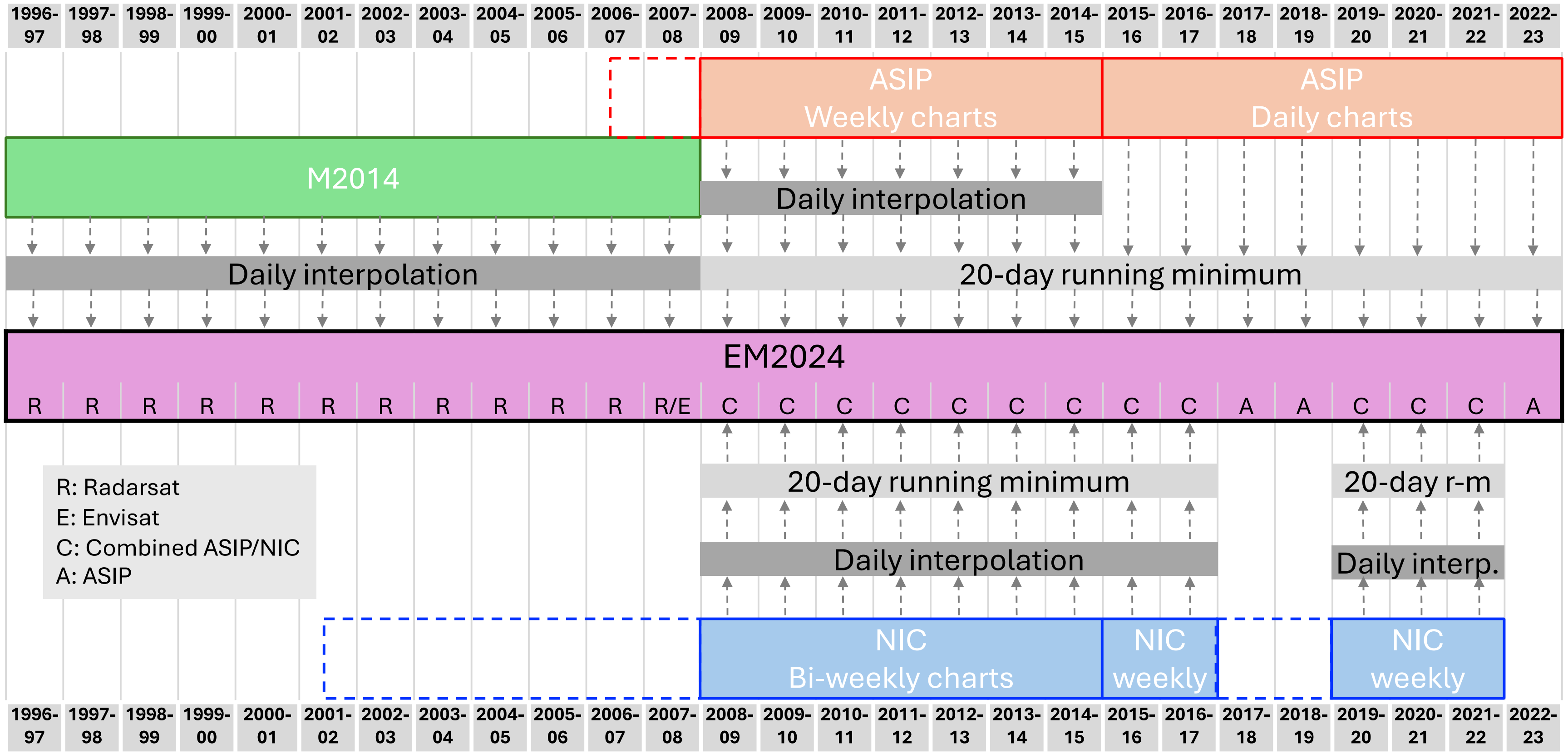

Figure 2-4: Schematic illustrating how the EM2024 dataset is compiled from the three "parent" datasets.

2.4 InSAR-based detection of landfast ice

2.4.1 Overview of InSAR and application to sea ice

Synthetic aperture radar interferometry (InSAR) holds promise for both automated identification of landfast ice and understanding small-scale deformation that it can undergo. InSAR uses SAR images taken from approximately the same location in space at different times to measure the surface displacement which occurred between images. Any application of InSAR requires that the surface being imaged remains sufficiently coherent between acquisitions. In the case of a moving surface like sea ice, this requires the total motion is less than half image resolution, such that at least half of any given pixel represents the same ice surface in both images. At typical drift speeds of up to 0.5 ms^{-1} and typical SAR resolutions on the order of 10–100 m, this is only achievable over mobile pack ice when images are acquired within a few minutes of each other. However, over relatively immobile landfast ice, InSAR can be applied to images acquired weeks or even months apart. In most situations motion of tens of m would preclude ice from being classified as landfast.

The Alaska Satellite Facility (ASF) Vertex portal hosts Sentinel-1 A/B SAR images that can be paired to perform interferometry. Within the Vertex portal, the Short Baseline Subset tool allowed for the selection of Sentinel-1 A/B SAR pairs within specified perpendicular and temporal baselines ranges. SAR pairs were limited to pairs with less than a 300 m perpendicular baseline and a 12-day temporal baseline. A 6-day temporal baseline is possible when using both the Sentinel-1A and Sentinel-1B in tandem. However, this was not possible for the whole study period due to Sentinel-1B encountering an issue. The 12-day temporal baseline allowed for the same satellite to be used to acquire the primary and secondary images in the SAR pairing. In addition, we applied a seasonal filter from November to July of 2017–2022 as landfast ice is not typically present within the study region outside of this period. A total of fourteen reference scenes were chosen to span the extent of the study area, with 7 required to cover the Chukchi and 7 to cover the Beaufort regions. After these constraints were applied to the Sentiel-1 dataset 2,084 SAR pairs were identified from March 2017 to July 2022. All images were taken in the interferometric wide swath (IW) mode. The Sentinel-1 single look complex in IW mode has a spatial resolution and pixel spacing of 3.1×22.7 m and 2.3×14.1 m, respectively. Each pixel is then multi-looked, or averaged, by 20 looks in the range direction by 4 looks in the azimuth direction to reduce speckle noise and improve coherence. Multi-looking by 20×4 looks reduced the resolution to 160 m which is down sampled to a pixel spacing of 80×80 m. Each SAR pairing was processed by ASF using the HyP3 toolbox (Hogenson et al 2016), which produces interferometric data products from the SAR pairings. For this study we used the coherence GeoTIFF and wrapped interferometric phase GeoTIFF for analysis.

2.4.2 Interferometric coherence and relationship to landfast ice extent

Coherence in interferometry describes the signal similarity of coregistered pixels in the primary and secondary SAR image pairs. In the context of sea ice, reductions in coherence are attributed to drifting sea ice, large amount of deformation, surface roughness change, and surface composition changes. Coherence has been used to identify and delineate landfast sea ice from pack ice by thresholding the normalized coherence values. Using Advanced Land Observing Satellite (ALOS) Phased Array L-band Synthetic Aperture Radar (PALSAR) data, Meyer et al., (2011) determined pixels with a normalized coherence value greater than 0.1 were landfast ice. The choice of an L-Band sensor, wavelength of 23.62 cm, allowed for longer time between acquisitions and be more robust to late season melting while maintaining coherence. PALSAR repeated orbit paths every 45 days.

This study used SAR pairs acquired by Sentinel-1, a C-Band (5.54 cm), SAR satellite which repeated its orbit every 12 days. The shorter wavelength requires less change to reduce coherence. However, the reduction of the repeat orbit interval is assumed to offset the lower threshold for reductions in coherence. This offset allowed for the use of the same normalized coherence threshold, 0.1, to distinguish landfast ice from mobile pack ice. On occasion, pack ice returns pixels or small clusters of pixels in the speckle which achieve the 0.1 coherence threshold but are not contiguous with the coast nor landfast ice. We remove these false positive identifications of landfast ice using morphological filtering. This operation removed small clusters of coherent pixels while filling 'pinholes' of low coherence within the landfast ice. Pixels did not achieve the 0.1 threshold outside of the land area prior to December. In addition, suspected surface melting or flooding caused complete loss of coherence in May or June. Interferograms from the Beaufort region maintained coherence through the end of May while the Chukchi region would lose coherence in early to mid-May. Previous studies using Sentinel-1 experienced similar losses of coherence and constrained their data to interferograms from March to May (Dammann et al., 2019). In accordance with our coherence-based definition of landfast ice, pixels must have a coherence higher than 0.1 and be contiguous with the coast; we constrained our analysis to December, January, February, March, April, and May.

InSAR products were grouped and mosaicked to generate monthly images for the whole study area. This created 24 InSAR-derived SLIE images for the months of December to May over the period 2017–2021. We then used the SLIEalyzer toolbox (Section 2.2.1) to measure landfast ice width for each of these SLIE images and compute monthly means for the whole InSAR period (2017–2021). The monthly landfast ice width measurements using coherence were then compared to corresponding data from the EM2024 dataset for the same period.

2.4.3 Measurement of apparent strain

InSAR allows for different deformation regimes within landfast ice to be calculated. Dammann et al., (2018) and Fedders et al., (2024, in press), show that it is possible to estimate 2-dimensional strain of sea ice from the phase gradient under certain circumstances, but without a constellation of satellites to provide multiple look directions, a universal approach remains elusive. Hence, to use InSAR to derive information about the stability of landfast ice, we simply assume that ice deformation of any kind results in a phase gradient and therefore the magnitude of the phase gradient is inversely related to the stability of the landfast ice.

To calculate the interferometric phase gradient, we treat each interferogram as a matrix and convolve it with kernels representing finite differences in the x and y directions. Using a 4-pixel long kernel provides the calculates the difference in phase between pixels spaced 3 pixel-widths apart. The phase gradient in the x direction using (Equation 2-1) and the y direction (Equation 2-2):

$$\boldsymbol{\frac{\partial \phi}{\partial x} \approx \frac{\phi_{(m,n)} - \phi_{(m-3,n)}}{3\Delta x}} \qquad (2\text{-}1)$$

$$\frac{\partial \phi}{\partial y} \approx \frac{\phi_{(m,n)} - \phi_{(m,n-3)}}{3\Delta y} \qquad (2\text{-}2)$$

Where ϕ is the interferometric phase, m and n are pixels indices in the x- and y-direction, respectively, and Δx and Δy are the corresponding pixels dimensions. Four-pixel kernels were found to capture the phase gradient while mitigating spurious pixels of rapid phase change associated with areas of low coherence.

The cyclic nature of interferometric phase means that there are artificially high phase gradients when the phase wraps between 2π and 0 at the end of a "fringe". To account for this, we follow the work of Libert et al., (2022) and convert the wrapped phase gradient to complex number using Equations 2-3 and 2-4, which invoke Euler's formula. In this form, the real and imaginary components of the phase gradient are represented using continuous sine and cosine functions that are insensitive to the discontinuities at phase wraps between 2π and 0. The magnitude of the unwrapped phase gradient in both the x and y direction can be found by taking the inverse tangent of the imaginary and real components of the complex wrapped phase gradient (Equation 2-5 and 2-6). The total unwrapped phase gradient, $|\nabla\phi|$, is the Pythagorean sum of the phase gradients in both x and y directions (Equation 2-7).

$$a_x + ib_x = e^{\mathrm{i}\frac{\partial\phi}{\partial x}} = cos\frac{\partial\phi}{\partial x} + i\ sin\frac{\partial\phi}{\partial x} \qquad (2\text{-}3)$$

$$a_y + ib_y = e^{\mathrm{i}\frac{\partial\phi}{\partial y}} = \cos\frac{\partial\phi}{\partial y} + i\ sin\frac{\partial\phi}{\partial y} \qquad (2\text{-}4)$$

$$\frac{\partial\phi}{\partial x} = \tan^{-1}(b_x, a_x) \qquad (2\text{-}5)$$

$$\frac{\partial\phi}{\partial y} = \tan^{-1}(b_y, a_y) \qquad (2\text{-}6)$$

$$|\nabla\phi| = \sqrt{\frac{\partial\phi_u}{\partial x}^2 + \frac{\partial\phi_u}{\partial y}^2} \qquad (2\text{-}7)$$

A 2π difference in ϕ between any two pixels corresponds to half a radar wavelength, λ=0.0564 m, difference in the line-of-sight displacement of the ice at those two pixels. Here, we define the term apparent strain, $\in_a$, to describe the magnitude of the horizontal gradient in line-of-sight displacement:

$$\in_a = \frac{\lambda}{4\pi}|\nabla\phi| \qquad (2\text{-}8)$$

Since Sentinel-1 is a side looking radar with a non-zero incidence angle, $\in_a$ is sensitive to both horizontal and vertical displacement of the ice surface. However, in the horizontal plane, it is only sensitive to motion in the look direction. Under certain circumstances, it is possible to identify cases when surface strain is dominated by either horizontal or vertical strain and, with sufficient constraint on the mode of deformation (e.g., radial divergence or simple shear), it is possible to resolve the 2D strain field through inverse modeling (Fedders et al., 2024, in press). However, this typically only applies inside sheltered lagoons (when strain is dominated by thermal processes) or when additional information about ice motion is available. Hence, it would be impracticable to apply this approach throughout our study domain and so instead we use $\in_a$, as a conservative approximation of the total amount of strain between acquisitions. We should be cautious about using $\in_a$ to infer stress accumulation in the ice, but we should expect areas experiencing more deformation should exhibit higher values of $\in_a$ than those regions that are sheltered from such activitiy, particularly when averaged over multiple interferograms. We therefore use $\in_a$ here as a proxy for the relative stability of the landfast ice.

The apparent strain images were sorted by year and month, with the date of the primary image in the SAR pair being the date of reference. Spatial coverage of Sentinel-1 is inconsistent within the study region. This resulted in different numbers of interferograms created for each reference scene. In addition, the fourteen SAR reference scenes overlapped in certain areas, also causing different numbers of interferograms to be valid during each time period. After aligning all valid apparent strain images, a per pixel count of images with a valid pixel was created. This value was then used to average the apparent strain value for this pixel on a per month basis from 2017–2022. By counting the number of valid pixels, we ensured areas which were occupied by landfast ice for multiple interferograms are not counted differently than places with few valid areas of landfast ice. Monthly average apparent strain values were calculated for December, January, February, March, April, and May for pixels with valid identification of landfast ice.

2.4.4 Regions used to define stability thresholds

Dammann et al., (2019) used InSAR to define 3 categories of stability within landfast ice, based on a qualitative analysis of the density and orientation of interferometric fringes: bottomfast; stabilized; and non-stabilized. Bottomfast ice is the most stable of these categories and occurs in water shallow enough where the entire water column freezes, and the sea ice is frozen to or is resting on the seafloor. This depends on the ice thickness (or, more precisely, the draft of the ice), but in our study region bottomfast ice will be found in waters up to approximately 1.5 m deep (Pratt 2022). In interferograms, bottomfast ice was identified based on "*No identifiable phase difference from the adjacent land*". Stabilized landfast ice is found seaward of the bottomfast ice zone where the ice is floating but held in place by islands or grounded pressure ridges. Dammann et al., (2019) identified stabilized ice based on "*Poorly defined, widely spaced fringes, or abruptly reduced fringe spacing compared to offshore ice*". Lastly, non-stabilized ice includes all landfast seaward of any island or grounded ridge and was identified according to "*Well-defined fringe orientation or patterns*". Here, we derived phase gradient thresholds to quantitatively define these stability categories.

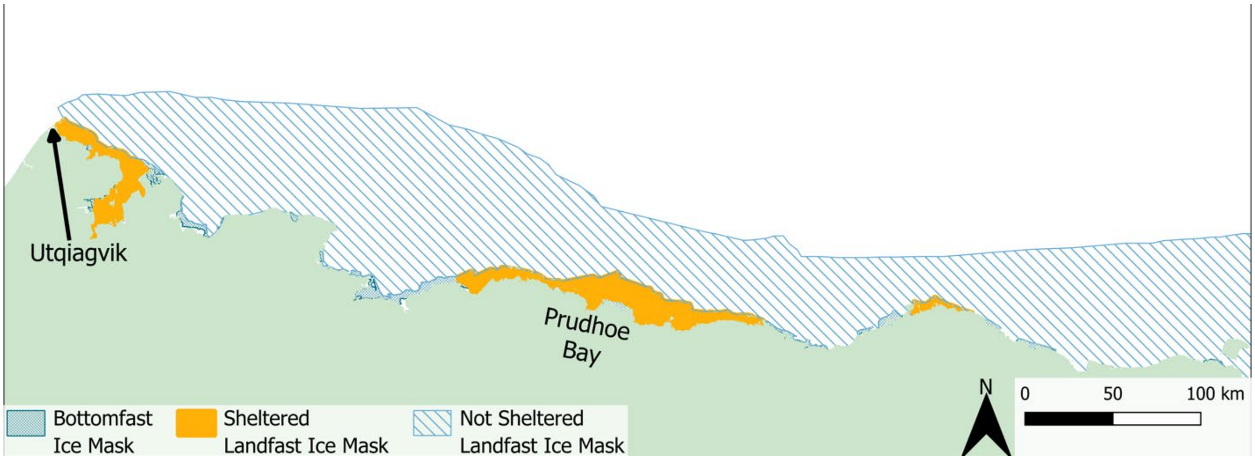

Figure 2-5: Spatial extent of bottomfast, sheltered, and not sheltered landfast ice masks.

Landfast ice that is anchored by an oceanward grounded feature is more stable than landfast ice oceanward of a grounded feature. Grounded pressures ridges do not necessarily occur in the same location during each season, leading to different extents of the stabilized region defined by Dammann et al., (2019). Unlike grounded pressure ridges, barrier island locations do not vary between seasons. Barrier islands shelter the landfast ice shoreward of its location and act similar to a grounded ridge when the embayment fills with landfast ice. We created spatial masks for landfast ice related to the landfast ice location to barrier islands:

1. *Bottomfast ice: The same extent identified by Dammann et al., (2019) (blue hashed areas in Figure 2-5)*
2. *Sheltered ice: Area shoreward of a barrier island or barrier island chain, not including areas of bottomfast ice (orange areas in Figure 2-5)*
3. *Not-sheltered ice: Landfast ice oceanward of a barrier island or barrier island chain (light blue areas in Figure 2-5)*

The maximum extent of bottomfast ice extent along the Beaufort coast varies little enough between seasons (Pratt 2022) that we can use the bottomfast ice extent defined during April of 2017 by Dammann et al., (2019) to identify the areas which are likely bottomfast ice during April of all seasons. The landfast ice in the sheltered region is guaranteed to have grounded landfast ice oceanward of its location due to the presence of the barrier islands. The not-sheltered region may include areas of landfast ice stabilized by grounded pressure ridges, but will include all the non-stabilized areas seaward of any stabilizing features.

2.5 In-situ field observations

2.5.1 Seasonal ice mass balance buoys (SIMBs)

Cryosphere Innovations 3rd generation Seasonal Ice Mass balance Buoys (SIMB3s) were deployed to measure the growth and melt of landfast ice (Figure 2-6). The SIMB3 is equipped with a downward-looking snow sounder to measure the distance, z_s, to either the snow surface, or the ice surface if there is no snow present. By independently measuring the initial distance from the snow sounder to the ice surface, z_{s0}, when the buoy is deployed, this allows the SIMB3 to observe changes in the snow depth, H_s, according to:

$$H_s = z_{s0} - z_s \qquad (2\text{-}9)$$

In summer, after the snow pack has melted away and $z_s > z_{s0}$, this sensor measures of surface melt of the ice. A second sounder looks upward below the ice and measures the distance to the ice bottom, z_b. The ice thickness, H_i, is then given by:

$$H_i = z_{ss} - z_{s0} \text{ for } z_s \leq z_{s0} \qquad (2\text{-}10)$$

$$H_i = z_{ss} - z_s \text{ for } z_s > z_{s0} \qquad (2\text{-}11)$$

where z_{ss} is the distance between the two sounders, which is equal to 4.05 m.

The SIMB is also equipped with a chain of temperature sensors, spaced at 2-cm intervals, that record the temperature profile from the ocean to the atmosphere through the ice and any snow present. There is a shielded air temperature sensor at the top of the buoy and a water temperature sensor at the bottom. Data are telemetered every hour via an Iridium satellite connection to servers at CryosphereInnovations, where they are available in real time.

SIMBs were deployed in landfast ice near Point Hope and Utqiagvik, Alaska (Figure 2-7) between 2020 and 2024 (Table 2-3). An attempt was made in early 2020 to deploy a SIMB in Foggy Island Bay, near Deadhorse, Alaska but the attempt was unsuccessful due to unanticipated failure of an ice auger used for the making the necessary hole in the sea ice. A subsequent storm prevented an immediate return to the site and the unfolding COVID-19 pandemic prevented further attempts in 2021 and 2022. Eventually, the SIMB was returned to Fairbanks, Alaska and redeployed in Utqiagvik to replace a buoy that was damaged during retrieval. This buoy was then damaged by a polar bear in 2022, prematurely ending its data record. The SIMB deployed at Utqiagvik in 2024 survived one polar bear encounter shortly after deployment, but was unrecoverably damaged by a second encounter on May 10.

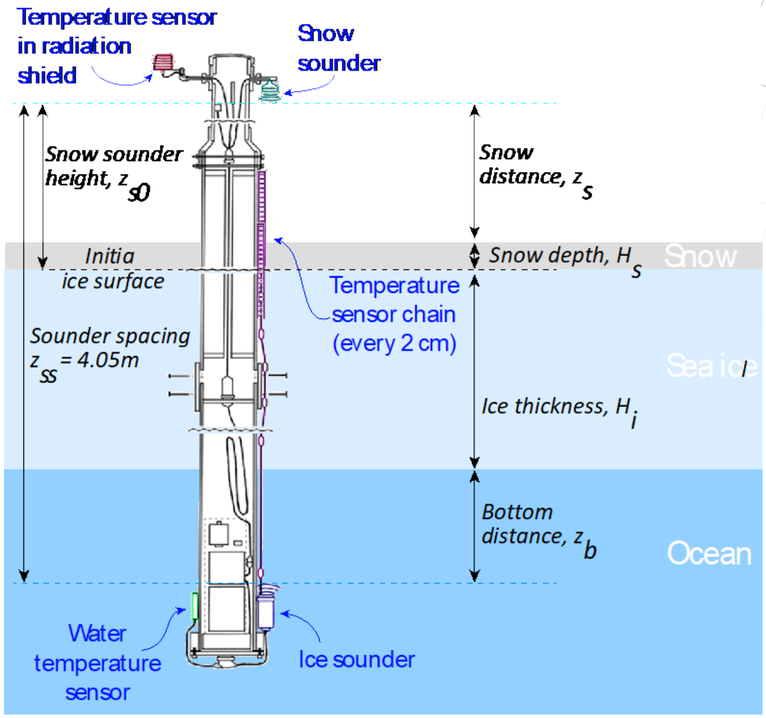

Figure 2-6: Schematic showing deployment of SIMB3 and derived measurements.

Figure 2-7: Map showing locations of SIMBs deployed during this project.

Table 2-3: Deployment notes for instruments deployed in landfast ice

Season	Point Hope	Utqiagvik	Foggy Island Bay
2020	SIMB: Mar 7 – Jun 20 ADCP: lost	No deployments	Aborted SIMB & ADCP deployments
2021	No deployments	SIMB: Mar 4 – Jun 8	No deployments
2022	SIMB: Feb 12 – May 26	SIMB: Jan 28 – Mar 4 ADCP: Jan 28 – Jun 22	No deployments
2023	No deployments	No deployments	No deployments
2024	No deployments	SIMB: Feb 3 – May 10	No deployments

2.5.2 Ice tethered acoustic Doppler current profilers (ADCPs)

To measure the vertical profile of currents beneath landfast ice, we deployed 1,200 kHz acoustic Doppler current profilers (ADCPs) in an ice-tether configuration adjacent to SIMBs (Figure 2-8). Suspending the ADCP close to the seafloor looking upwards allows measurement of the current profile near the ice-water interface with a vertical resolution of 5 cm. However, as noted in Table 2-3, we were only able so successfully deploy two such ADCPs. The first of these was deployed as planned in Point Hope, but due to the COVID-19 pandemic we were unable to return to the community to recover it before the landfast ice detached from the coast. We requested assistance from local residents to search the seafloor for in the vicinity of the initial deployment, but the weather never aligned with scheduling windows and so the instrument and its data were lost. We were therefore only able to collect one season of under-ice current data at Utqiagvik, in 2022. In this instance, the ADCP was deployed at a depth of 6.5 m in approximately 7 m of water, below sea ice that was initially 0.8 m thick.

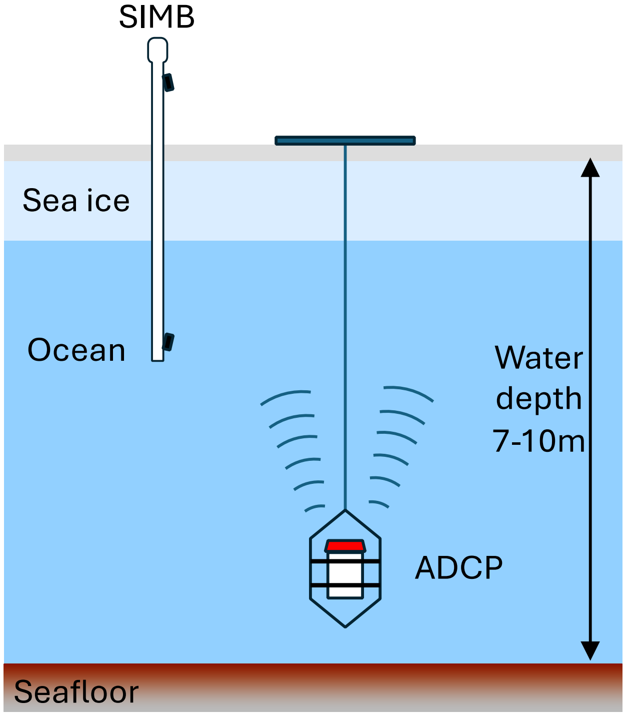

Figure 2-8: Schematic illustrating upward-looking ice-tethered deployment of an ADCP adjacent to a SIMB.

2.6 Atmospheric analysis

2.6.1 Reanalysis data products

This study utilized the European Centre for Medium-Range Weather Forecasts reanalysis version 5 (ERA5; Hersbach et al., 2020) for the analysis of storms, which is publicly available at the Copernicus Climate Data Store (https://cds.climate.copernicus.eu/). ERA5 is a gridded (0.25 by 0.25 degree resolution) reanalysis dataset that uses a weather model to assimilate station and satellite remote sensing products to generate hourly gridded observations of various meteorological variables. This reanalysis was selected as it has shown good performance relative to similar products from other modeling centers in the Arctic and Alaska (Avila-Diaz et al., 2021; Bachand and Walsh 2022; Graham et al., 2019).

For our analysis we obtained hourly sea level pressure (SLP), 10-m wind speed and wind direction spanning 1991–2023 (Hersbach et al., 2023). This includes years prior to those covered by the EM2024 landfast ice dataset, but overlaps well with the most recent climate normal period of 1991–2020 used by the U.S. National Weather Service and the World Meteorological Organization. This 30-year climatology provides a simple long-term average of each parameter over its appropriate timescale (i.e., monthly or daily). Anomalies were produced by subtracting out the long-term average climatologies based on the 1991–2020 climate normal period.

2.6.2 Cyclone tracking

Cyclones, often referred to interchangeably as storms, are areas of low pressure that can bring high winds and precipitation. These storm systems are often responsible for many extreme events in coastal regions of Alaska such as the ex-Typhoon Merbok in September 2022 that brought substantial impacts from coastal erosion and flooding. These storms can be tracked either subjectively (i.e., by visual inspection of synoptic weather maps) or following an objective method using computer software. In this study we used the objective storm identification and tracking algorithm described by Zhang et al., (2004). This algorithm is designed to track storms on gridded SLP from atmospheric reanalysis at 6 hourly and 2.5 degree temporal and spatial resolution, respectively. For our study we applied this algorithm to the ERA5 SLP gridded fields at 6 hour increments and regridded via bilinear interpolation to 2.5 degrees. The result is a data set that provides the time, location, and central pressure of each cyclone identified.

To identify links between typical patterns of storm conditions and the occurrence of landfast ice breakout events, we used the results of a Self-Organizing Map (SOM) algorithm. SOM is a methodology that uses unsupervised neural networks to identify patterns in data (Kohonen 1989; 1990). In our analysis, SOMs were used to identify common patterns of SLP in the Alaska region (i.e., synoptic pattern types), each of which being tied to specific days during the period of analysis (each day of the period belongs to a SOM node). The SOM method has been previously used to identify synoptic pattern types for Alaska (e.g., Cassano and Cassano 2010; Cassano et al., 2017; Glisan et al., 2016; Hartl and Stuefer 2020). In this study we applied the Python MiniSOM algorithm (Vettigli 2018) to all of the daily average SLP anomaly fields from the ERA5 reanalysis for January–April over 1997[2]–2023 to match the period of the breakouts database. The SLP data were regridded to an equal area, 50×50 km grid and grid points with elevations greater than 500 m were masked to avoid artifacts stemming from the calculation of SLP at high elevations. Although we could have avoided the need to mask these regions by using reference pressure level (e.g., 850 hPa) for the SOM analysis, we used SLP for consistency with the cyclone tracking. Our analysis used a 4 by 5 SOM map, which provided a set of 20 different possible synoptic map types.

---

[2] Since breakouts are defined as only occurring between January and April and the EM2024 dataset begins in October 1996, the first year in the breakout catalog is 1997.

2.7 Pan-Arctic modeling of landfast sea ice

2.7.1 Selection and configuration of Pan-Arctic MOM6-SIS2 (PAMS) model

Previous work using a Pan-Arctic Regional Ocean Modelling System (PAROMS) (Curchitser et al., 2018; Danielson et al., 2016; Danielson et al., 2020b) demonstrated that the annual cycle of landfast ice extent in the Chukchi and Beaufort Seas could realistically be simulated with Lemieux et al.'s (2016; 2015) parameterization for basal shear stress resulting from the interaction between ridge keels and the seafloor in shallow water. However, PAROMS was found to be less well suited for multi-decadal model runs of similar duration to our expanded observational climatology of landfast sea ice. Specifically, it developed drifts in the temperature and salinity of the deep ocean that diverged from the known property values over extended integration times. At the same time, other partners in the modeling community were moving toward turning the world-class Modular Ocean Model v6 (MOM6) climate model (Adcroft et al., 2019) into a regional ocean model for its improved numerical schemes, including more efficient time-stepping. We have since discovered that the deep temperature drifts are sensitive to the restratification parameterization used, which is not something that is currently available in PAROMS.

Accordingly, for this study we chose the MOM6 ocean model, with the Sea Ice Simulator v2 (SIS2) sea ice model (Adcroft et al., 2019; Ross et al., 2023). This choice required that we set up a new integration domain covering the Arctic and some of the marginal seas around the Arctic (Bering Sea, Hudson Bay, etc.). The model was developed at roughly 12 km horizontal resolution for computational efficiency and for efficient testing, though a 6-km version of the same model formulation is in development and can be run later if a higher-resolution is required. Due to the very small scales of the eddies in the Arctic, true eddy resolving is beyond our abilities for this pan-Arctic domain. The 1-km or less nested model (including sea ice) is a Regional Ocean Modelling System (ROMS) capability that does not yet exist for SIS2. Having ice open boundary conditions would involve considerable development effort on top of

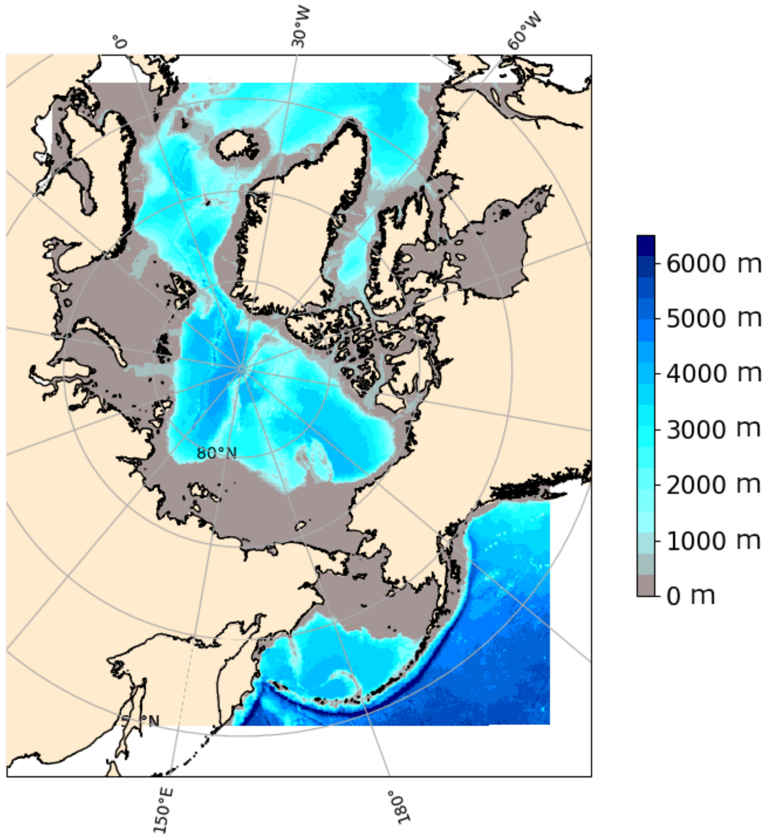

Figure 2-9: Model domain and bathymetry for the PAMS model used in this study.

what was done for the ocean open boundary conditions. As a result of the aforesaid limitations, the PAMS model we have implemented here is limited to a horizontal resolution of 12 km.

Note that we have chosen to mask out the Sea of Okhotsk as it is not connected to the rest of the domain. This domain has open boundaries on all lateral sides, and its bathymetry and extent are shown in Figure 2-9. Some of the notable parameter choices for MOM6 are shown in Table 2-4.

Table 2-4: Notable parameter choices for MOM6 model used in this study

Parameter	Value	Reference
Vertical coordinate	75 layer z*	(Adcroft et al., 2019)
Baroclinic time step	600 s	-
Thermodynamics, coupling and biogeochemistry time step	1,800 s	-
Model time period	1993–2017 (or 2019)	-
Vertical mixing		
Planetary boundary layer parameterization	ePBL	(Reichl and Hallberg 2018)
Shear mixing	Jackson	(Jackson et al., 2008)
Bottom boundary layer mixing efficiency	0.0	-
Internal tidal mixing	Polzin	(Polzin 2009)
Submesoscale restratification parameterization	Bodner, coefficient of 0.3	(Bodner et al., 2023)
Lateral mixing		
	Biharmonic Smagorinsky: SMAG_BI_CONST = 0.06, AH_VEL_SCALE = 0.01	(Griffies and Hallberg 2000)
Boundary conditions		
Sea level and barotropic velocity	Flather scheme	(Flather 1976)
Baroclinic velocity	Radiation and nudging (3 day inflow, 360 day outflow time scales)	(Marchesiello et al., 2001); (Orlanski 1976)
Tracers	Reservoirs with 3 km length scales	-
Minimum depth	5 m	-
Maximum depth	6,500 m	-
Tidal SAL coefficient	0.094	-
Equation of state	WRIGHT_FULL	(Wright 1997)
Opacity scheme	3-band with chlorophyll from COBALT	(Manizza et al., 2005)

The SIS2 sea ice model has the option to call the CICE Consortium Icepack library (Hunke et al., 2024) for ice ridging, which we have found to be helpful for getting realistic ice thickness fields in the central Arctic basin. In addition, we have ported two different landfast ice parameterizations from CICE into SIS2: those of Lemieux et al., (2016; 2015) and Dupont et al., (2022), though all the results described below were derived using only the latter, at the recommendation of the science review board. In brief, the Lemieux studies assumed idealized triangular ridges that scaled with the mean thickness in a grid cell and applied a basal shear stress where the keel depth of these ridges exceeded the water depth. By comparison, Dupont et al's (2022) approach takes advantage of the sub-grid ice thickness distribution to probabilistically estimate the interaction of deep-keeled ice with the seafloor, which can also have sub-grid roughness. Here, we use bathymetry from the general bathymetric chart of the oceans (GEBCO) 2020 (GEBCO Compilation Group 2020) and apply the method of Adcroft (2013) for estimating seafloor roughness. Notable parameters used (i.e., differing from the global model of Adcroft et al., 2019) for the ice are shown in Table 2-5. The SIS2 model has a split-explicit timestep, with the thermodynamics updating on the slow ice timestep and the ice dynamics updating on the fast ice timestep. The fast ice timestep of 2.1 s is needed to resolve the elastic waves of the elastic-viscous-plastic rheology (Bouillon et al., 2009; Hunke and Dukowicz 1997). Note that, in this particular context, the term “fast” is used to mean rapid or quick, rather than stationary or attached.

Table 2-5: Notable sea ice parameters used in the SIS2 model

Parameter	Value	Reference
Number of ice categories	10	-
Slow ice timestep	900 s	-
Timestep ratio for fast ice solver	432	-
Yield curve ellipticity	1.5	-
Ridging	Yes	-
Ridge participation	old	(Thorndike et al., 1975)
Ridge redistribution	old	(Hibler 1980)
Landfast ice parameterization	ITD	(Dupont et al., 2022)
Transmute ice	Yes, at “northern” edge	-

2.7.2 Model forcing

The PAMS model is forced at the surface with winds and other atmospheric fields from the Japanese 55-year Reanalysis (JRA55-do) (Tsujino et al., 2018). The bulk fluxes are computed by the sea ice model and passed to the ocean via the coupler. For river forcing, the Global Flood Awareness System (GloFAS) product is remapped to all the coastal ocean points and applied as a fresh water input, similar to rain. It is given a salinity of zero and a temperature matching the 10-m air temperature. For the Gulf of Alaska, we replace GloFAS with a high-resolution (1-km) validated runoff product from Hill et al., (2015).

The model initial conditions are interpolated from the 1/12-degree Global Ocean Physics Reanalysis (GLORYS) fields (Copernicus Marine Service Information 2023). This includes temperature, salinity, free surface, horizontal velocities and the ice thickness and concentration. GLORYS is also used for the ocean lateral boundary conditions, applied daily on all four open boundaries. The boundary conditions are those of Flather (1976) for the barotropic flows and a combination of radiation and nudging to GloFAS for the baroclinic velocities. The temperature and salinity boundary conditions are applied via the tracer reservoirs. In MOM6, each open boundary has a data structure containing fields on that open boundary segment, including a reservoir for each tracer in which values are mixed in from values inside the model if the flow is directed outward or from external values if the flow is directed inward. The user provides lengthscales for each segment for how large the “reservoir” is for both the inflow and outflow cases, i.e., the reservoir can be large with a long memory of resident values, or it can be minute and easily overwritten with the incoming values.

The sea ice does not have open boundary conditions and sees the domain boundaries as walls. However, there is a TRANSMUTE_SEA_ICE option which we are using to turn ice into fresh water when it approaches the southern boundaries near Greenland and Kamchatka to prevent it from accumulating there. We are currently nudging to global monthly sea surface salinity climatology. This is only applied where there is no sea ice and is used to help correct some salinity biases observed in the Bering Sea. The model has tides, coming from both the open boundaries and an internal body force option. The boundary tides are interpolated from a global TPXO simulation (Egbert and Erofeeva 2002) as part of the Flather boundary condition. In both cases, we are including 10 tidal constituents, 4 semi-diurnal (M2, S2, N2, K2), 4 diurnal (K1, O1, P1, Q1), and 2 longer period tides (MF and MM).

2.7.3 Parameterization of basal shear stress

A basal shear stress term to represent the interaction between pressure ridge keels and seafloor was first introduced by Lemieux et al., (2016; 2015) to allow for ice to become landfast in shallow waters. In this scheme, the momentum equation includes an extra bottom drag term that acts in opposition to the resultant horizontal stress when the ice is deep enough to interact with the local bottom. The maximum magnitude of this stress is determined by mean ice thickness, the mean water depth, and two parameters defining simplified triangular shapes of pressure ridge keels. One advantage of this approach is that the landfast ice parameterization applies to the mean ice thickness in the cell and is therefore suitable even for a model with a single ice category. However, many sea ice models now allow for multiple ice categories in each grid cell, with some memory of the thickness distribution. Hence, to make use of that additional information Dupont et al., (2022) designed a probabilistic landfast ice parameterization that considers both the ice thickness distribution, $g(H_i)$, and the water depth distribution, $b(H_w)$. The basal shear stress, $\tau_{b_{max}}$, is calculated by integrated the product of a normal force applied to the seafloor, F_N, $g(H_i)$, and $b(H_w)$, for all thicknesses where the ice draft, $D(H_i)$, is greater than the water depth, H_w:

$$\tau_{b_{max}} = \mu_s \int_0^{\infty} \int_0^{H_w = D(H_i)} F_N g(H_i) b(H_w)\ dH_i\ dH_w \tag{2-12}$$

$$F_N = \hat{g}(\rho_i H_i - \rho_w H_w) \tag{2-13}$$

This allows the basal shear stress to be computed using the relatively well constrained physical parameters of a seafloor friction coefficient, μ_s, and the densities of ice, ρ_i, and seawater, ρ_w. $\hat{g}$ is the acceleration due to gravity.

Although both the Lemieux and Dupont parameterization schemes are available in SIS2 (via the CICE IcePack), here we only use the Dupont parameterization. Note also that while MOM6 supports the tracking of icebergs, we have not yet added to this domain and so pressure ridges are the only basal shear stress mechanism accounted for in this parameterization.

2.7.4 Velocity-based definition of modeled landfast ice extent

Landfast ice extent is derived from the PAMS model output by applying a simple threshold to the daily mean sea ice velocity field followed by a 20-day running minimum to find grid cells with a velocity below the threshold for at least 20 days. To test sensitivity of this threshold, we applied three different thresholds (Table 2-6) to each of the two model runs to create 6 separate modelled datasets of landfast sea ice extent. Sea ice velocity is computed by the model as a daily mean value in units of cm s^{-1} and we selected thresholds based on the cumulative amount of motion over the 20-day period that underlies our definition of landfast ice (Section 2.1.2). The middle threshold corresponds to a total 20-day motion of around 86 m, which approximately corresponds to the spatial resolution of the SAR images used in the M2014 dataset (Mahoney et al., 2014; Mahoney et al., 2007). Thresholds 1 and 3 correspond to twice and half this amount of motion, respectively.

Table 2-6: Mean daily Ice velocity thresholds used to determine landfast sea ice extent in PAMS model output

Threshold	cm / s	m / 20-days
1	0.010	173
2	0.005	86
3	0.001	17

2.7.5 Selection of model runs

As of July 2024, the 80th model run on the 12-km grid described above is now executing. These were preceded by 20 experiments on an 18-km grid and prior to that, a few runs were performed on a 6-km grid in which we had an error in the velocity boundary conditions. All of the early simulations were performed on the University of Alaska Fairbanks' high-performance computing system known as "chinook". In 2021, co-Investigator Hedstrom obtained access to a computer in Oak Ridge known as "gaea". All of the simulations are now being done there using the Flexible Runtime Environment software which manages the compilation, resubmission, and file transfers to Princeton.

Not all of these simulations ran to completion. There have been instabilities within the ice, others within the ocean. We have learned much from the Regional MOM6 group meetings, for instance, the North Atlantic simulations show that the Gulf Stream path is extremely sensitive to the choice of Coriolis option. They have also gotten some odd Gulf Stream paths when trying a hybrid vertical coordinate instead of the z-star, even after some open boundary bugs were fixed. The Northeast Pacific group has been active in comparing their results to mooring data from the Bering Sea shelf, leading to all of us turning off the bottom boundary layer mixing and to reduce the shear mixing as the defaults currently in the model are too vigorous.

Not all model runs were focused on improvement of Arctic processes, but among those that did, there was an attempt to include a brine plume parameterization from Nguyen et al., (2009). We also changed the restratification parameterization scheme in an effort to better resolve sub-grid processes that oppose vertical mixing. We began by using the Fox-Kemper scheme (Fox-Kemper et al., 2011; Fox-Kemper et al., 2008), which uses constant lengthscale of 500 m for restratification processes. However, we later switched to using the Bodner scheme (Bodner et al., 2023), which has a variable lengthscale that depends upon latitude and other modeled ocean properties.

We also experimented with the coupler used to represent ice-ocean processes in an effort to reduce instabilities. To handle communication between all components of the model, we used the Flexible Modeling System (FMS) coupler (http://noaa-gfdl.github.io/FMS). The timestep on which the FMS coupler operates is set to half an hour (1,800 s). Accordingly, the atmospheric fields are interpolated every half hour, then the ice is advanced for the same interval, taking two steps of 900 s each. Finally, the ocean takes three (baroclinic) steps of 600 s each as well as one thermodynamic step of 1,800 s. However, ice-ocean instabilities occur at much shorter timesteps, and so we implemented a new coupled ice-ocean driver (CIOD), which couples just the ice-ocean processes at the fast ice timesteps (see Table 2-5). It is known that there is an instability in the traditional ice-ocean coupler that can show up in the marginal ice zone and lead to excessive near-surface mixing. The CIOD is being developed at the Geophysical Fluid Dynamics Laboratory, with the goal to more tightly couple the ice and ocean time-stepping in such a way as to shut down the instability. Recent experiments in the global model show that the amount of ice in the model is sensitive to the time-stepping, even with the traditional coupler. The combined modeling system has many timesteps, including the fast and slow ice timesteps (see Section 2.7.1), as well as the coupling timestep and the frequency of updating the atmospheric wind fields. The ice can become up to a meter thicker in the central Arctic with differing choices in these multi-year runs. The CIOD runs also tend to have thicker ice than those without it by roughly half a meter.

To make a quantitative comparison between the landfast ice extent simulated by the PAMS model and observations from the EM2024 dataset, we scaled and reprojected the model's 12-km gridded output to the 100-m grid used in the EM2024. This allowed us to the SLIEalyzer toolbox to make a direct comparison of the metrics described in Section 2.2. However, this was a time consuming task, requiring approximately 72 hours of processing time and the creation of approximately 1 TB of data files to complete the process for data from a single velocity threshold (Section 2.7.4) for a one model run. As a result, a detailed analysis of the landfast ice simulated by the PAMS model lagged behind the model development and we had to use model runs that had completed before April 2024 for the analysis to be included in this report.

In the following sections of this report, we present results from mode runs 51, 56, and 73, the differences between which are summarized in Table 2-7. Model run 73 was not completed in time for a thorough analysis of its simulated landfast ice extent, but is included here as an example of a later iteration of the PAMS model that allowed for hourly output, and we evaluate its ocean and non-landfast ice performance in comparison with model runs 51 and 56.

Table 2-7: Summary of differences between PAMS model runs selected for presentation in this report

Model run	Coupling system	Restratification parameterization	EM2024 comparison
51	FMS	Fox-Kemper	Yes
56	FMS + CIOD	Bodner	Yes
73	FMS	Bodner	No

3 Results

3.1 1996–2023 landfast ice climatology

3.1.1 Assessment of differences and bias between landfast ice data source

During the assimilation of the EM2024 dataset, the 2007–2008 season was the only season which contained data for all datasets. Each SLIE images' landfast ice width was measured using the SLIEalyzer toolbox (Section 2.2.1) and the coast vectors described in Section 2.2.3 in both the Beaufort and Chukchi regions. To have a direct comparison between the datasets the landfast ice width measurements were interpolated to daily resolution for the M2014, NIC, and ASIP datasets during the 2007–2008 season using a nearest neighbor interpolation. Each season in all datasets contains 304 days of landfast ice width measurements. These 304 width measurements represent SLIE locations at each coast vector each day from October 1st to July 31st of the following year. Since the M2014 data predates the ice chart datasets we treat landfast ice width measurements from the M2014 as the most accurate. After each dataset was interpolated to daily resolution an additional precaution was taken for the ASIP and NIC datasets. In addition to the daily interpolation of weekly, ASIP, and bi-weekly, NIC, ice charts we applied a 20-day running minimum to these datasets to match the methodology used during the creation of the M2014 dataset. The datasets used for comparison were all daily resolution with a 20-day running minimum applied to the width measurements at each coast vector. The daily regional mean landfast ice width in the Chukchi and Beaufort regions during the 2007–2008 season are shown in Figure 3-1 and regional mean values for maximum width and the dates of first ice and ice free events are listed in Table 3-1.

Table 3-1: Comparison of average metrics for the 2007–08 landfast sea ice season between the M2014, ASIP, and NIC datasets for the Chukchi and Beaufort regions. Note that the uncertainty ranges indicate the spatial variability within each region.

Metric	Chukchi			Beaufort		
	M2014	ASIP	NIC	M2014	ASIP	NIC
Average Maximum Width (km)	17.2 ± 21.1	18.4 ± 14.6	11.0 ± 17.65	26.3 ± 22.1	35.4 ± 30.7	29.3 ± 27.5
Average Date of First Ice	Dec 28 ±38 days	Jan 7 ± 35 days	Jan 11 ± 69 days	Dec 4 ± 60 days	Dec 8 ± 38 days	Nov 24 ± 36 days
Average Date of Ice-Free	May 31 ± 21 days	May 22 ± 23 days	May 14 ± 22 days	Jun 9 ± 19 days	Jun 11 ± 5 days	May 31 ± 21 days

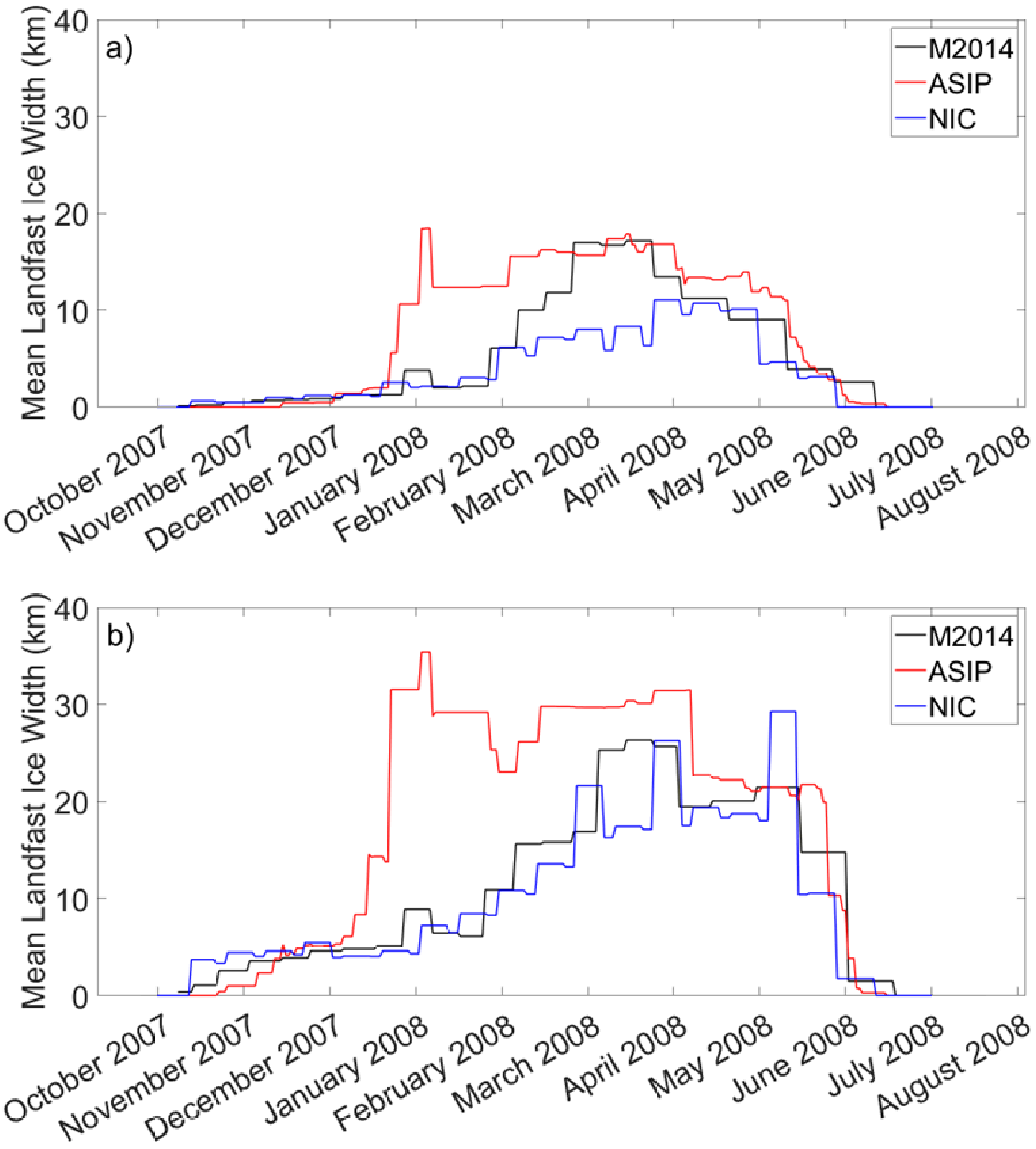

Figure 3-1: Landfast ice width for the a) Chukchi and b) Beaufort regions for all three datasets available for the 2007–2008 season.

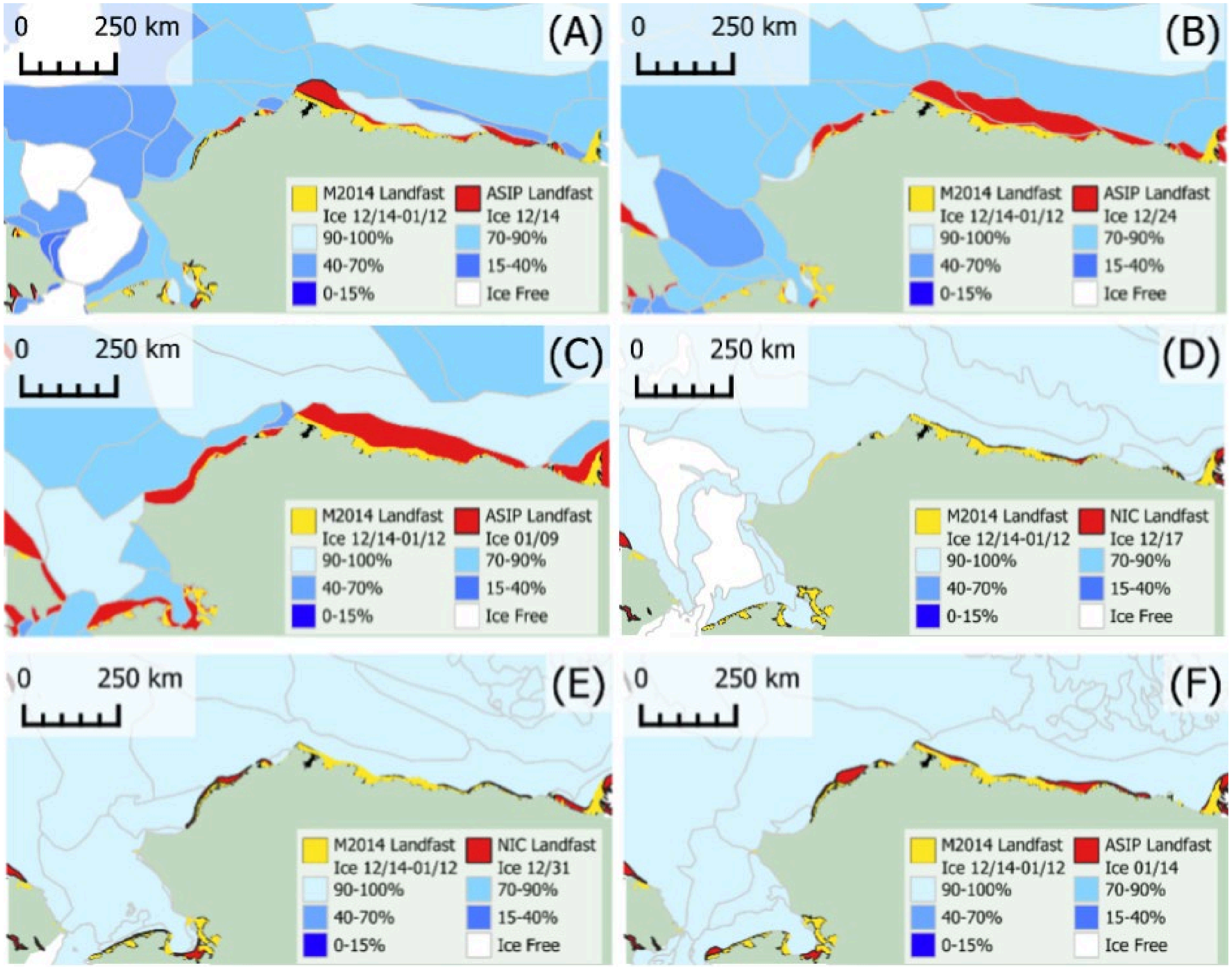

Figure 3-2: ASIP (A, B, C) and NIC (D, E, F) ice charts from December 2007 and January 2008 with the M2014 SLIE image (yellow) measurement of landfast ice during the similar period. ASIP ice charts depicted are (A) 12/14/2007, (B) 12/24/2007, and (C) 1/9/2008. NIC ice charts depicted are (D) 12/17/2007, (E) 12/31/2007, and (F) 01/14/2008. Red areas indicate areas in each ice chart identified as landfast ice by ASIP and NIC. Shades of blue indicate various concentrations of sea ice.

Small deviations in the landfast ice width measured by each dataset were expected as the methodology and frequency which was used to identify areas of landfast ice differed amongst datasets. Both the ASIP and NIC datasets fall within 1 standard deviation of the M2014 dataset for maximum regional mean landfast ice with, mean first ice date, and mean last ice date. One exception to this is a stable extension of landfast ice reported in the ASIP dataset during the early 2007–2008 season deviated from the other two datasets (Figure 3-1). During January and February, an extension of landfast ice was observed in the ASIP dataset which was not observed in either the M2014 or NIC datasets (Figure 3-1). The difference in landfast ice width observed by the ASIP ice charts can be attributed to specific ice charts (Figure 3-2). Along the Beaufort region, mobile pack ice with 90–100% concentration occupied the existing SLIE between December 12th, 2007, and December 14th, 2007. These vector features in the ASIP ice charts were reclassified as landfast ice as there was no identifiable motion between ice charts. The lack of motion and continuity to the previously charted landfast ice likely lead the analyst at ASIP to classify these areas as landfast. Later, 1–2 months, in the season similar extents were identified as landfast by the M2014 dataset and NIC dataset. This deviation from the other datasets was not a consistent trend found in the ASIP ice charts and was treated as an anomaly within the dataset.

Landfast ice width measured for all seasons in which any dataset had valid data for the whole season, described in Table 2-1, are shown in Figure 3-3. As described in Section 2.2.3, we calculated the landfast ice width along 8,892 locations across our study region, 6,956 in the Chukchi region and 1,936 in the Beaufort. Averaging the daily SLIE measurements across each region highlights interannual variability in the landfast ice regime not revealed in the average seasonal. A total of 27 annual cycles covering the years 1996–2023, with 12 measured by M2014, 16 by ASIP, and 15 by NIC (Figure 3-3). Each season follows a similar pattern with a gradual advance and rapid retreat in both regions. In the Chukchi region, the regional mean landfast ice extent typically achieved an annual maximum between 10–25 km for all datasets (Figure 3-3a). The 2017–2018 and 2018–2019 seasons were anonymously low landfast ice widths (<5 km), and only ASIP data were available. In the Beaufort region, the landfast ice typically achieves an annual maximum mean width between 20–30 km for all datasets (Figure 3-3b). Overall, the ASIP and NIC datasets agreed well with regards to regional mean landfast ice width. When deviations were observed between datasets, the deviations were not consistent in the sense that ASIP was not always measuring greater landfast ice width compared to NIC. The inconsistent differences between the NIC and ASIP datasets provided no evidence to choose a single dataset to update the M2014 dataset. As such we chose to average the ASIP and NIC datasets, described in Section 2.3 to update the M2014 landfast ice climatology.

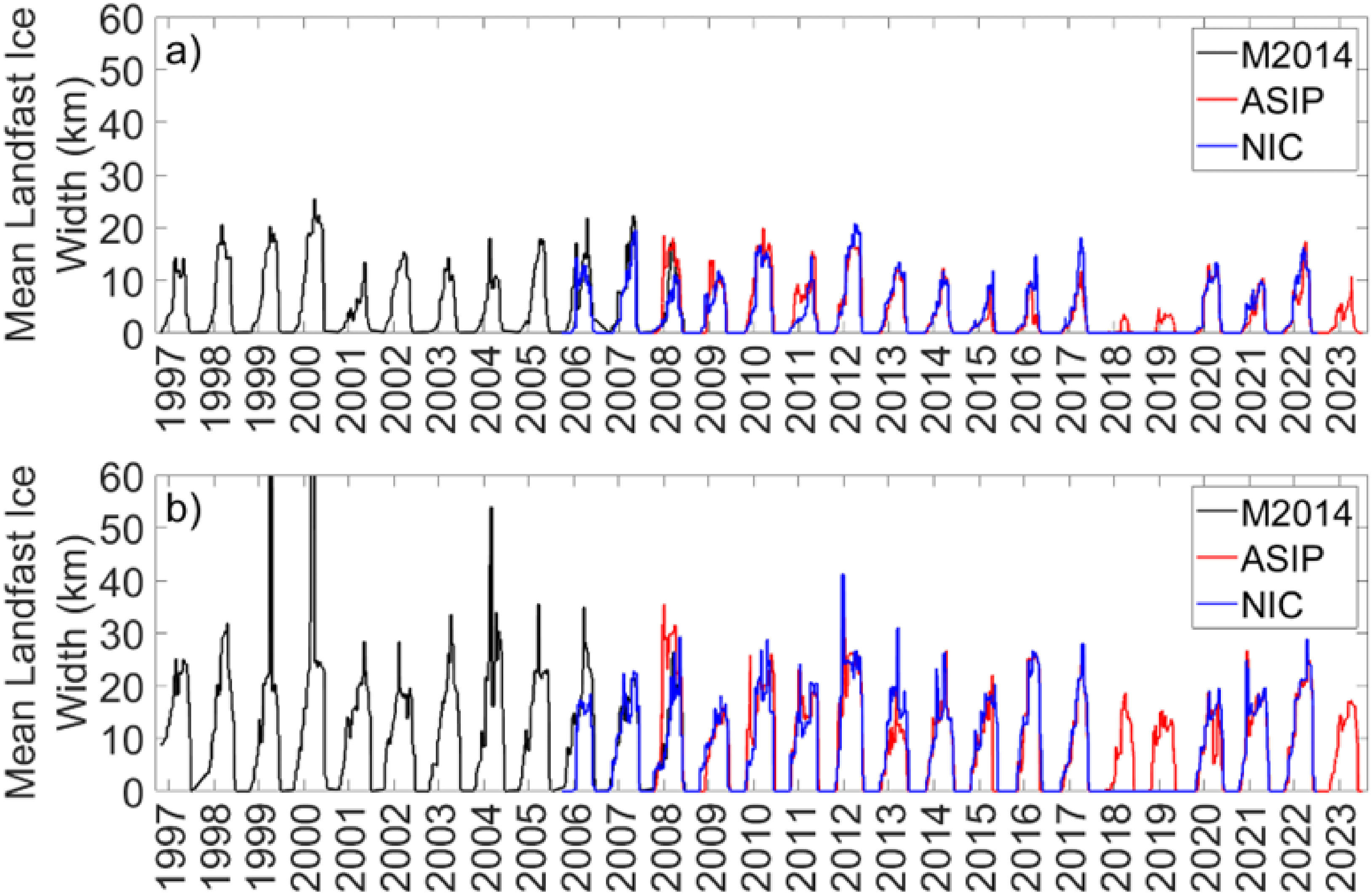

Figure 3-3: Time series of mean landfast ice width in the a) Chukchi and b) Beaufort regions for all seasons for the M2014 (black), ASIP (red), and NIC (blue) datasets. For this comparison, all datasets are interpolated to daily resolution, while the ASIP and NIC datasets also have a 20-day running minimum applied.

3.1.2 Regional landfast ice variability in the EM2024 dataset

By computing the median daily landfast ice width for the Chukchi and Beaufort regions (Figure 3-4) we can summarize and compare landfast ice extent variability over time and between the two regions. In the Chukchi Sea (Figure 3-4a) we see that typical maximum mean landfast ice width varies between 10–25 km, with anomalously low landfast ice widths during the 2017–18 and 2018–19 seasons. In the Beaufort region (Figure 3-4b), typical maximum mean landfast ice widths vary between 20 km and 30 km with multiple stable extensions in excess of 50 km in the pre-2008 (i.e., M2014) part of the record. However, in addition to variation between the region, there is considerable variability in landfast ice width within each region, which is illustrated by the shaded regions in Figure 3-4. This local-scale variability of landfast ice width along the coast appears to scale with median width such that it is typically greater in the Beaufort region than in the Chukchi region and years with a high median landfast ice width exhibit more intra-regional variability than those with a lower median width. It also notable that the differences in mean daily landfast ice width between the different data sources (Figure 3-3) are considerably smaller than the spatial variability in landfast ice width within each region, as indicated by the extent of the shaded regions in Figure 3-4.

3.1.3 Landfast ice occurrence probabilities

To visualize the spatial variability in the location of the SLIE, we rasterized and stacked all the daily SLIEs for all years on a single grid. This allows us to count the number of days that a SLIE occupied any given pixel within the grid. By "fattening" each SLIE to a width of 10 pixels (1,000 m) before doing so and then dividing by the total number of days in the record (7,668), we are able to estimate the probability that the SLIE occurred within a 500-m radius of a given point in space (Figure 3-5). The lightest shades of blue indicate areas where the SLIE rarely occurred, and these are generally found furthest offshore. The typical range of SLIE location is indicated by darker blue shades, while areas of red correspond to locations where the SLIE occurred on at least 389 different days (5% of all daily SLIE images). Individual regions of high SLIE probability separated from the coast are referred to as "nodes" (Mahoney et al., 2014; Mahoney et al., 2007) and are encircled by dashed yellow. These are interpreted to represent regions of recurring grounded ice features.

By stacking the SLIE images (i.e. including the areas shoreward of the SLIE) rather than just the SLIEs themselves, we use a similar approach to determine the probability that any given pixel was occupied by landfast ice, which can be expressed as a percentage or in days per year. To illustrate variability in landfast ice occurrence over the 27-year span of the EM2024 , we calculated landfast ice occurrence probability over three 9-year periods (Figure 3-6). Areas shoreward of nodes identified in Figure 3-5 show the highest occurrence probabilities, though there is a notable reduction in the area of high probability behind the node in Harrison Bay (which represents the node farthest from the coast) since the 1996–2005 period (Figure 3-6a). Stable extensions, as described by Mahoney et al., (2014; 2007), are represented by widespread areas of low probability indicative of their infrequent and brief occurrences. These areas are notably absent from the 2005–14 and 2014–23 periods (Figure 3-6b,c), though it is likely that any such unusually extensive areas would not be charted as landfast by NIC and ASIP analysts so their absence in data derived from ice charts may not be meaningful.

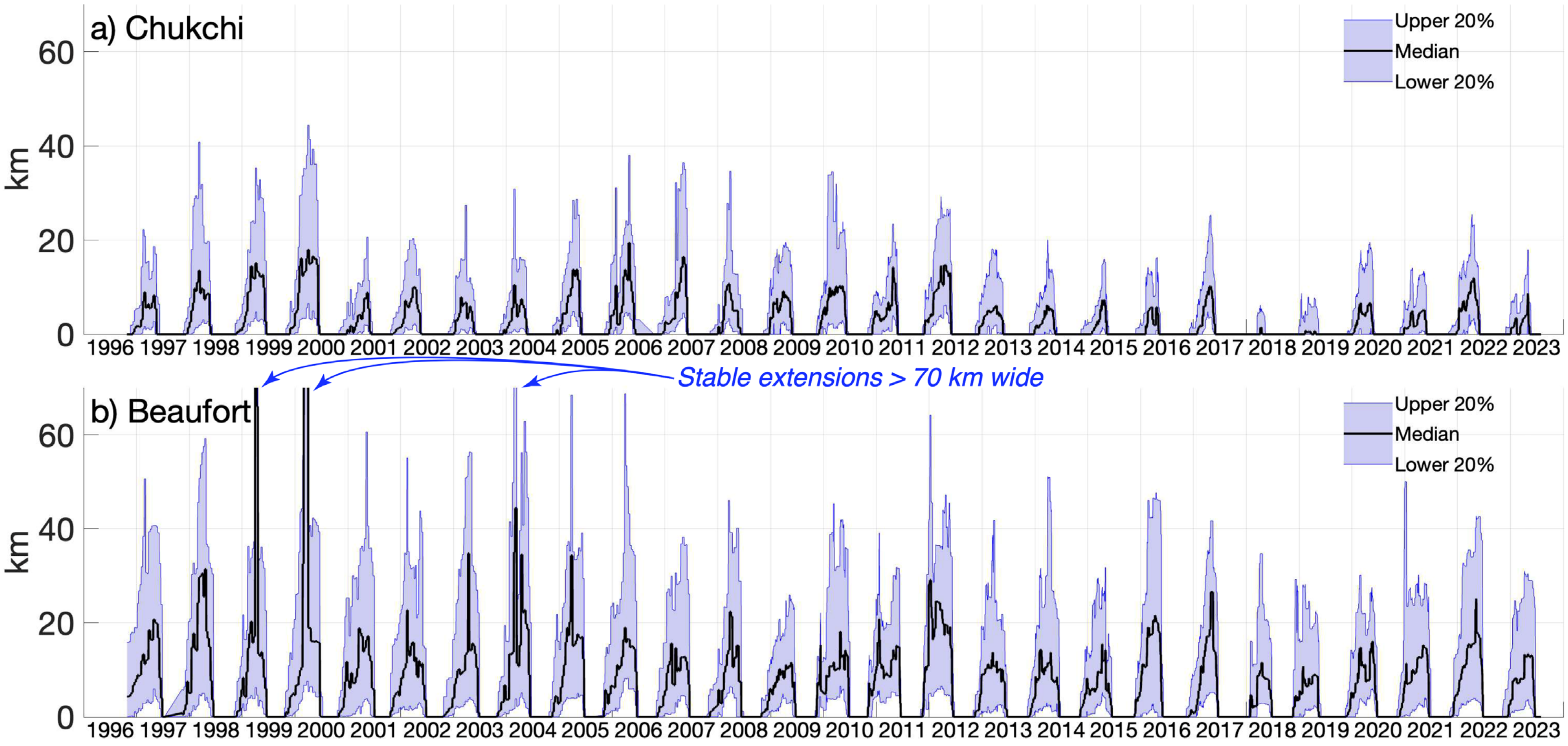

Figure 3-4: Regional median landfast ice width in the a) Chukchi and b) Beaufort regions. The shaded regions represent the spatial variability in daily landfast ice width in each region. Note full width of stable extensions that occurred in the Beaufort Sea in 1999, 2000, and 2004 extend beyond the limit of the y-axis.

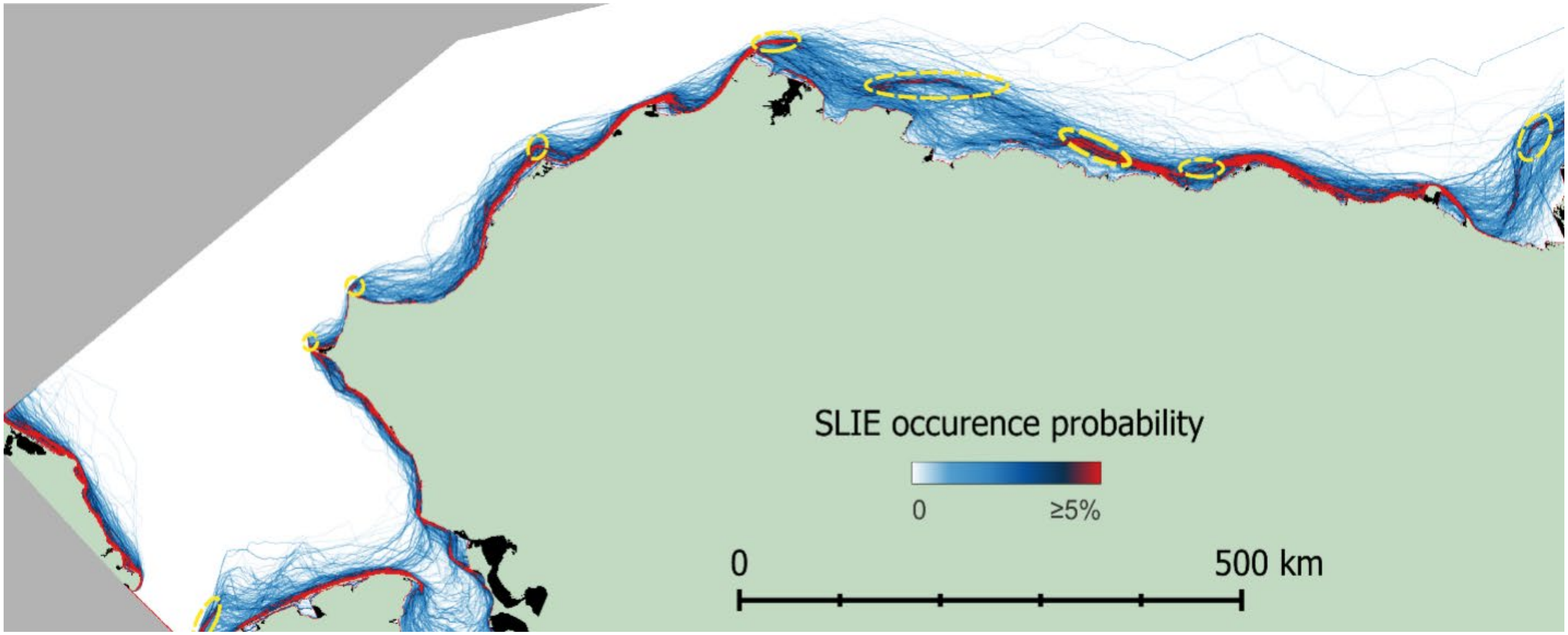

Figure 3-5: All SLIEs delineated from the period 1996–2023 stacks so the color value of a line indicated the probability of the SLIE lying within 500 m of a given point between October and July. A near continuous dark blue zone indicates where the SLIE commonly stabilizes. Dashed yellow ellipses highlight the location of nodes some distance from the coast where the SLIE occurs with greater frequency, and which indicate probable locations of recurring grounded ice features.

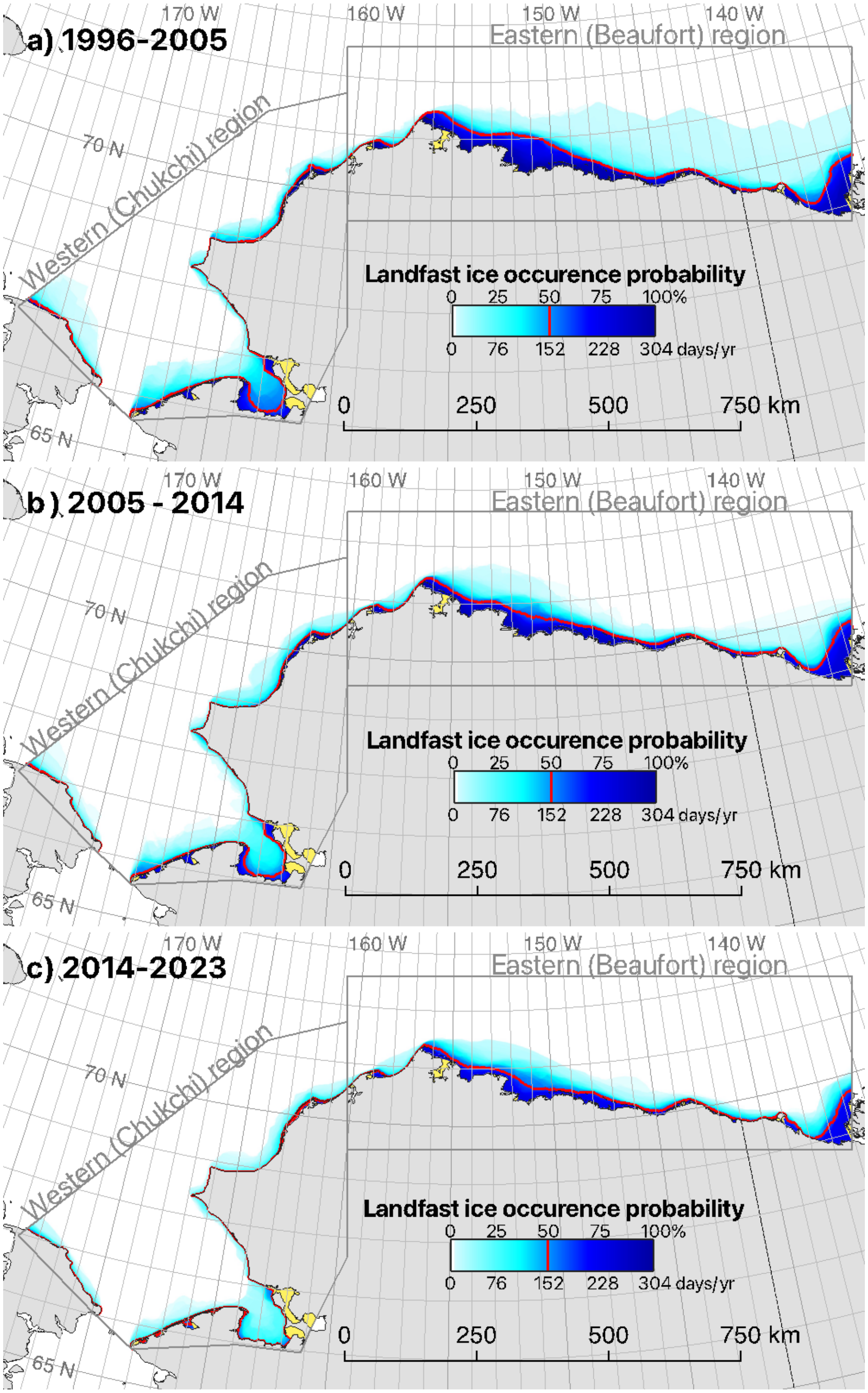

Figure 3-6: The extent of landfast ice shoreward of the SLIE stacked for each 9-year period in the EM2024 dataset (1996–2023), such that the shade of blue represents the fraction of the 304-day annual cycle (October-July) for which that area was occupied by landfast sea ice. The red line indicates the 50% probability contour. White areas indicate where landfast ice was never observed.

3.1.4 Monthly landfast ice extents

Landfast ice is a seasonal feature in the study region, typically occupying the waters adjacent to coast from October or November through June or July, as illustrated by the annual cycles in Figure 3-4. The spatial pattern of this seasonal variability is illustrated by monthly plots of the minimum, median, mean, and maximum landfast sea ice extent (Figures 3-7–3-10). Over the full duration of the EM2024 landfast ice rarely occurred in October such that the median landfast ice width for the month is zero throughout the study region, meaning that landfast ice was absent from the entire study area during October more than 50% of the time. When landfast ice was present in October, the vast majority of it was found in the Beaufort Sea, though some was present in sheltered lagoons along the Chukchi coast (as indicated by maximum extent in Figure 3-7a). November is the first month of the landfast ice season in which the median landfast ice width was non-zero (Figure 3-7b), though the median extent is still confined to sheltered regions of the coast.

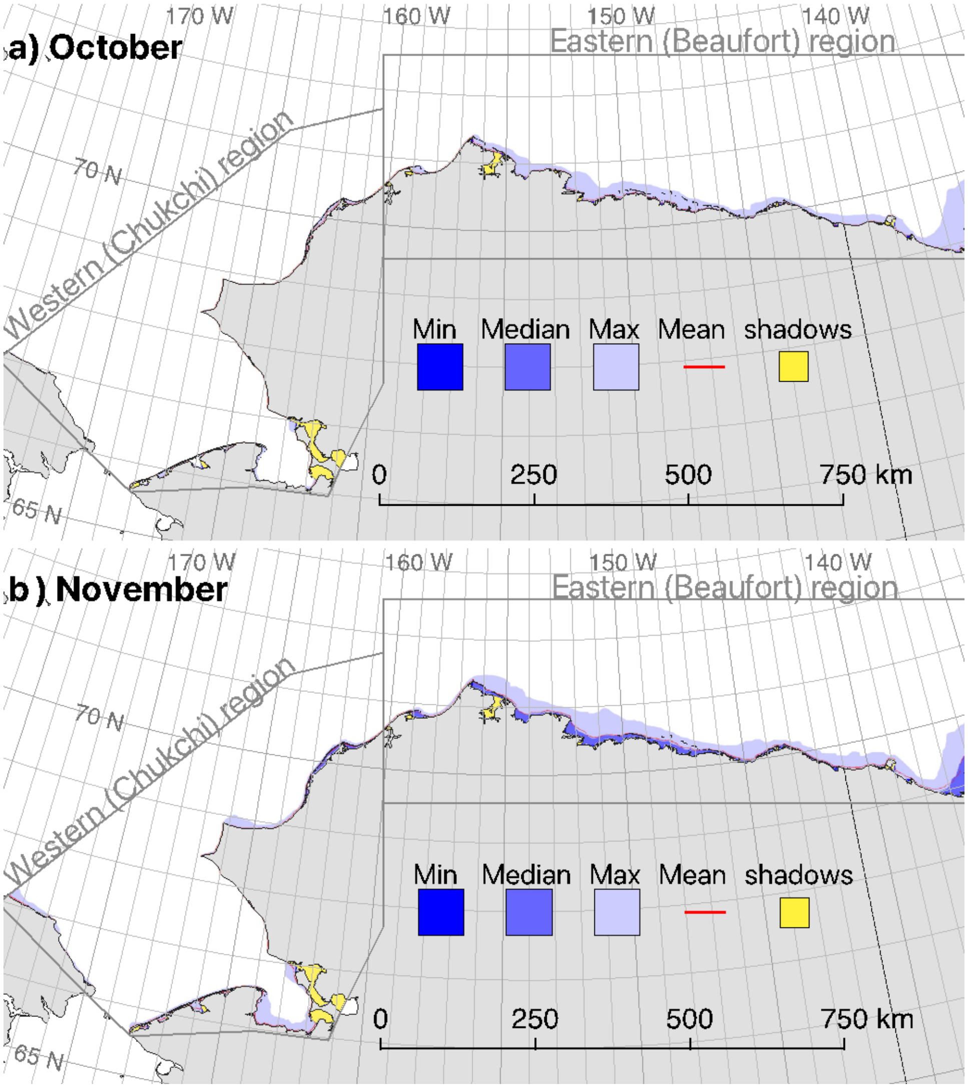

Figure 3-7: Monthly minimum, median, maximum, and mean landfast sea ice extents for the months of October and November.

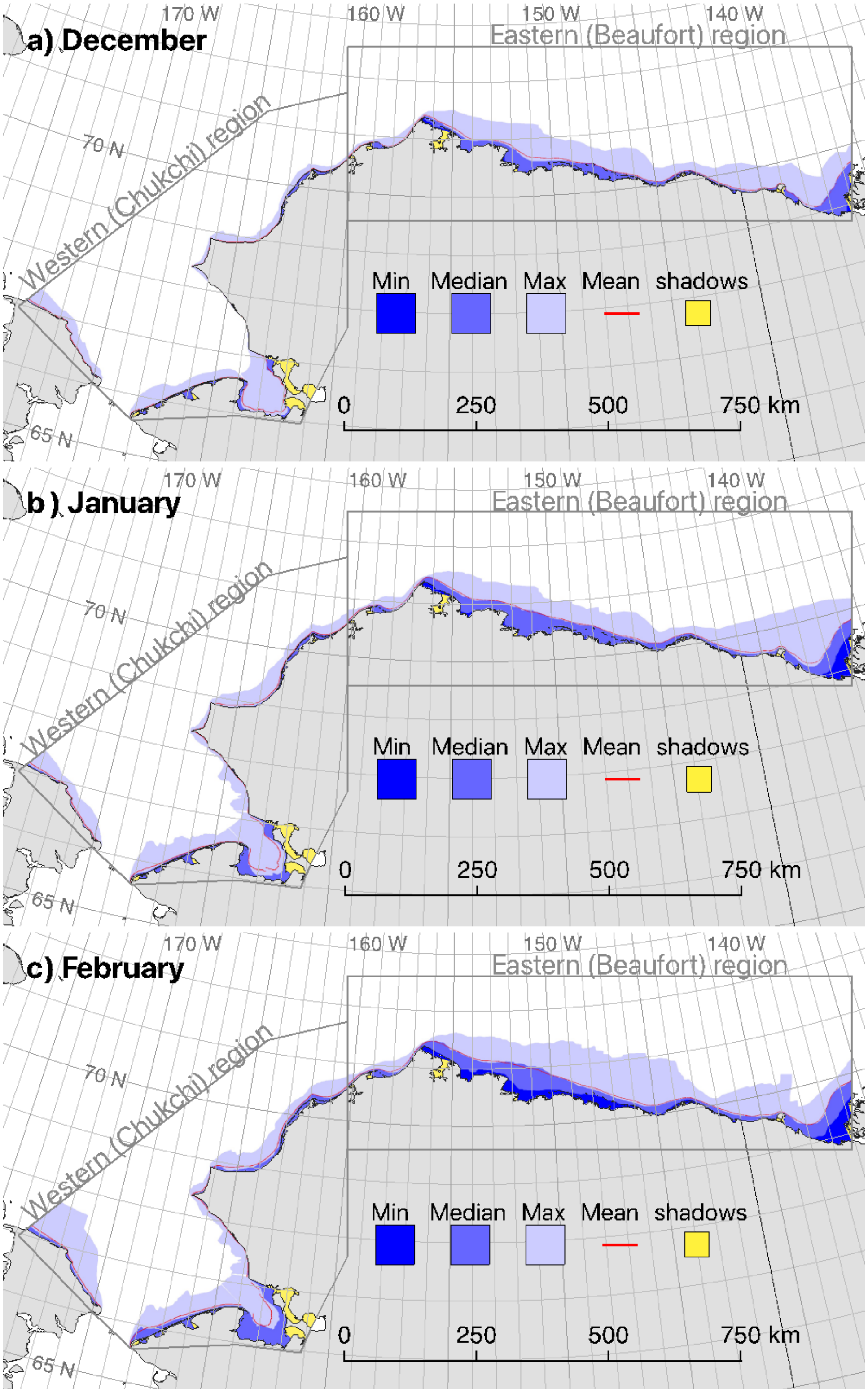

Figure 3-8: Monthly minimum, median, maximum, and mean landfast sea ice extents for the months of December, January, and February.

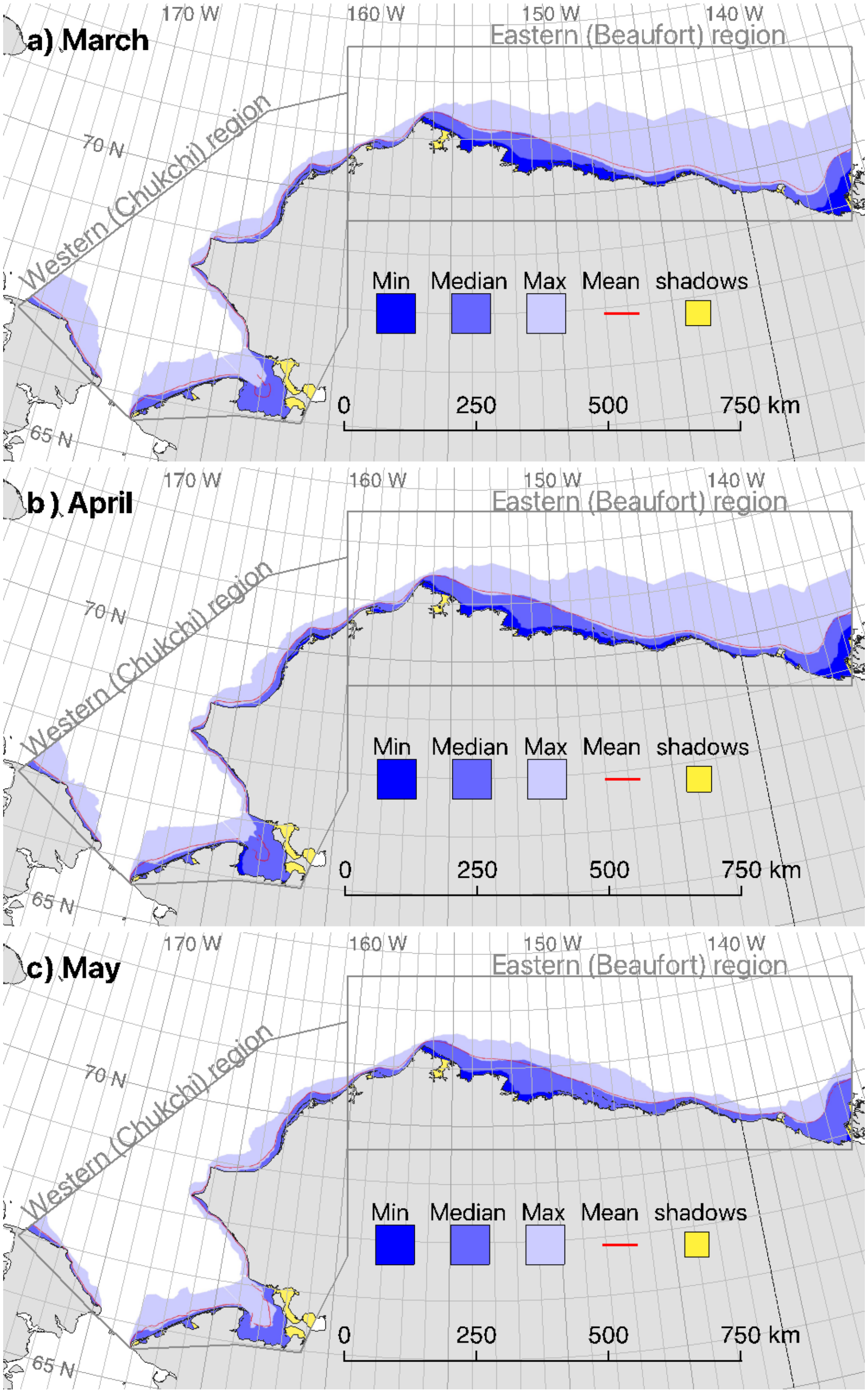

Figure 3-9: Monthly minimum, median, maximum, and mean landfast sea ice extents for the months of March, April, and May.

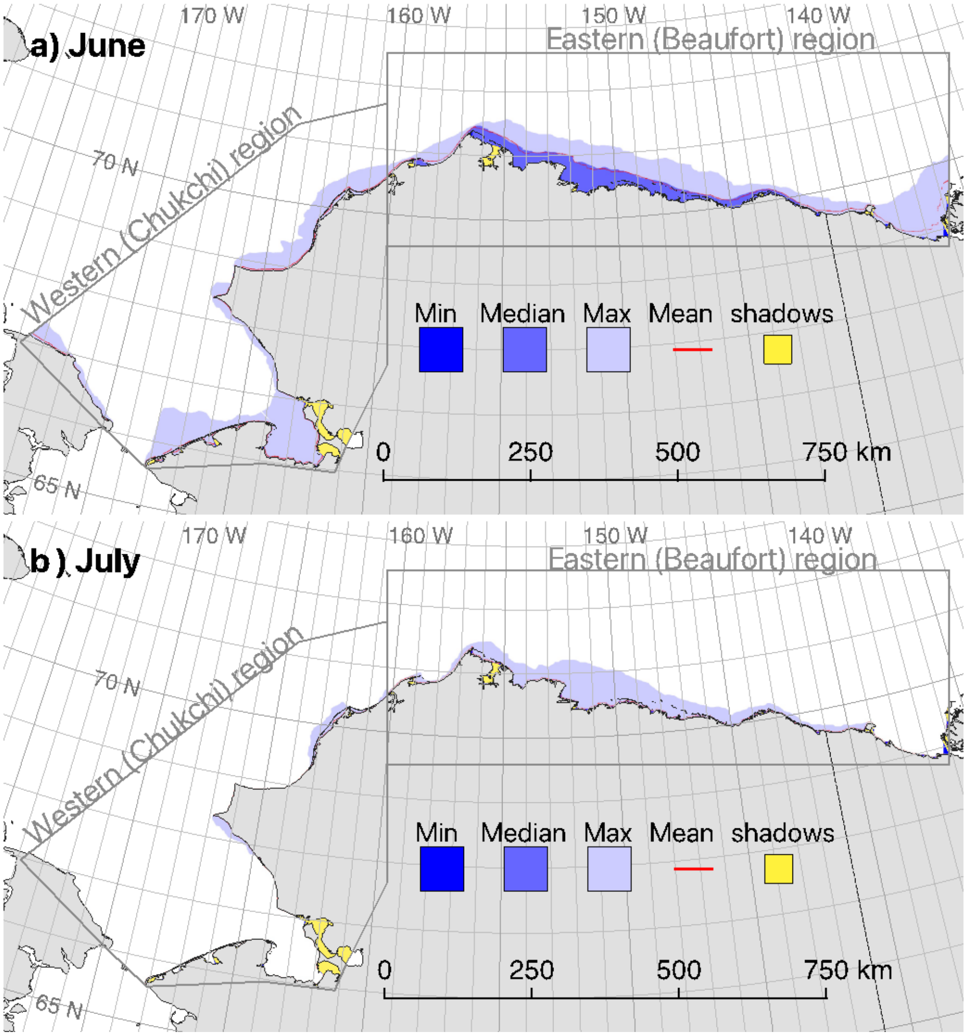

Figure 3-10: Monthly minimum, median, maximum, and mean landfast sea ice extents for the months of June and July.

By December, the median SLIE position has advance to just beyond the barrier islands in both the Chukchi and Beaufort regions and the most sheltered regions of Kotzebue Sound (Figure 3-8b). However, with the exception of a small area in Elson Lagoon near Point Barrow, the minimum monthly landfast ice width remains zero throughout both regions until January (Figure 3-8b) and it is not until February that the minimum landfast ice extent covers at least half the adjacent coastline in the Beaufort Sea (Figure 3-8c). This indicates that throughout most of the study region, there was at least one year in which landfast ice either did not form until February or experienced a breakout event that extended all the way to the coastline. In most of Chukchi Sea, the minimum landfast ice extent remains zero throughout the year.

Overall, the minimum, median, and maximum monthly landfast ice extents achieve maxima in the month of April (Figure 3-9b). In May, there was a notable reduction in the maximum extent of landfast ice in the Beaufort Sea (Figure 3-9c), but the minimum and median extents closely resemble those of April. This implies that interannual variability of landfast ice extent is comparatively low in May. As the landfast continues to retreat in June (Figure 3-10a), the minimum monthly extent becomes zero once again throughout the study region, with the median landfast ice extent also becoming zero in the Chukchi Sea. However, the maximum landfast ice extent is slower to retreat and, in June, resembles that of May. This indicates that in some years, breakup did not commence until at least June. In the Chukchi Sea, the monthly maximum extent remains remarkably consistent from April to June, which suggests there is a bathymetric limit on the maximum extent in this region. In July, the minimum and median extents are effectively zero throughout both study regions but the maximum extent demonstrates that extensive regions of landfast remained until July in the Beaufort Sea and northern Chukchi Sea in at least one year (Figure 3-10b).

3.1.5 Timing of annual landfast ice events

Following the methods described in Section 2.2.5, we derived the annual occurrence dates of 3 key events based on the timeseries of landfast ice measured width at each coast vector (Figure 3-11). The median date on which each event occurred throughout the study region is shown by a solid colored line. The shaded region around each line extends between the lower and upper 20th percentiles and illustrates the range of interannual variability. The median dates of freezing and thawing onset are shown by dashed lines, inside of their respective lower and upper 20th percentiles. These were calculated following the method of Mahoney et al., (2014; 2007) from NCEP reanalysis data interpolated to the origin point of each coast vector.

Overall, landfast ice forms earliest in regions where freezing temperatures occur earliest, but there is no consistent relationship between the dates of first ice and those of freeze onset. Abrupt changes in the date formation along the coast correspond to pronounced features in the coastline, such as Point Lay and Icy Cape. The landfast ice between these points is among the earliest to form in the study region, along with the ice along the Beaufort Sea coast between Point Barrow and Kaktovik, where there are many coastal lagoons and barrier islands. The latest place in our study region where landfast ice occurs is between Kivalina and Cape Lisburne, which is the only section of coast with a southerly aspect.

The occurrence of breakup is closely followed by ice free conditions and those locations where breakup occurs earliest are also the locations that become ice free earliest. In general, there is less variability in the timing of these season-ending events than in the date of formation at the beginning of the season. However, there are some short sections of the coastline where breakup and ice free conditions occur substantially earlier than on the coast to either side. For example, the landfast ice to the east of the headland near Enurmino on the northern Chukotka Peninsula typically breaks up in mid-April, while the landfast ice on either side remains in place until mid-May or June. Similarly early breakup occurs on the east-facing coast immediately west of Bering Strait, the west facing coast immediately south of Cape Lisburne, and in the vicinity of Herschel Island. Landfast ice is also later to form in these locations, such that the upper bound of first dates ice comes close or even overlaps with the lower bound of breakup dates in some cases. One thing these locations all have in common is a relatively narrow landfast ice cover, as indicated by the proximity of the SLIE to the coastline in these locations (Figure 3-5). The time period between the onset of thawing temperatures and the end of the landfast ice season is much shorter than that between the onset of freezing temperatures and the beginning of the landfast ice season. With the exception of the aforementioned locations where breakup occurs particularly early, the median date of breakup in the Chukchi Sea is almost coincident with the median date of thaw onset. By comparison, the median breakup date is 2–3 weeks later than the median thaw onset throughout most of the Beaufort Sea. This suggests that surface heating has a less direct relationship with breakup in this section of coastline.

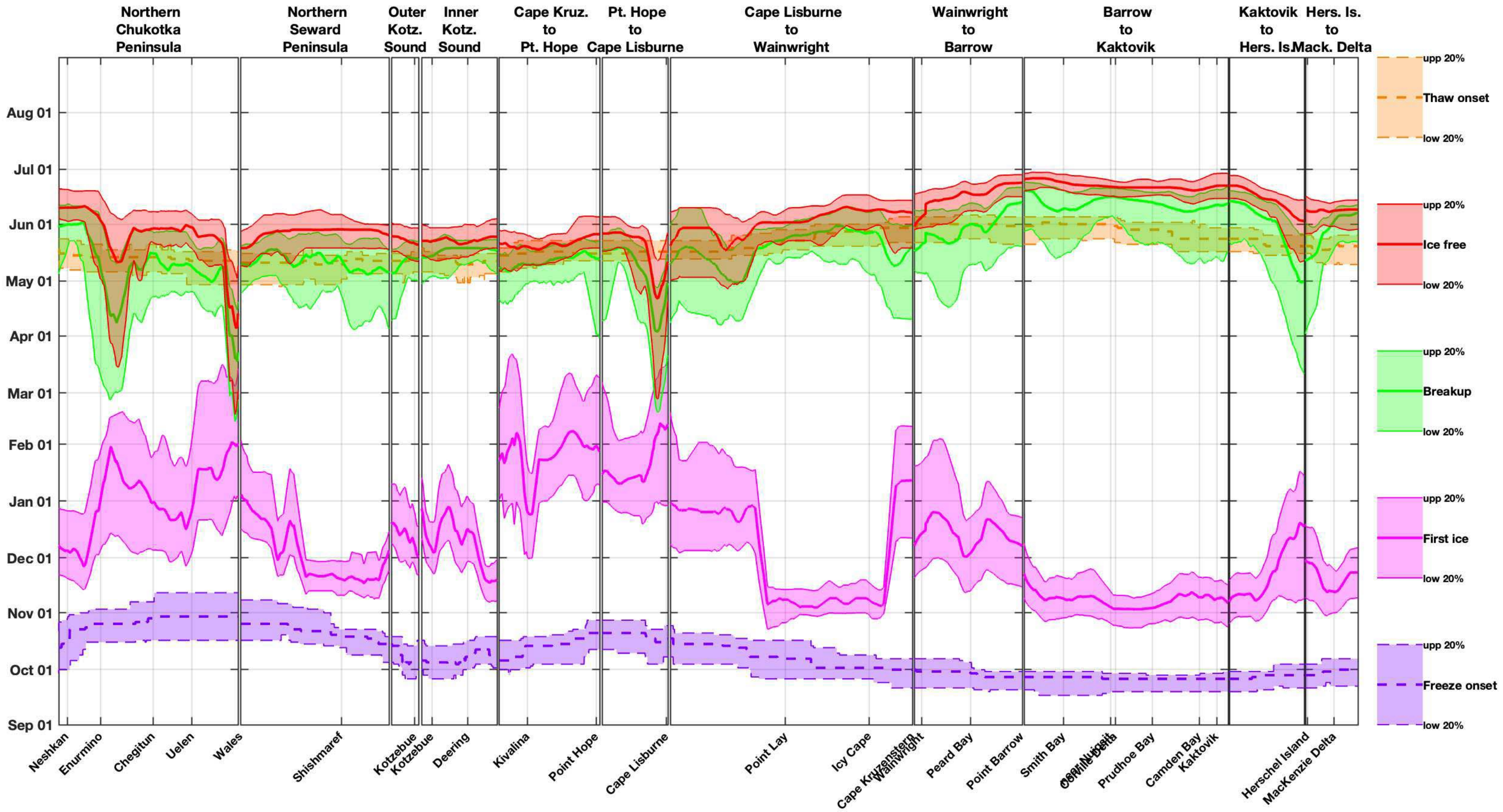

Figure 3-11: Spatial variability in the median dates of occurrence of 3 key events in the annual cycle (First Ice, Breakup, and Ice-Free) over the duration of the EM2024 dataset. Also shown are median dates of the onset of freezing and thawing derived from NCEP reanalysis data.

3.1.6 Landfast ice breakout events

Applying the criteria described in Section 2.2.7 to the EM2024 dataset, we identified a total of 202 individual breakouts in the Beaufort study region and 161 in the Chukchi region (Appendix A). On average, there are 7.5 breakout per year in Beaufort region, compared with 6.0 per year in the Chukchi region. However, there is considerable interannual variability and there were 9 seasons when there were as many or more breakouts in the Chukchi region than the Beaufort (Figure 3-12). There is also some evidence of synchronous peaks and lulls in breakout activity in both regions every 7–10 years. The underlying cause for the absence of breakouts in some years (2003–04 and 2021–22 in the Chukchi region and 2011–12 in both regions) is unclear. If we relax our breakout criteria, we detect some events in these years, but the overall 7–10 year pattern of peaks and lulls remains. The difference in annual average breakout counts between the Chukchi and Beaufort regions can be primarily ascribed to breakouts in January, when on average the Beaufort region experiences twice as many breakouts as the Chukchi (Figure 3-13a). In February, March, and April, breakout events seem equally frequent in both regions. Breakouts are of similar area in both regions and the size distribution appears to follow a power law such that larger breakouts have a lower likelihood of occurring (Figure 3-13b).

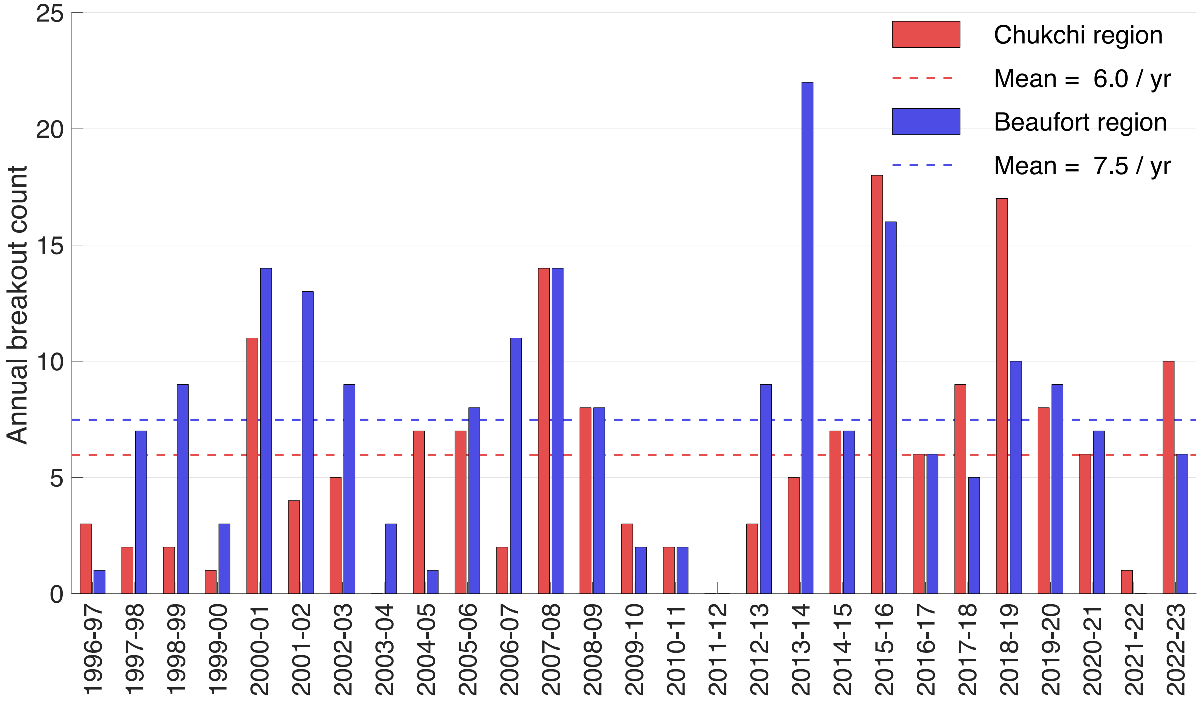

Figure 3-12: Annual counts of breakout events in the Chukchi and Beaufort study regions.

We computed a map of breakout probabilities by accumulating, or stacking, the areas of ice involved in each breakout in the catalog (Figure 3-14). By dividing the breakout count, N_b, by the number of years, $N_{yr} = 27$, we derive the average number of breakouts per year, $\overline{N}_b$, on a pixel-by-pixel basis (Equation 3-1). This shows that some areas are more prone to breakout than others (Figure 3-14a). In particular, the region eastward of Point Barrow shows breakout counts of over 0.3/yr, indicating that extensive breakouts can occur approximately every three years. Other breakout "hotspots" are found in the southernmost Chukchi coastline either side of Bering Strait, the area between Kotzebue and Cape Kruzenstern, and the section coast between Kaktovik and Herschel Island.

$$\overline{N}_b = N_b/N_{yr} \tag{3-1}$$

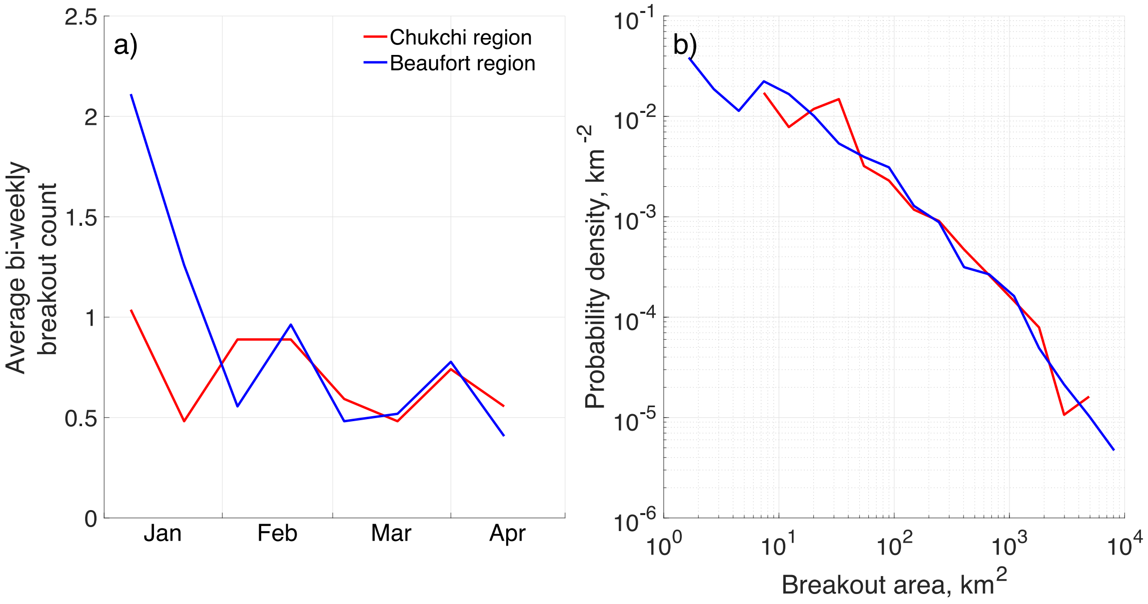

Figure 3-13: a) Average bi-weekly breakout counts and b) probability density distribution of breakout size for the Chukchi and Beaufort study regions.

By dividing $\overline{N}_b$, by the annual likelihood that landfast ice occupied each pixel, $P(landfast)$, we can also obtain a measure of the breakout probability, $P(b)$ (Figure 3-14b):

$$P(b) = \overline{N}_b / P(landfast) \qquad (3\text{-}2)$$

P(b) provides the probability of a breakout occurring if the ice becomes landfast ice in a given region. A probability of 1 indicates that every time landfast ice occupied that pixel it underwent a breakout. Comparison between Figures 3-14a and 3-14b shows that regions with a breakout probability near 1 correspond to regions with low overall breakout counts, meaning that landfast ice is rarely found at these locations.

We also computed the conditional breakout probability, $P^*(b)$, which represents a measure of the likelihood that any given pixel will become landfast between January and April and then subsequently breakout (Equation 3-3).

$$P^*(b) = \overline{N}_b \cdot P(landfast) \qquad (3\text{-}3)$$

This emphasizes the areas of potential breakout risk that overlap with areas where landfast is likely to occur (Figure 3-14c), which is primarily in the regions closest to the shore.

3.1.7 Access and availability of climatology dataset

A copy of the EM2024 dataset of landfast ice extent in the Arctic OCS was provided to BOEM with this report. We are continuing to explore longer term open online access to the data for public dissemination after completion of the project and anticipate that results will be available as a “data story” through the Scenarios Network for Alaska and Arctic Planning (SNAP) at https://uaf-snap.org.

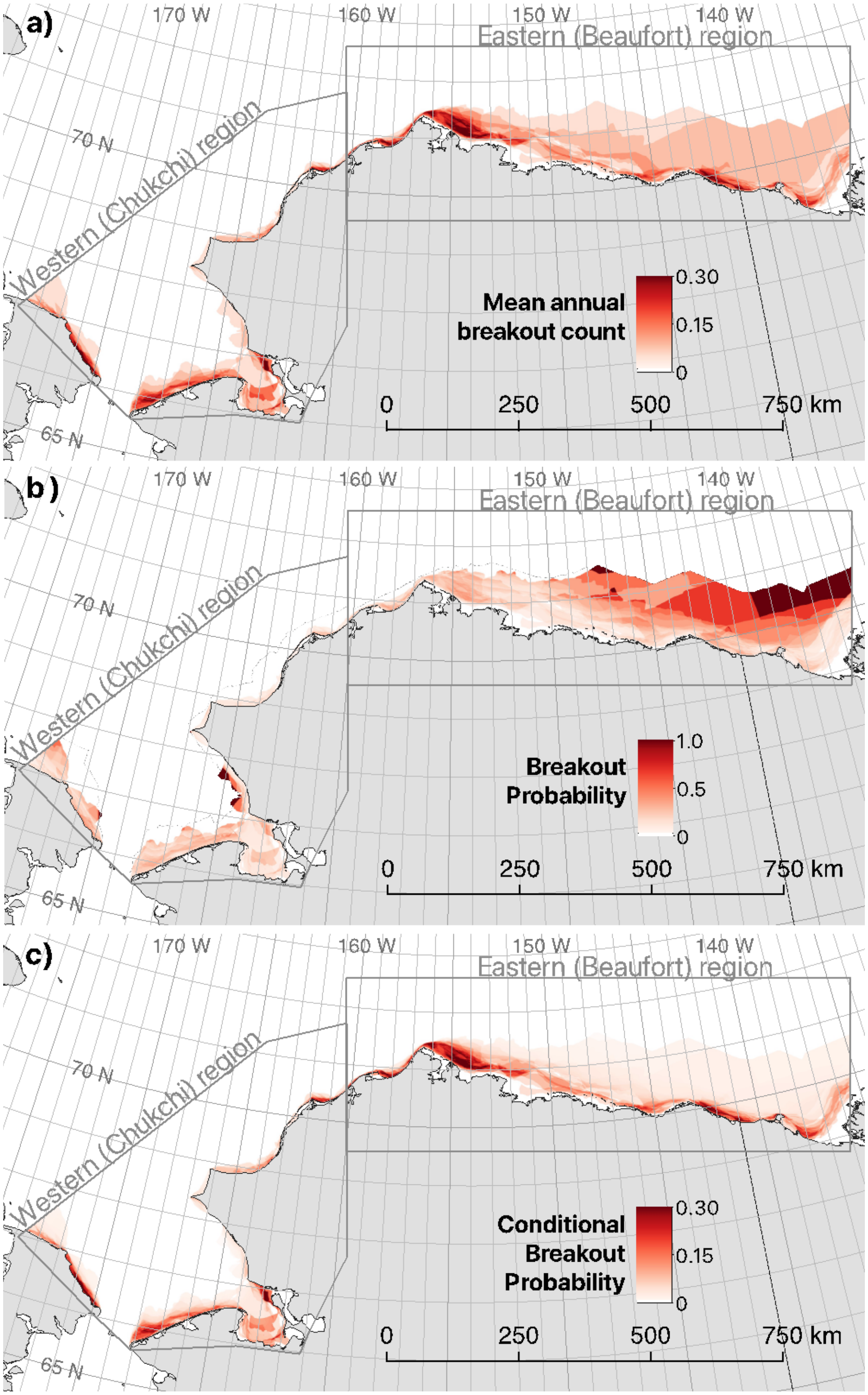

Figure 3-14: Spatial distribution of breakouts across the combined study region shown as a) mean annual breakout, b) breakout probability, and c) conditional breakout probability. See text for details of how these values were calculated.

3.2 InSAR-derived landfast ice extent and stability

3.2.1 Landfast ice extent from coherence masks

The automated methodology for delineating areas of landfast ice from mobile pack ice using interferometric coherence derived from Sentinel-1 interferograms, described in Section 2.4.2, was applied to 2,084 SAR image pairs from 2017–2021 along the study region coastline. In total, 14 interferometric wide reference scenes were identified which covered the study region. During a typical month, 2 Sentenel-1 SAR pairs satisfied our temporal and perpendicular baseline requirements for each reference scene. Certain areas within the study region such as Kotzebue Sound, Colville Delta, and Mackenzie Delta, had fewer acquisitions resulting in months with 1 or no acquisitions which satisfied our baseline requirements. The thresholded coherence images (Section 2.4.2) were sorted and mosaiced by month and year to represent monthly images of InSAR-derived landfast ice extent. This resulted in produced 24 monthly coherence mosaics representing each month between December and May during the 4 landfast ice seasons between 2017 and 2021, which could be used as inputs to the SLIEalyzer toolbox. For example, Figure 3-15 compares the InSAR-derived mean landfast ice extent during April (cyan) line with that derived from the EM2024 dataset (blue) for the period 2017–2021. This shows generally good agreement, with no consistent bias across the study region for this month.

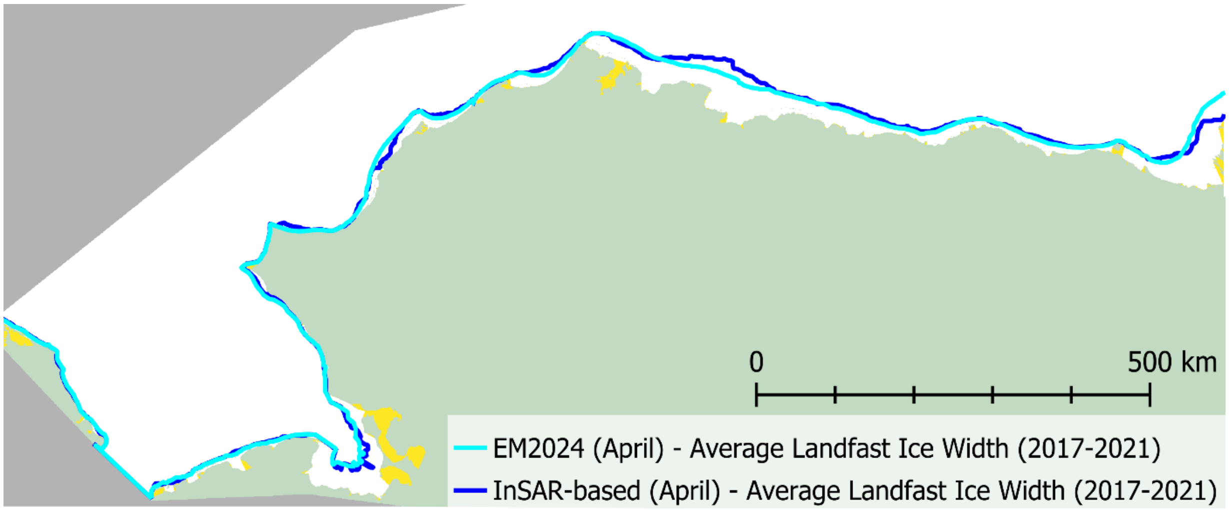

Figure 3-15: Mean SLIE position for the month of April by the EM2024 dataset (cyan) and InSAR-based method (blue) from 2017 –2021. Yellow regions indicate "shadow" zones outside the domain of the coast vectors (see Figure 2-1).

To compare the InSAR-derived landfast ice extent against the EM2024 dataset for all months from December to May, we calculated the difference in landfast ice width for each coast vector (Figure 3-16). Here, the difference (blue line) is calculated by subtracting the InSAR-derived width from the EM2024 values. The normalized difference (gray line) is derived by dividing the difference by the EM2024 width. During December, mean landfast ice width was zero throughout much of the study region and both datasets generally agree where landfast ice had not yet formed, but small differences in width result in large normalized differences. However, where landfast was present (primarily in the Beaufort region), the InSAR-derived results tend to underestimate the width. This is illustrated by the tendency of the blue line to lie below the x-axis in Figure 3-16a.

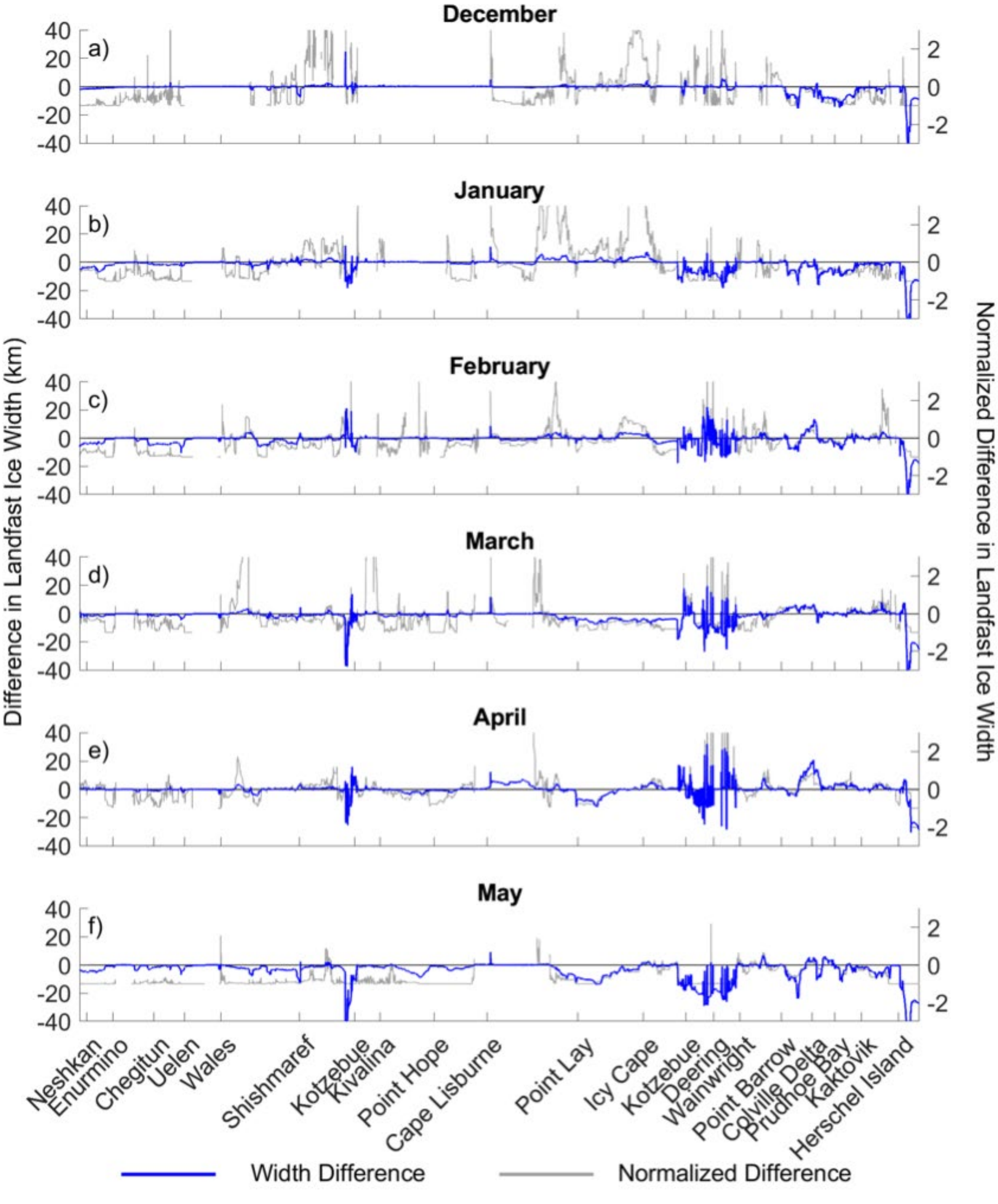

Figure 3-16: Difference in landfast ice width at each coast vector from 2017–2021 between the InSAR-derived results and the EM2024 dataset. Positive values indicate that the InSAR method overestimate landfast ice extent relative the EM2024 dataset.

There is a similar pattern for the month of January (Figure 3-16b), with the InSAR approach still tending to underestimate the width of landfast ice as it expands throughout both study regions. However as the season progresses through February, March, and April, the relationship becomes more variable along the coast, with the InSAR-based approach indicating over 10 km more landfast ice on average than the EM2024 dataset (Figure 3-16b-e). Also, there is notable spatial variability in Kotzebue Sound during these months, with the difference in landfast ice width changing from <−10 km to >10 km and back again over the span of just a few coast vectors. The cause of this variability is not certain, but examination of the parent SAR imagery and interferograms over Kotzebue Sound indicate that the surface of the ice loses coherence temporarily without any substantial horizontal motion. This coherence loss could be caused by surface flooding, which has been observed to be caused by heavy snow load in this region (Mahoney et al., 2021). Kotzebue Sound also has extensive areas of shallow water (≲2 m), in which the ice can repeatedly interact with the seafloor as the water level rises and falls under the influence of winds and tides. This process can result in flexural fracturing of the ice surface, which can also lead to coherence loss.

In the month of May, the landfast ice width difference between the two datasets is more consistently negative again, due to extensive areas where no landfast ice was identified by the InSAR-based method, but landfast ice was still present in both the Chukchi and Beaufort coasts in the EM2024 dataset. In particular, Kotzebue Sound never met the coherence threshold to be considered landfast ice during May of any season from 2017–2021. This consistent underestimation by the InSAR-based method is likely due to the alteration of the dielectric properties of the ice surface during the early stages of melt, which leads to the loss of coherence before any substantial motion of the ice.

3.2.2 Monthly mean apparent strain

Apparent strain fields were calculated from each of the 2,084 interferograms as described in Section 2.4.3. These were sorted into months, based on the date of the primary SAR acquisition and used to generate monthly mean fields of apparent strain (Figure 3-17 and Figure 3-18). Pixels with coherence values below 0.1 were excluded. Although there can be considerable variability between adjacent pixels, there is an overall tendency for lower apparent strain values (blue regions) to be found near the coast with higher apparent strains (yellow regions) found nearer the SLIE. This spatial distribution becomes more apparent as the landfast ice season progresses and another tendency emerges whereby the apparent strain in landfast ice tends to decrease over time. This tendency can be clearly seen in the probability distribution of average coherence values for each month (Figure 3-19), which shows that modal value of apparent strain decreases monotonically from month to month. This indicates that landfast ice becomes more stable the longer it persists.

The greater proportion of low phase gradient landfast ice pixels occurred in April and May. A difference between April and May is the presence of landfast ice along the Chukchi coast, specifically in Kotzebue Sound. The majority of landfast ice which is coherent during the month of May is along the Beaufort coast (Figures 3-17 and 3-18). The landfast ice which remains coherent in May is the most stable. While landfast ice is typically present along the Beaufort coast in June (Figure 3-7) no coherent pixels existed using the methodology described in Section 2.4.2.

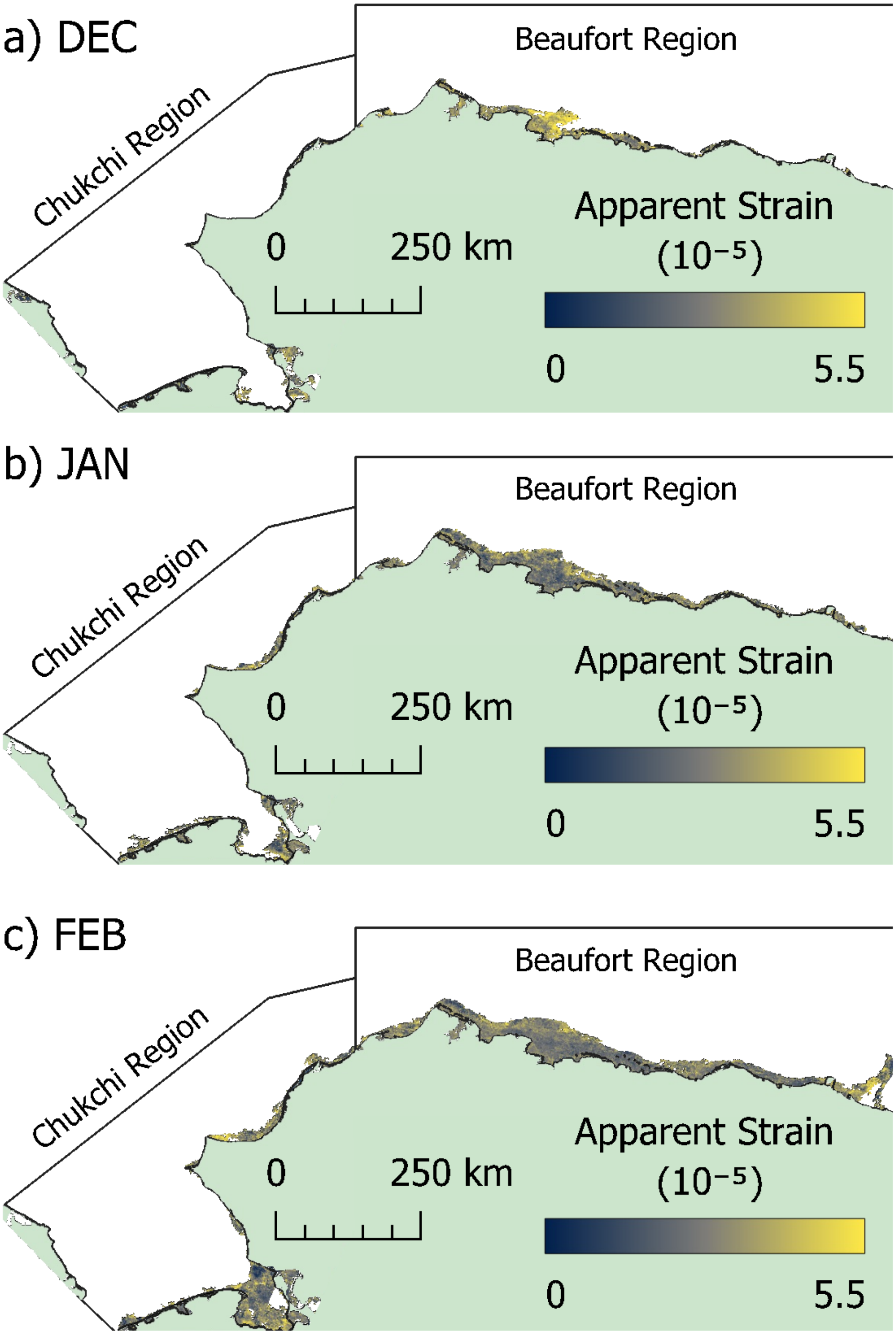

Figure 3-17: Monthly mean apparent strain from 2017–2021 for the months of a) December, b) January, and c) February.

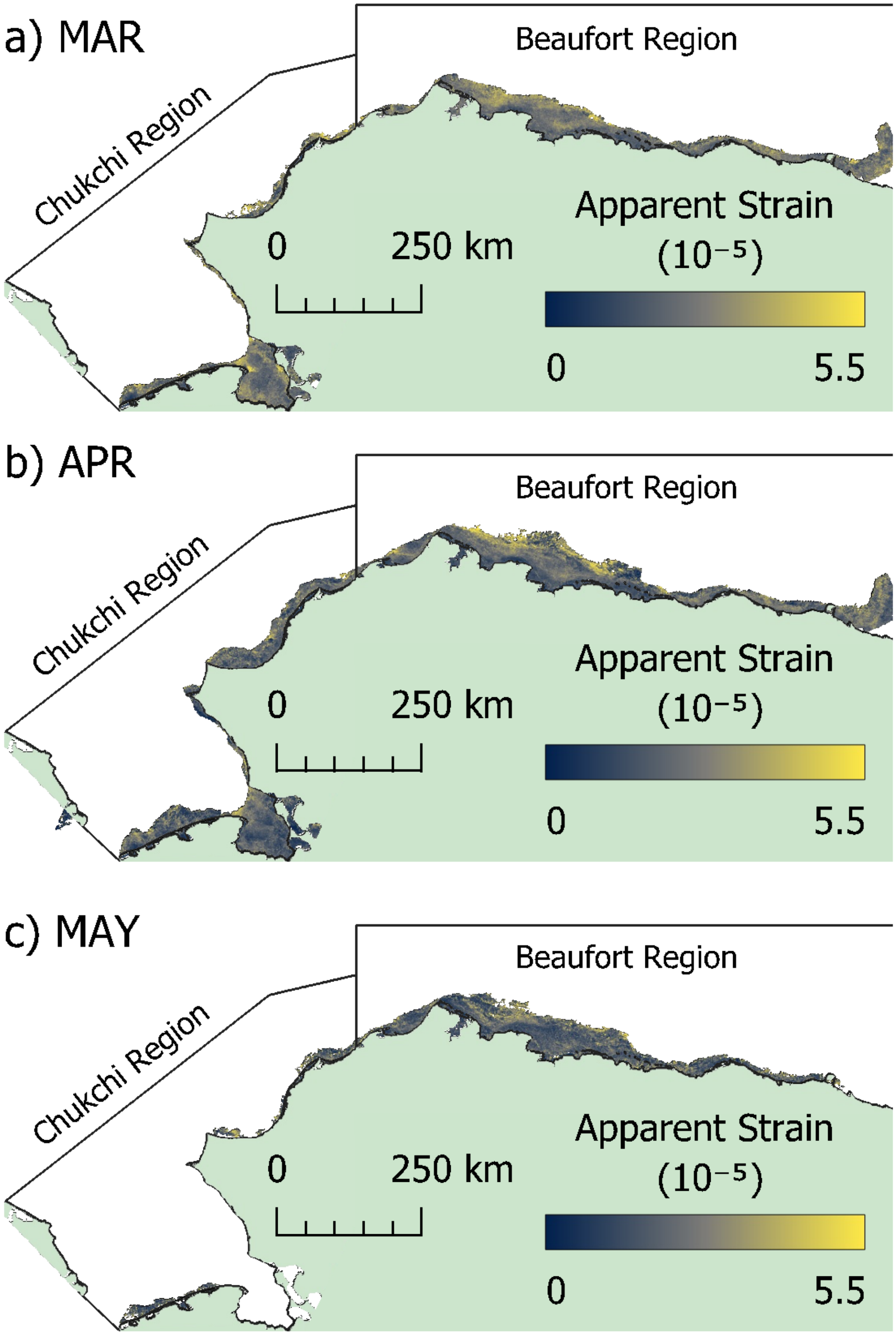

Figure 3-18: Monthly mean apparent strain from 2017–2021 for the months of a) March, b) April, and c) May.

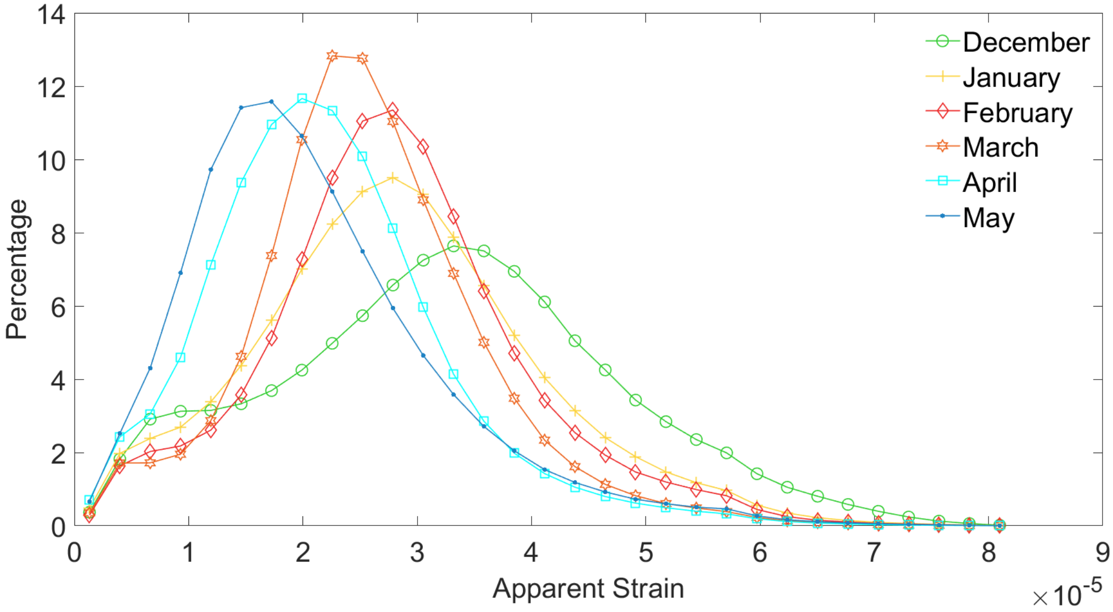

Figure 3-19: Distribution of average apparent strain during each month (December, January, February, March, April, and May) between 2017–2021.

3.2.3 Quantification of three landfast ice stability categories

Landfast ice present along the Beaufort coast is typically stable and approaching its seasonal maximum width during April. This is also the month for which Dammann et al., (2019) qualitatively defined landfast ice stability using InSAR. Hence, we used the distributions of April mean apparent strain in the three regions identified in Section 2.4.4 (bottomfast, sheltered, and not-sheltered) to establish strain thresholds for the 3 associated stability categories (bottomfast, stabilized, and non-stabilized). The distributions of apparent strain in each region have well defined and distinct modes (Figure 3-20), with the modal value for the bottomfast region being the lowest and that for the not-sheltered region being the highest. The bottomfast region distribution is right skewed while the other regions are approximately normally distributed. The right skew in the bottomfast distribution is the result of high apparent strains being present at the oceanward bottomfast ice boundary, likely associated with tide cracks. The distribution of the sheltered region was used to establish the upper and lower bounds for the bottomfast and not-sheltered regions respectably.

The 10th percentile of the sheltered region corresponds to a value of apparent strain of 1.0×10^{-5} and the point at which the proportion of pixels sheltered region exceeds that in the bottomfast region. Hence, we use this value as the threshold between bottomfast and stabilized ice. For threshold between stabilized and non-stabilized ice, we use the 90th percentile of the sheltered region distribution, which corresponds to an apparent strain of 2.3×10^{-5}. We note that this aligns with the mode of the not-sheltered distribution, rather than intersection between the sheltered and not-sheltered distributions. However, we expect that areas in the not-sheltered region may still have been stabilized, but by a grounded ridge rather than a permanent barrier island. This likely explains why the mode of the not-sheltered region is broader and is why we did not choose the intersection point of the sheltered and non-sheltered distribution as the threshold between stabilized and non-stabilized ice. These apparent strain thresholds can now be applied to results from single interferograms to identify areas of varying stability within the landfast ice.

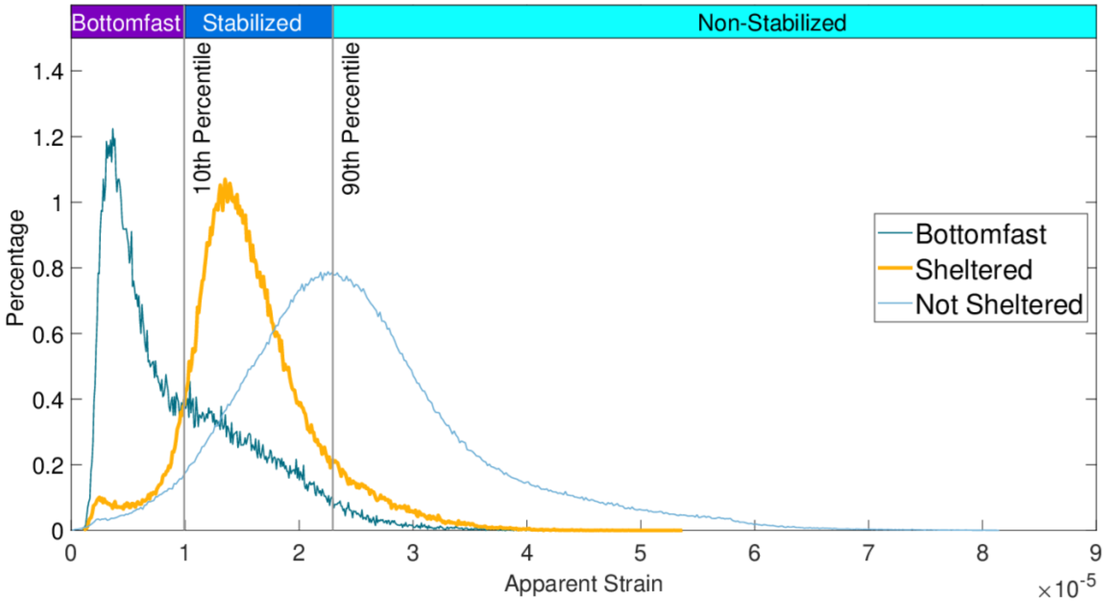

Figure 3-20: Distribution of April mean apparent strain during the period 2017–2021 in the areas identified as bottomfast, sheltered, and not-sheltered landfast ice.

To assess the accuracy of the apparent strain thresholds determined in Figure 3-20, we applied them to interferograms created from pairs of SAR images acquire in April 2017 similar to those used by Dammann et al., (2019) along the Beaufort coast in Alaska. The exact SAR pairs used by Dammann et al., (2019) were not available through ASF's Vertex portal and so we selected overlapping pairs that were acquired within 12 days. By color-coding apparent strain values according to these thresholds, we can map the resulting distribution of stability categories within the landfast ice (Figure 3-21). The areas defined as bottomfast ice by this method are more expansive than the areas Dammann et al., (2019) identified as bottomfast. This discrepancy is large, but we can attribute it to abnormally low phase gradient across the region at this particular time. The corresponding apparent strain throughout Elson lagoon is considerably lower than the mean value for this month (Figure 3-17b) and falls within range typically found in bottomfast ice. The boundary between stabilized and non-stabilized landfast ice agrees

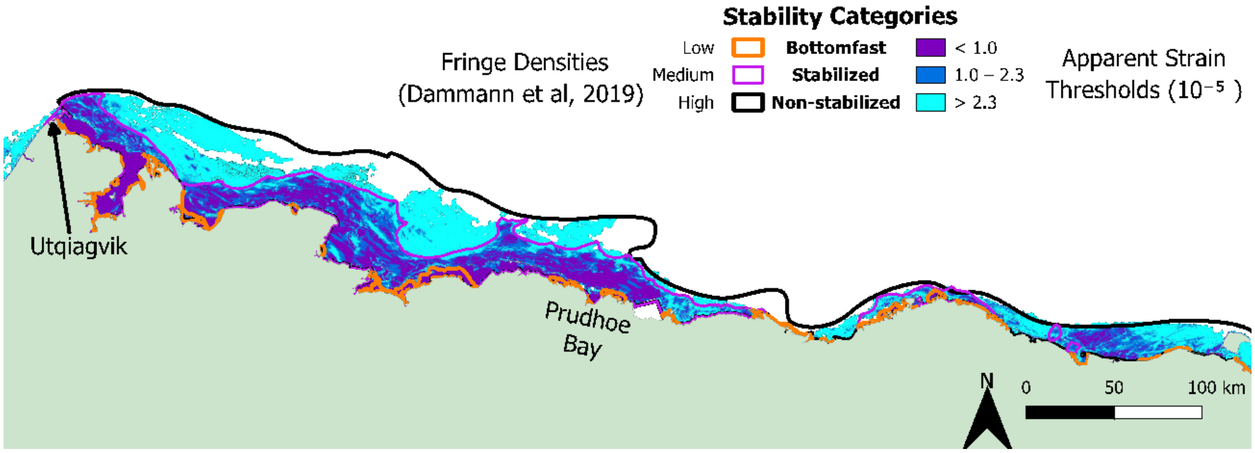

Figure 3-21: Categorized landfast ice stability derived from apparent strain threshold applied to interferograms from April 2017 corresponding to those used by Dammann et al., (2019). Solid shaded areas indicate the stability categories quantitatively derived from apparent strain. Outlined areas indicate areas identified qualitatively by Dammann et al., (2019).

more closely between our quantitative approach and the qualitative method used by Dammann et al., (2019), which provides some validation for our apparent strain threshold of 2.3×10^{-5}.

3.3 In situ landfast ice observations

3.3.1 Point Hope landfast sea ice mass balance observations

As summarized in Table 2-3, SIMBs were deployed in landfast ice near Point Hope in 2020 and 2022. Unfortunately, the bottom sounder on the SIMB deployed in 2020 malfunctioned, but we were able to estimate the ice thickness from the temperature profile, following the method outlined by Gough et al., (2012). Data from both deployments (Figure 3-22) show sustained growth through March and April, but otherwise there are marked differences between the two landfast ice seasons.

In 2020, a maximum ice thickness of 0.95 m was reached around May 1 and bottom melt began 10 days later on May 11, which coincided with the arrival of comparatively warm water above its freezing point at the base of the ice (Figure 3-22a). From this point forward, it was not possible to estimate the position of the ice bottom from the temperature profile. The snow pack started warming and thinning on May 8 and had completely melted by May 20, when surface melt began. By May 25, a total of 6 cm of surface melt had occurred before the SIMB appeared to shift vertically down, giving rise to an apparent rapid increase in snow depth as the snow sounder got closer to the ice surface. On June 8, 2020, the SIMB began drifting due to detachment of the landfast ice. This event was identified by the Global Navigation Satellite System (GNSS)-derived track of the buoy, but it is also marked by an abrupt warming of the water column throughout the full depth of the SIMB. By comparison, in 2022, the ice was already 1.12 m thick by the time it had started thinning in 2020 (May 1) and it continued growing until the buoy was recovered on May 26. By this time the ice had reached a thickness of 1.16 m. Snow melt in 2022 began on May 21, by which date in 2020 the snow had completely melted and surface ablation of the ice had started.

Although we did not intend to let the SIMB deployed in 2020 drift away when the landfast ice detached, it provided valuable data of the thermodynamic processes leading up to the detachment and disintegration of the landfast ice, which was fortuitously under frequently clear skies allowing it to be captured by PlanetScope and Landsat imagery (Figure 3-23). On May 19, the day before the SIMB indicated complete melting of the snow pack, PlanetScope imagery shows the landfast around the SIMB was largely still snow covered (Figure 3-23a). By May 24, areas of bare ice or melt ponds hundreds of meters in size are evident (Figure 3-23b), consistent with approximately 4 cm of surface melt observed by the SIMB. On June 7, the day before the SIMB was set adrift, many ponds appear to have drained and a refrozen fracture can be seen close to the SIMB location, revealed by snow melt (Figure 3-23c). The next clear-sky image on June 9 shows that the landfast ice has retreated back to location of the refrozen fracture (Figure 3-23d). At the time this image was acquired (18:44 UTC), the SIMB had drifted approximately 20 km southward, but it's GNSS position began to become intermittent, suggesting the buoy may have been tilting in waves. This makes is difficult to identify the buoys precise position in the image (Figure 3-23e), but there are no easily resolvable ice floes in the region, suggesting that the SIMB was drifting in open water at the time and probably since the detachment event. The SIMB continued to report its position for another 11 days as it drifted through largely open water containing isolated fragments of landfast ice (Figure 3-23f).

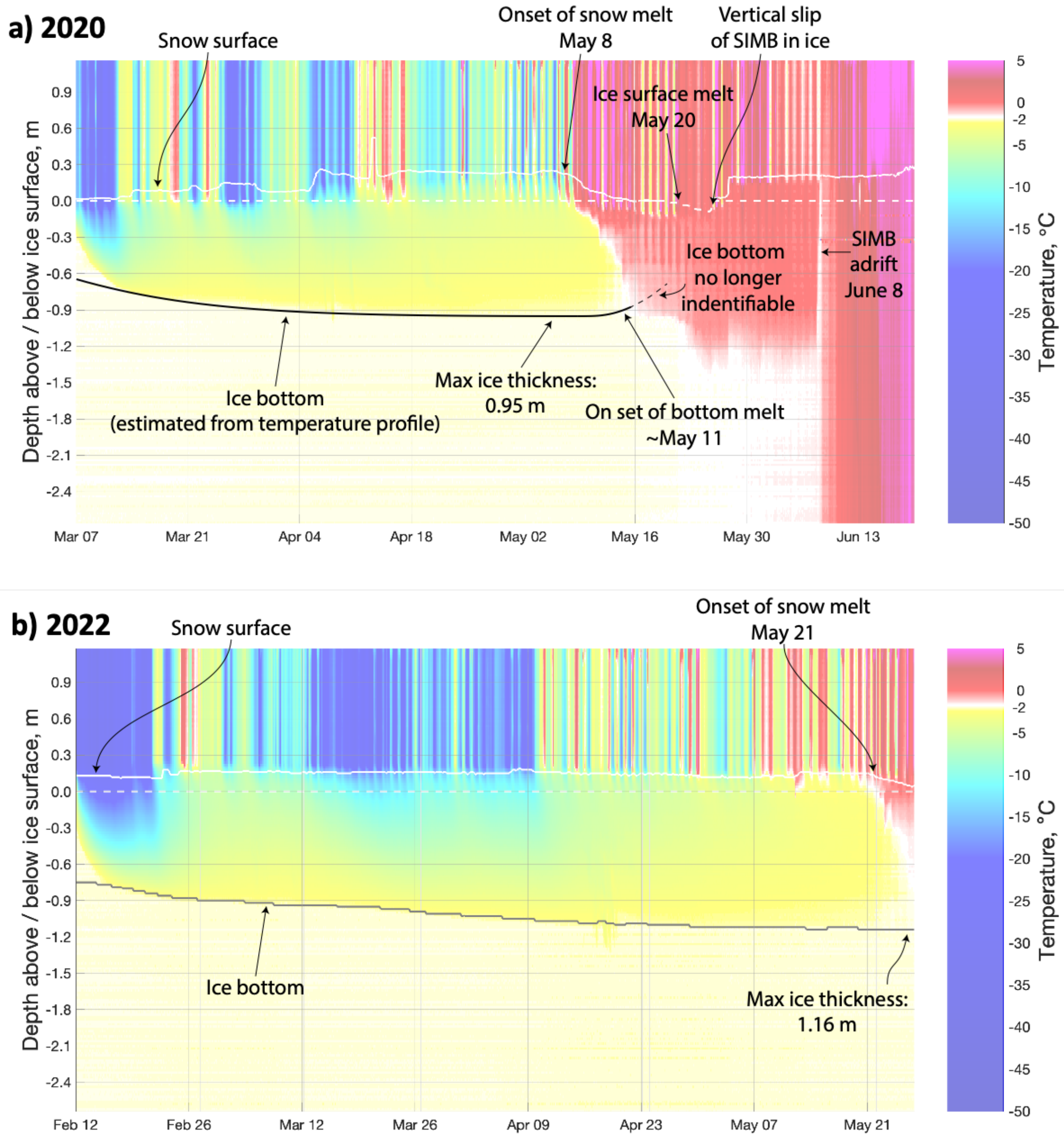

Figure 3-22: Snow depth, ice thickness, and temperature profile data from SIMBs deployed in landfast ice near Point Hope in a) 2020 and b) 2022.

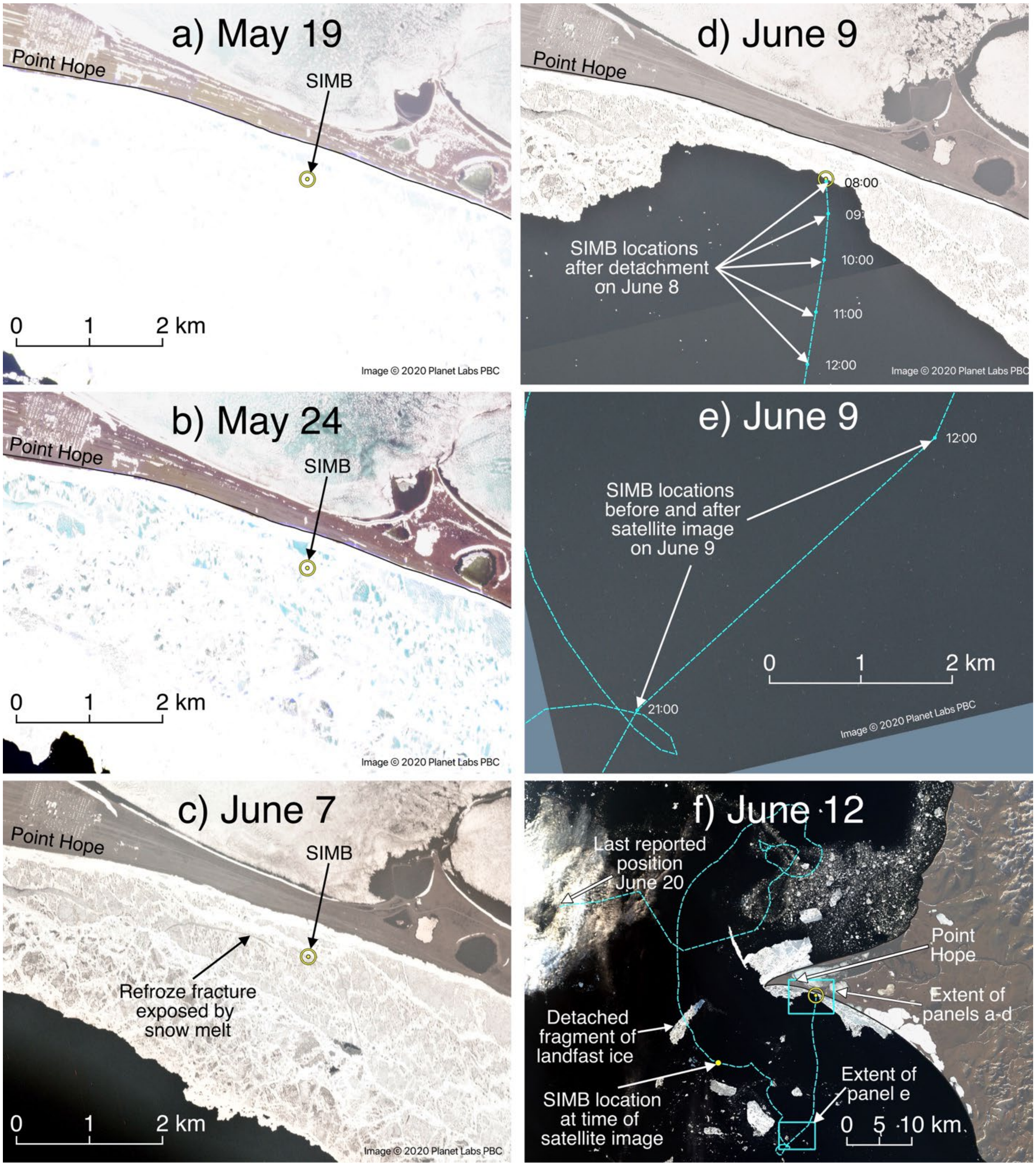

Figure 3-23: (a–e) PlanetScope imagery and (f) Landsat-9 imagery capturing the late season evolution of the landfast ice near Point Hope and the trajectory of the SIMB deployed in 2020.

3.3.2 Utqiagvik landfast sea ice mass balance observations

SIMBs were deployed in the landfast ice near Utqiagvik in 2021, 2022, and 2024 (Figure 3-24). However, due to a thermistor string malfunction, temperature profile data are not available from 2021 and, as noted in Section 2.5.1, damage by a polar bear cut the SIMB record short prematurely in early March 2022. Nonetheless, we can still usefully compare the early winter ice growth between 2022 and 2024 and the

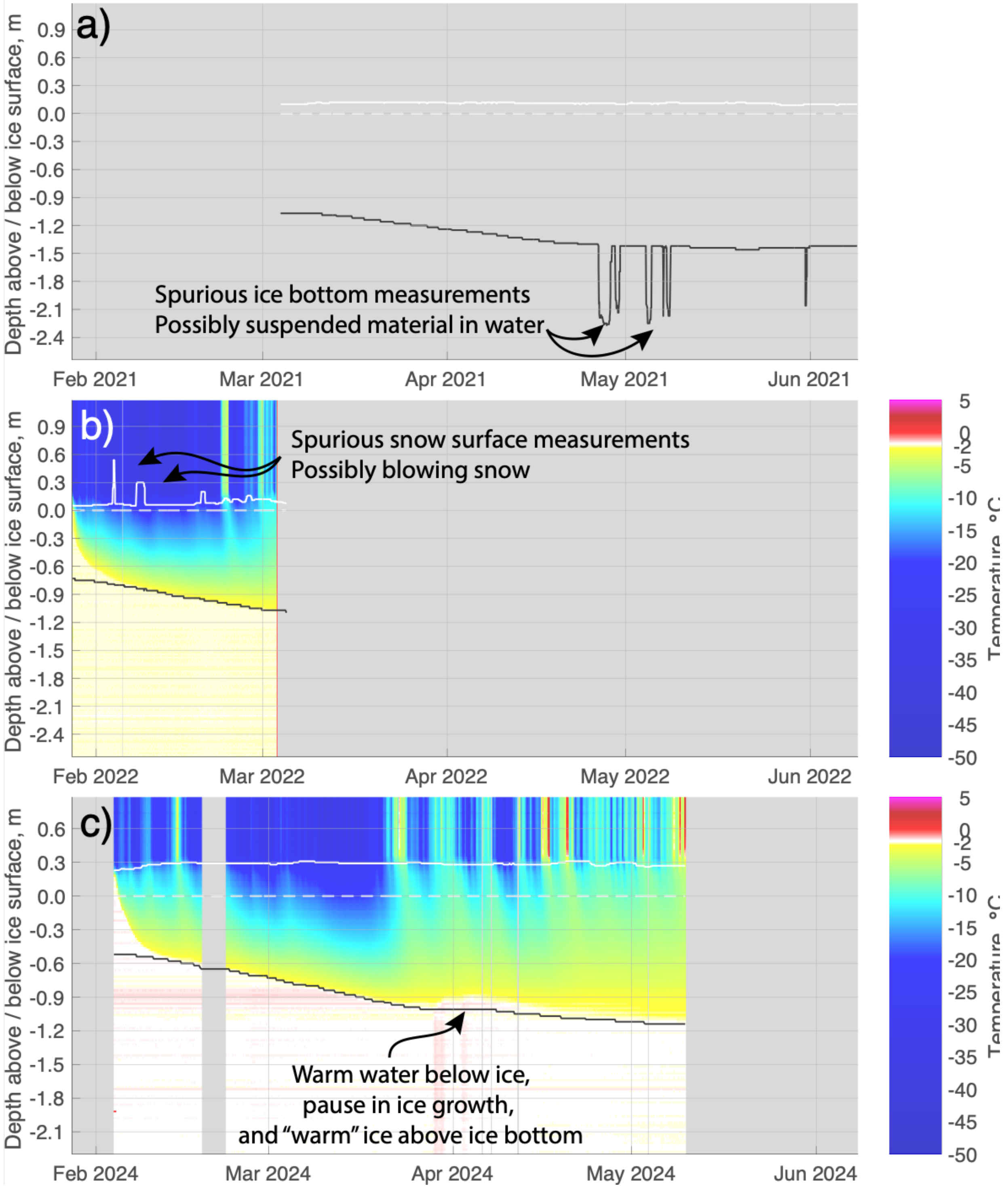

Figure 3-24: SIMB data from 3 deployments in landfast ice near Utqiagvik in a) 2021, b) 2022, and c) 2024.

late winter ice thicknesses and snow depths between 2021 and 2024. Notably, the sea ice was some 30 cm thinner throughout February 2024 than it was during February 2022, and during April and May the landfast ice was approximately 20 cm thinner in 2024 than during the same period in 2021. These differences can be partly explained by the greater snow depth in 2024 than in either 2021 or 2022, which would have insulated the underlying sea ice and slowed growth. However, there is also a notable pause in ice growth in late-March to early-April 2024 associated with water temperatures up to -1.4 ºC, slightly above the expected freezing point (Figure 3-24c). During this time, temperature sensors up to 6 cm above the location of the ice bottom detected by the bottom sounder reported water temperature similarly above the freezing point. This is similar to the situation that occurs immediately after deployment as the hole around the SIMB freezes in. In this case, it suggests that the ice immediately around the buoy may have melted, possibly due to turbulence-enhanced heat flux around the protrusion of the buoy below the ice bottom. This raises the possibility that increased ocean heat flux could also have contributed to the reduced landfast ice thickness measured in Utqiagvik in 2024.

3.3.3 Under-ice ADCP measurements

The one ice-tethered ADCP that was successfully deployed and recovered recorded under-ice velocity data near Utqiaġvik from January 29 to June 10, 2022 (Figure 3-25). The instrument was set to record velocity data in 150 5-cm vertical bins. Ensemble averages consisted of two pings and were reported in 1-minute increments. Data was generally available from 0.6 m to 5.5 m above the transducer, with data quality being highly dependent on the amount of suitably-size backscatterers present in the water column. A lack thereof resulted in periods of insufficient data quality being rejected by the onboard processing of the ADCP. In order to reduce noise, the raw velocity data was averaged hourly and in 25 cm vertical bins.

Pronounced current variability was observed on semidiurnal timescales, with a period consistent with the semidiurnal M2 tide, and on sub-inertial timescales of 2–7 days on two separate occasions (Figure 3-25c-e). Subinertial variability with a period of 2–3 days occurring between 20 February and 28 February was strongly baroclinic (Figure 3-25c,d) and was associated with pronounced upward velocities close to the transducer (Figure 3-25e). ERA5 wind data indicated that these baroclinic velocities were likely associated with a passing storm (Figure 3-25b). Transducer temperature exhibited relatively strong variability during this time (Figure 3-25a), suggesting possible advection of offshore waters by the baroclinic currents. A second period of subinertial velocity variability (this time with a barotropic vertical structure) occurred between 15 May and 22 May. Its period was slightly longer at 5–7 days with no apparent wind or temperature association.

By time-integrating the depth-averaged velocity over 2-week periods, we can visualize the direction and scale of spatial scale of water transport under the ice at the location of the ADCP (Figure 3-26). For most of the winter, the currents are relatively weak and change direction regularly such that 14-day integrated current amounts to less than 10 km of transport, with a general tendency for westward motion. However, in early May there is a pronounced change in the direction and magnitude of the flow such that the 14-day integrated current velocities exceed 10 km for the remainder of the record (Figure 3-26h,i). This may represent a mechanism to transport water under the landfast ice from more southerly latitudes where there may have been more opportunity to absorb more solar energy. Upwelling of warm water seems an unlikely explanation as this is usually associated with eastward flow (e.g., Hirano et al., 2016).

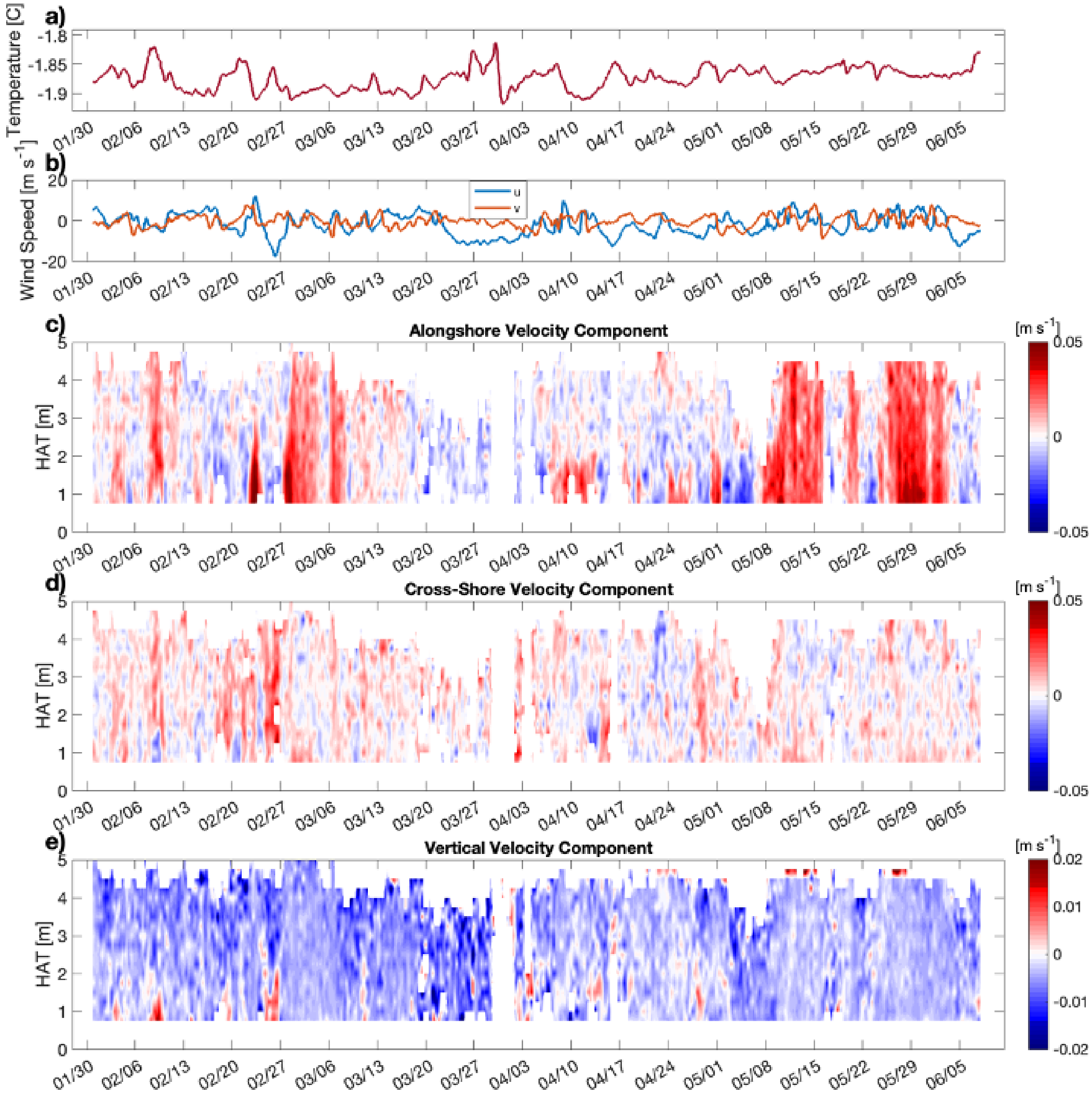

Figure 3-25: Timeseries of data for the ADCP deployed under landfast sea ice near Utqiagvik in 2022. a) Water temperature measured by the ADCP; b) ERA5 wind velocity interpolated to ADCP location; c) Zonal current velocity profiles; d) Meridional current velocity profiles; and e) Vertical current velocity profiles.

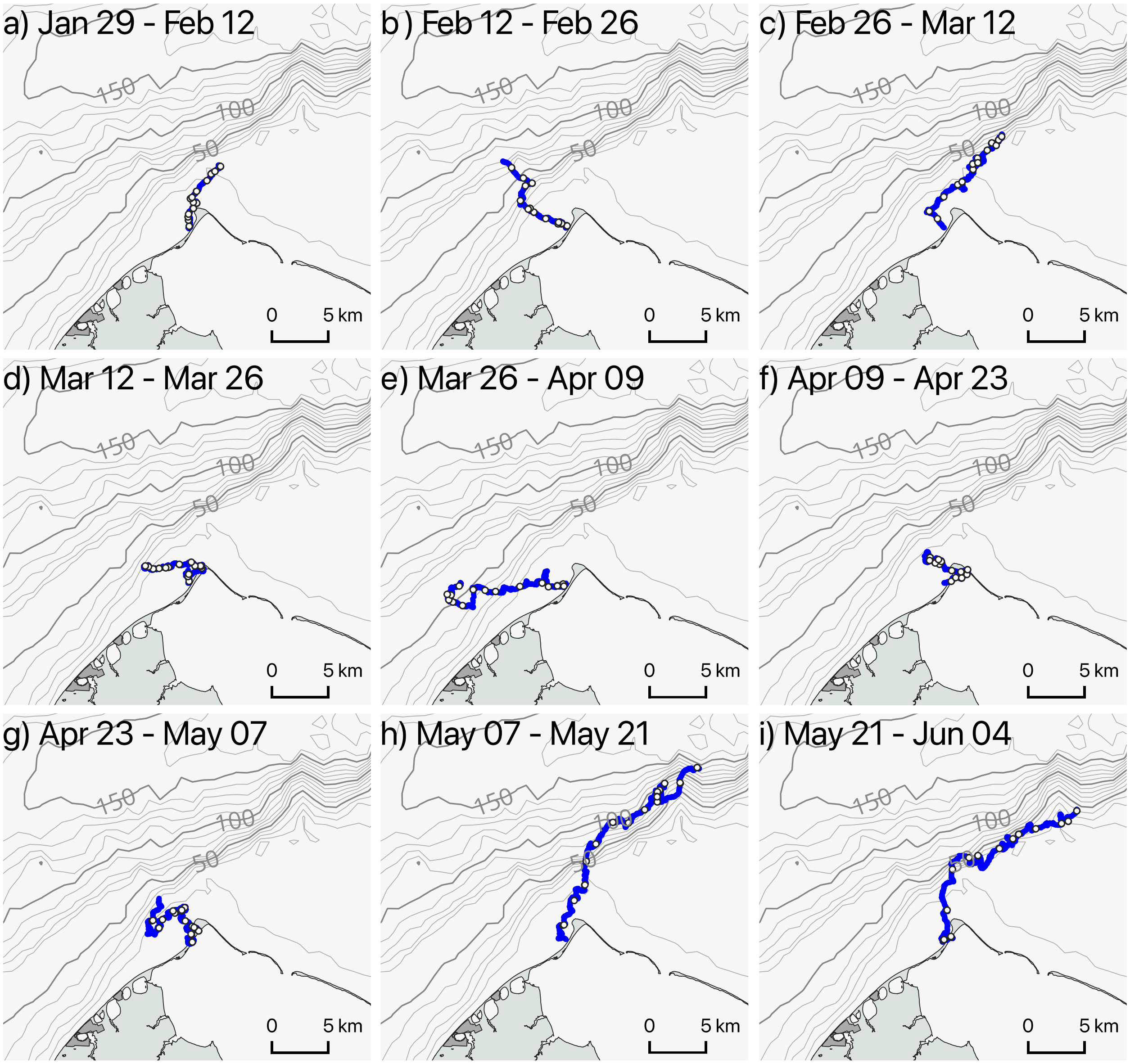

Figure 3-26: 14-day progressive vector plots derived from depth-average current velocity data from the ADCP deployed near Utqiagvik in 2022. White circles indicate the progressive pseudo-position at noon UTC each day. Bathymetry is given in meters

Time-averaged under-ice current velocities (Figure 3-27) were generally small, with average currents on the order of 0.6 cm s^{-1} flowing in a northward direction, which is almost parallel to the coastline that is oriented approximately SSW-NNE in the vicinity of the ADCP deployment. The vertical structure of the cross-shore flow was mostly barotropic, while a slight intensification lower in the water column towards the transducer was likely associated with the baroclinic velocity signals mentioned earlier. The intensification in the upper 0.5 m underneath the ice is likely an artifact due to data sparsity during aforementioned periods of insufficient data quality, and care must be taken when interpreting this intensification physically.

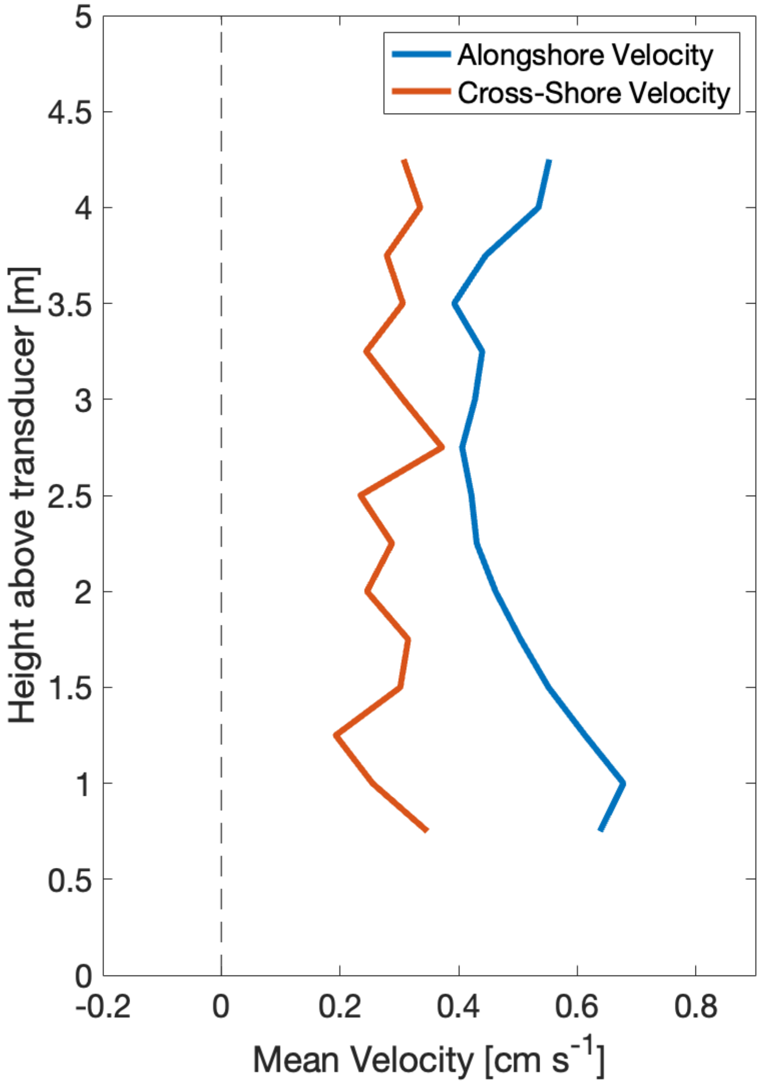

Figure 3-27: Time-average vertical profiles of zonal and meridional currents under the landfast ice near Utqiagvik, measured in 2021.

3.4 Cyclone Activity in the Alaska Arctic OCS

Composite anomalies, which is an average of sea level pressure on all breakout days, are shown in Figure 3-28. The composites for both the Beaufort and Chukchi Sea events reveal an area of anomalous low pressure centered in the Bering Sea. This general pattern can be indicative of storm activity in the Bering Sea region during the days when landfast breakouts occurred. However, the areas of statistically significant patterns were limited implying that there is some variability among the strength or position of storms during these events. SOMs (Section 2.6.2) were employed to look for possible groupings of spatial patterns in sea level pressure, storm tracks and winds among events.

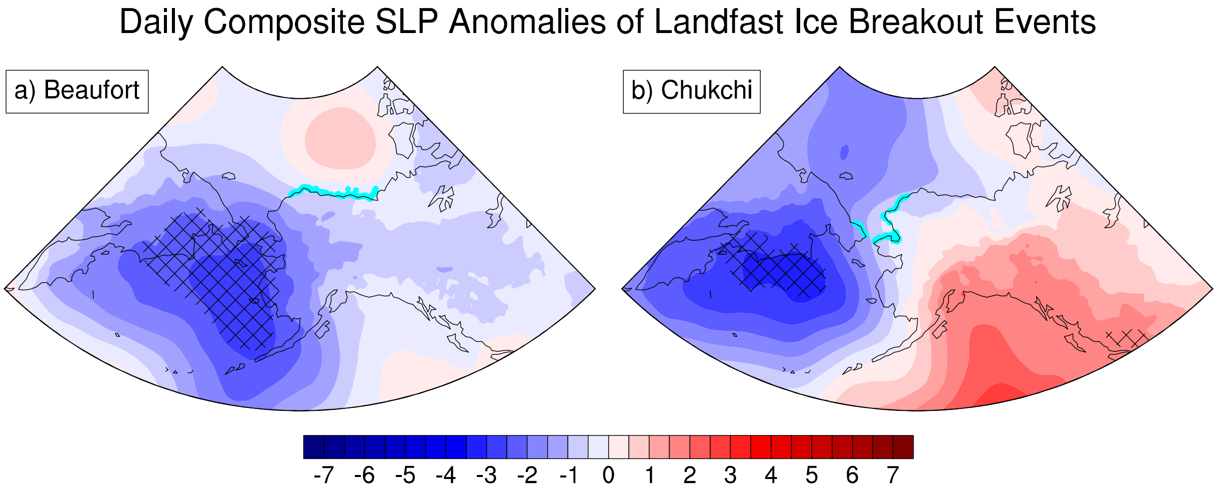

Figure 3-28: Daily composite anomalies of sea level pressure on landfast breakout days 1997[3]–2023 for the (a) Beaufort and (b) Chukchi Seas. Units are in hPa and regions significant at the 95% level according to a t-test are cross-hatched. Anomalies relative to 1991–2020 reference period. Locations of breakout events shown in cyan.

The 4×5 SOM matrix of nodes is shown in Figure 3-29. These 20 nodes reveal the relatively common nature of storms in and around the Alaska region during January–April, with areas of low pressure found in the domain in each node. Over the full period, no SOM node stood out as being more frequent than others. The relative frequency of each node occurring within 0–5 days prior to each breakout day are shown in Table 3-2. Node 19 has the highest frequency of occurrence of the sea level pressure patterns associated with breakouts for both seas. This node is most associated with low pressure in southern Bering Sea. Over the 1997–2022 period there is a breakout event in Beaufort or Chukchi Sea 31% or 21% of the time when it occurs, respectively. The second most frequent SOM pattern for the Beaufort Sea is Node 15 and for the Chukchi it is Node 11. To better understand potential meteorological drivers of the breakouts associated with these SOM patterns, the composite anomalies of storm track density and wind speeds are shown in Figures 3-30 and 3-31, respectively. Node 19 is associated with storms tracking through the Bering Sea. High pressure of the Arctic Ocean results in a pressure gradient that gives rise to anomalously strong easterly winds across the Beaufort turning more northward in Chukchi Sea. Nodes 14–15 are also similarly linked with Bering Sea storm tracks but with the strongest positive wind anomalies in Chukchi Sea. Node 11 is tied to weaker winds over the Chukchi Sea region.

---

[3] As noted earlier in Section 2.6.2, breakouts are defined as only occurring between January and April. Since the EM2024 dataset begins in October 1996, the first year in the breakout catalog is 1997.

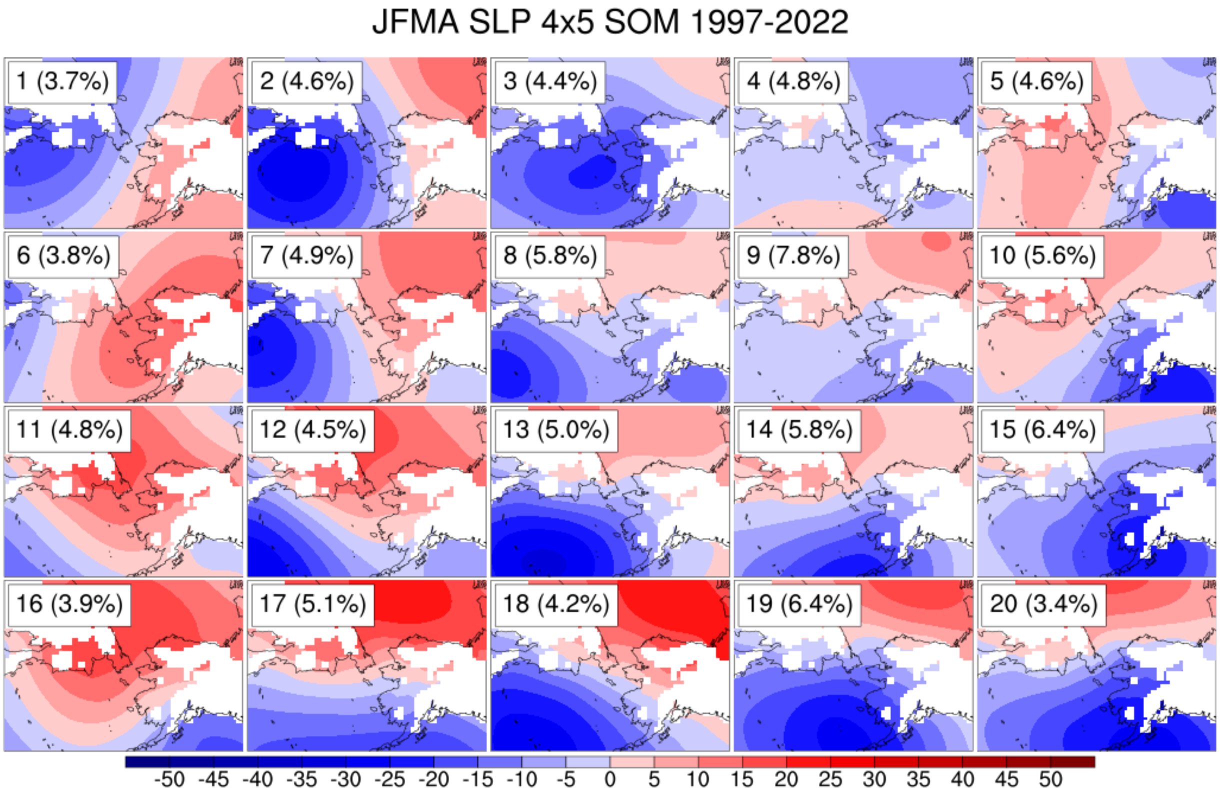

Figure 3-29: Self-organizing map 4×5 matrix of daily sea level pressure anomalies for January-April over 1997–2022. The units are in hPa. The node number is shown on each panel along with the frequency of occurrence over the record. White areas indicate elevations greater than 500 m which are masked (see Section 2.6.2).

Table 3-2: Percent of occurrence of each SOM node (corresponding to Figure 3-29) within 0–5 days prior to the landfast breakout events for the Beaufort and Chukchi regions. The percentage was calculated by dividing the number of breakout events associated with each node by the total number events.

Beaufort

2.44	4.59	4.30	4.59	1.87
2.73	4.73	4.02	5.16	3.30
3.73	4.59	5.31	7.03	7.60
5.45	5.74	6.03	9.04	7.75

Chukchi

5.88	6.43	4.60	5.15	4.04
4.04	3.68	6.25	4.96	5.15
5.88	3.86	5.51	6.99	4.04
2.57	4.04	4.23	6.07	6.62

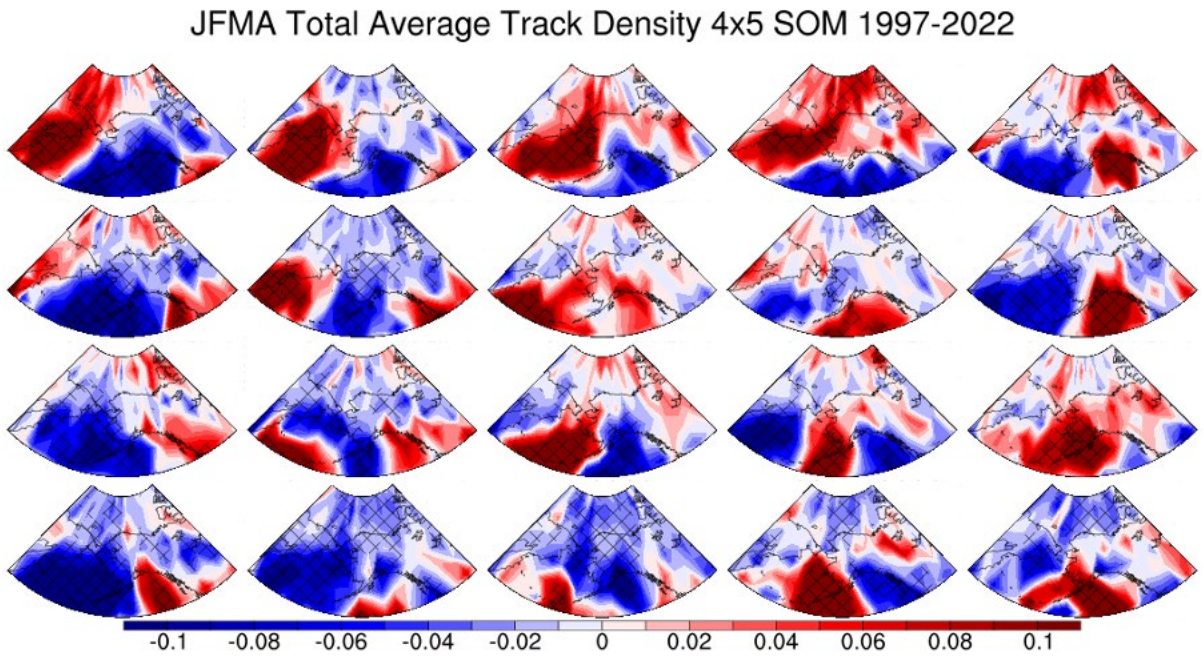

Figure 3-30: Composite anomalies of total storm track densities associated with the days of each SOM node corresponding to Figure 3-29. The units are in number of storms per day and regions significant at the 95% or greater level according to a t-test are cross-hatched. Anomalies relative to 1991–2020 reference period.

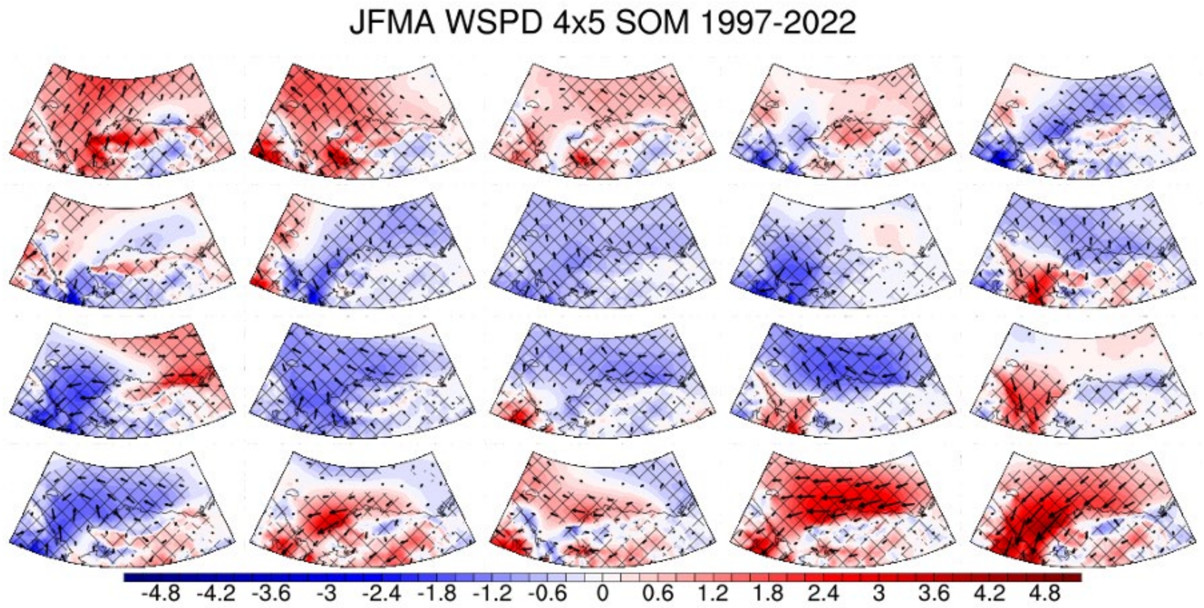

Figure 3-31: Composite anomalies of wind speed (shaded) and direction (vectors) associated with the days of each SOM node corresponding to Figure 3-29. The units of wind speed are in m s^{-1} and regions significant at the 95% or greater level according to a t-test are cross-hatched. Anomalies relative to 1991–2020 reference period. The longest wind vectors are associated with 4 m s^{-1} wind anomalous speeds.

3.5 PAMS model results

3.5.1 Pan-Arctic ice concentration

As referenced in Section 2.7.5, we have performed a total of 80 model runs, each producing a 25-year simulation of the Arctic domain and . Many of these runs were aimed at reducing biases in the temperature and salinity fields and overall ice cover. These biases are quite sensitive to the vertical mixing in the model, as well as to the restratification parameterizations of Fox-Kemper et al., (2011; 2008) and Bodner et al., (2023). We evaluated overall ice extent for model runs 51 and 56 (see Table 2-7) and compared the results against daily satellite estimates, with both runs showing a bias towards too much winter ice (Figure 3-32). Run 56 also has too much ice in the summer. Though there are biases, they are not worsening in time, unlike a similar run which used the ERA5 forcing (not shown) instead of JRA55-do. The ERA5 run with the increasing sea ice extent also exhibited an increasing landfast ice extent.

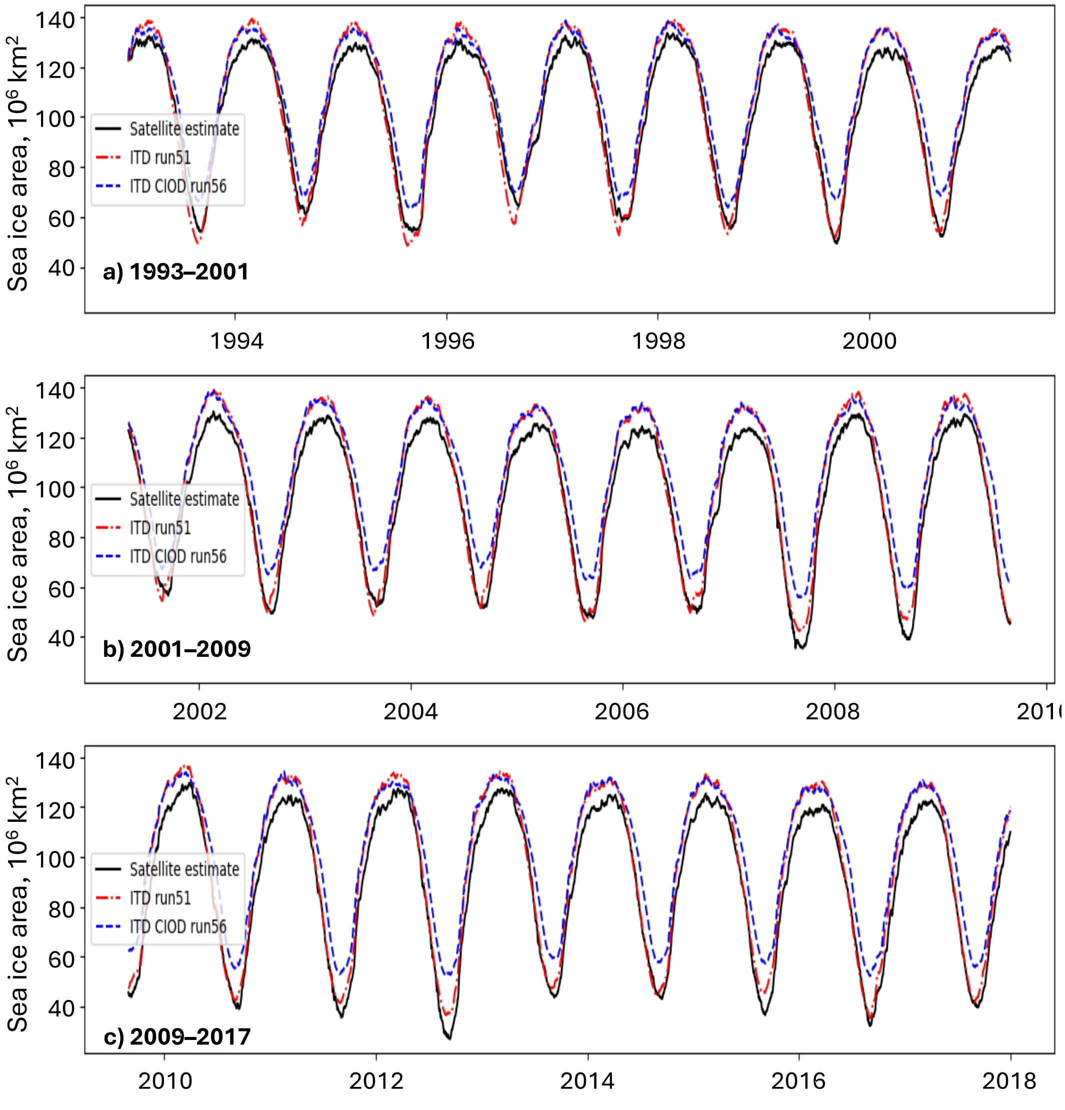

Figure 3-32: Comparison of the PAMS model's ice extent compared to the satellite estimates of Comiso et al., (2014) in units of millions of square kilometers. The 25-year span of the simulation is split into thirds for clarity. As described in Section 2.7.5, model runs 51 and 56 differ primarily in the use of an experimental ice-ocean coupler (CIOD) in run 56.

3.5.2 Pan-Arctic Ocean evaluation

One of the metrics we have been using to evaluate the PAMS model is to compare the March mixed-layer depth with that of de Boyer Montégut et al., (2004). They picked a mixed-layer depth criterion of a density difference of 0.003 kg m^{-3}, one of the metrics that MOM6 can write out. Figure 3-33 shows that the model has many of the same patterns, with a mixed layer of less than 50 m in the central Arctic, around 100 m in the North Pacific, and with patches of deep mixing south of Greenland and Iceland. While there are slight variations from one run to the next, there are persistent biases of well over 100 m, with some variability in the strength and exact location of the biases.

Another metric is to compare to the World Ocean Atlas (WOA) 2018 "decadal" averages for 1995 –2004 and 2005–2017. Figures 3-35–3-36 show the difference between the PAMS model and WOA for both temperature and salinity and for both decades. We here examine both the surface and the 100 and 200 m depths. The surface temperature of the Greenland-Iceland-Norwegian (GIN) Seas is persistently biased too cold in the model while the North Atlantic and North Pacific are biased warm, getting warmer in the second decade. The subsurface temperature biases echo the patterns in the mixed-layer biases, with too deep mixing bringing cold water down off the Norwegian coast and too shallow mixing preserving the warm subsurface water off the Northeast Greenland coast.

For the salinity, we have a persistent bias of too much salt at the surface in the central Arctic basin. We have surface salt restoring, but not under the ice. One theory for the excess salt under the ice is that of Nguyen et al., (2009). The idea is that in the model, when sea ice is formed in winter, the ice model grows ice, taking water from the ocean model. It leaves behind most of the salt, leaving it at the surface of the ocean. In reality, the ice would be forming in open leads covering at most 1% of the surface ocean and the salt should be rejected in brine plumes which would sink to the bottom of the mixed layer, entraining fluid as it goes.

A third metric was introduced by Dr. Wilbert Weijer in an Interagency Arctic Research Policy Committee (IARPC) session on Arctic ocean biases. He asked for time- and spatially-averaged profiles for the two Arctic basins delineated by the yellow and gold curves in Figure 3-37. In May 2023 (run 27), our PAMS model had one of the larger temperature biases in the eastern basin. In order to discover the timescale of this temperature drift, we have made plots such as those shown in Figures 3-38–3-41. The eastern basin has warm Atlantic layer water inflowing at roughly 300 m depth, mixing and deepening to 400 m as it progresses around to the western basin. The WOA profiles show some warming from one decade to the next, but nowhere near as much as in some of the model runs, including that of GLORYS.

For salinity, the most notable feature is the too-salty surface bias in the western basin, consistent with our surface salt bias under the ice. This feature is also seen in the GLORYS profiles. Surprisingly, adding the surface salinity restoring to a climatology has increased that salinity bias while simultaneously reducing the temperature bias. The changes between runs 27 and the more recent ones include this surface salinity restoring, turning off the bottom boundary layer, and introducing the mixed layer restratification from either Fox-Kemper (2011; 2008) or Bodner (2023). Run 73 also has the shear mixing dialed down with a new LZ_RESCALE option.

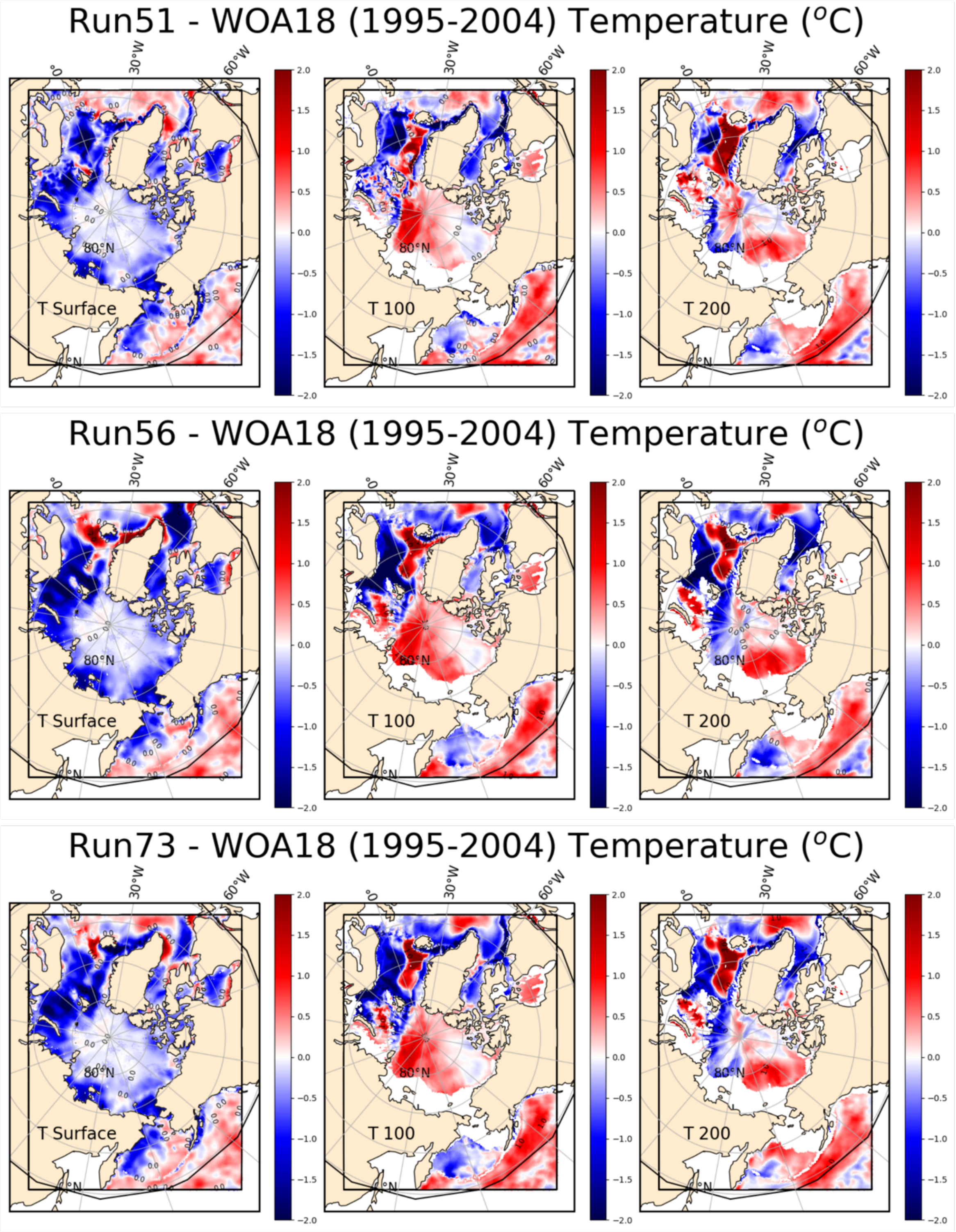

Figure 3-33: Difference between the PAMS model temperature World Ocean Atlas 2018 for the decade 1995 – 2004. On the left is the surface, middle is at 100 m depth and on the right is 200 m depth. Three simulations are shown, with run 51 at the top, run 56 in the middle and run 73 on the bottom.

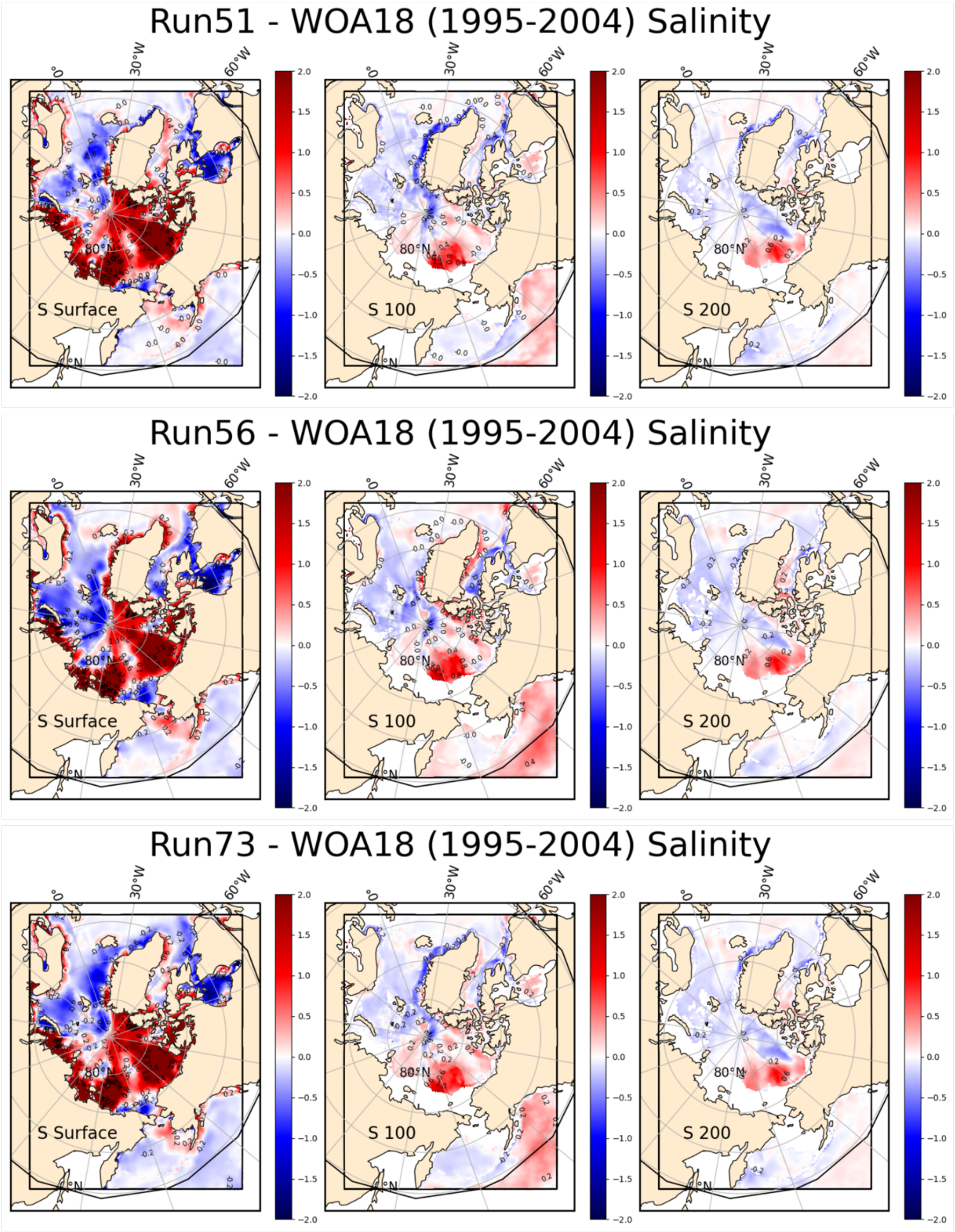
Run51 - WOA18 (1995-2004) Salinity

Run56 - WOA18 (1995-2004) Salinity

Run73 - WOA18 (1995-2004) Salinity

Figure 3-34: Difference between PAMS model salinity World Ocean Atlas 2018 for the decade 1995 –2004. On the left is the surface, middle is at 100 m depth and on the right is 200 m depth. Three simulations are shown, with run 51 at the top, run 56 in the middle and run73 on the bottom.

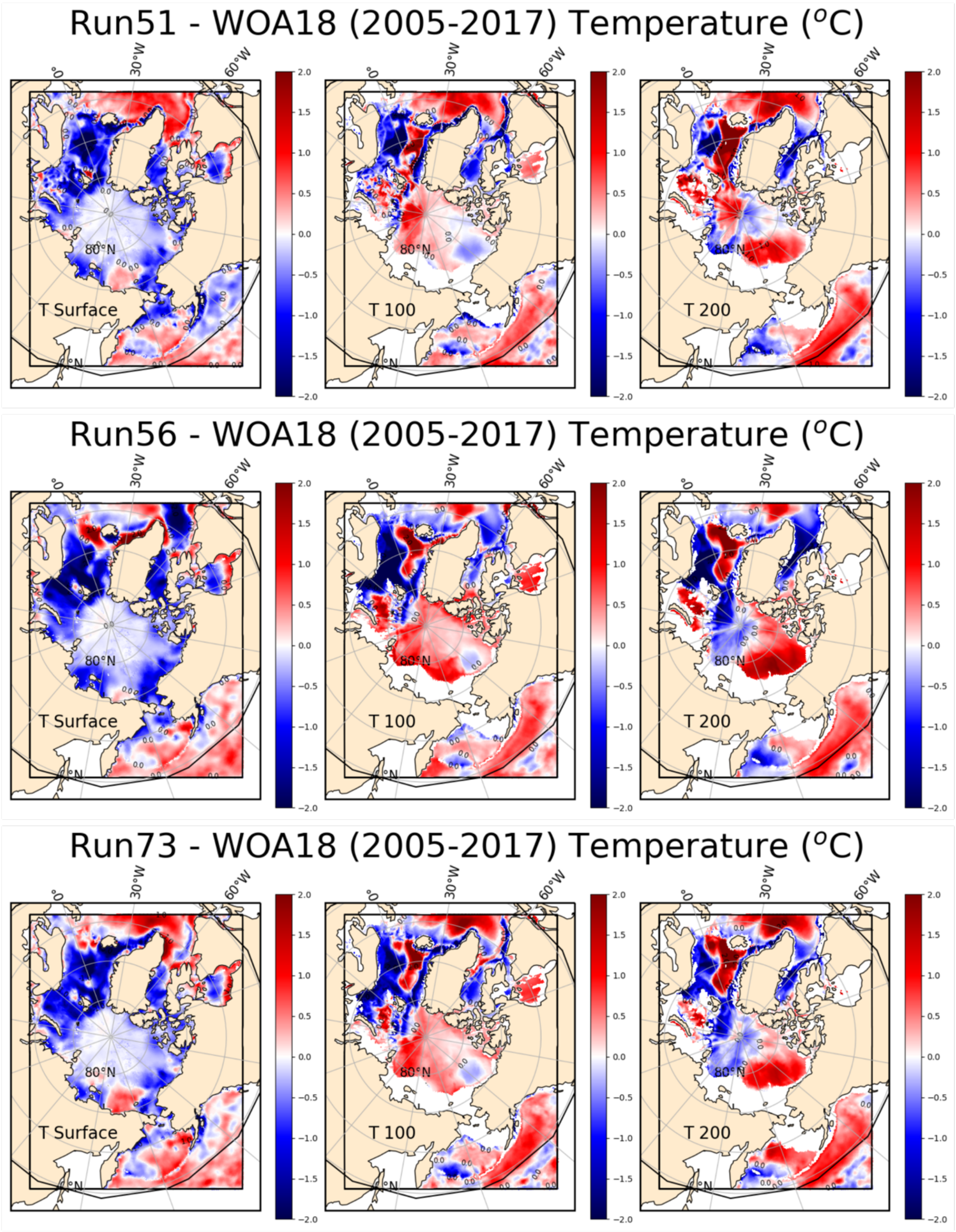

Figure 3-35: Difference between the PAMS model temperature World Ocean Atlas 2018 for the decade 2005 – 2017. On the left is the surface, middle is at 100 m depth and on the right is 200 m depth. Three simulations are shown, with run 51 at the top, run 56 in the middle and run73 on the bottom.

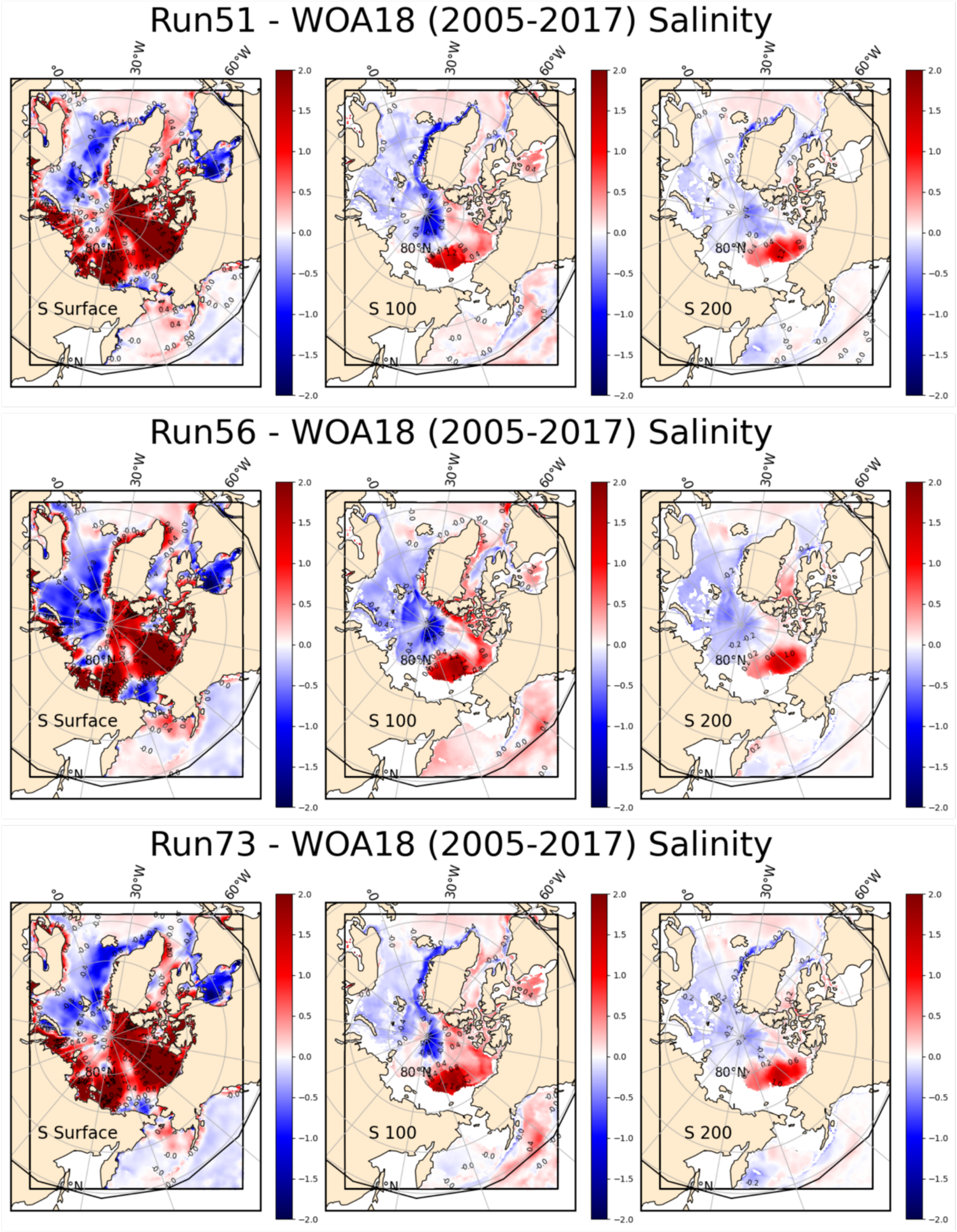

Figure 3-36: Difference between the PAMS model salinity World Ocean Atlas 2018 for the decade 2005 –2017. On the left is the surface, middle is at 100 m depth and on the right is 200 m depth. Three simulations are shown, with run 51 at the top, run 56 in the middle and run73 on the bottom.

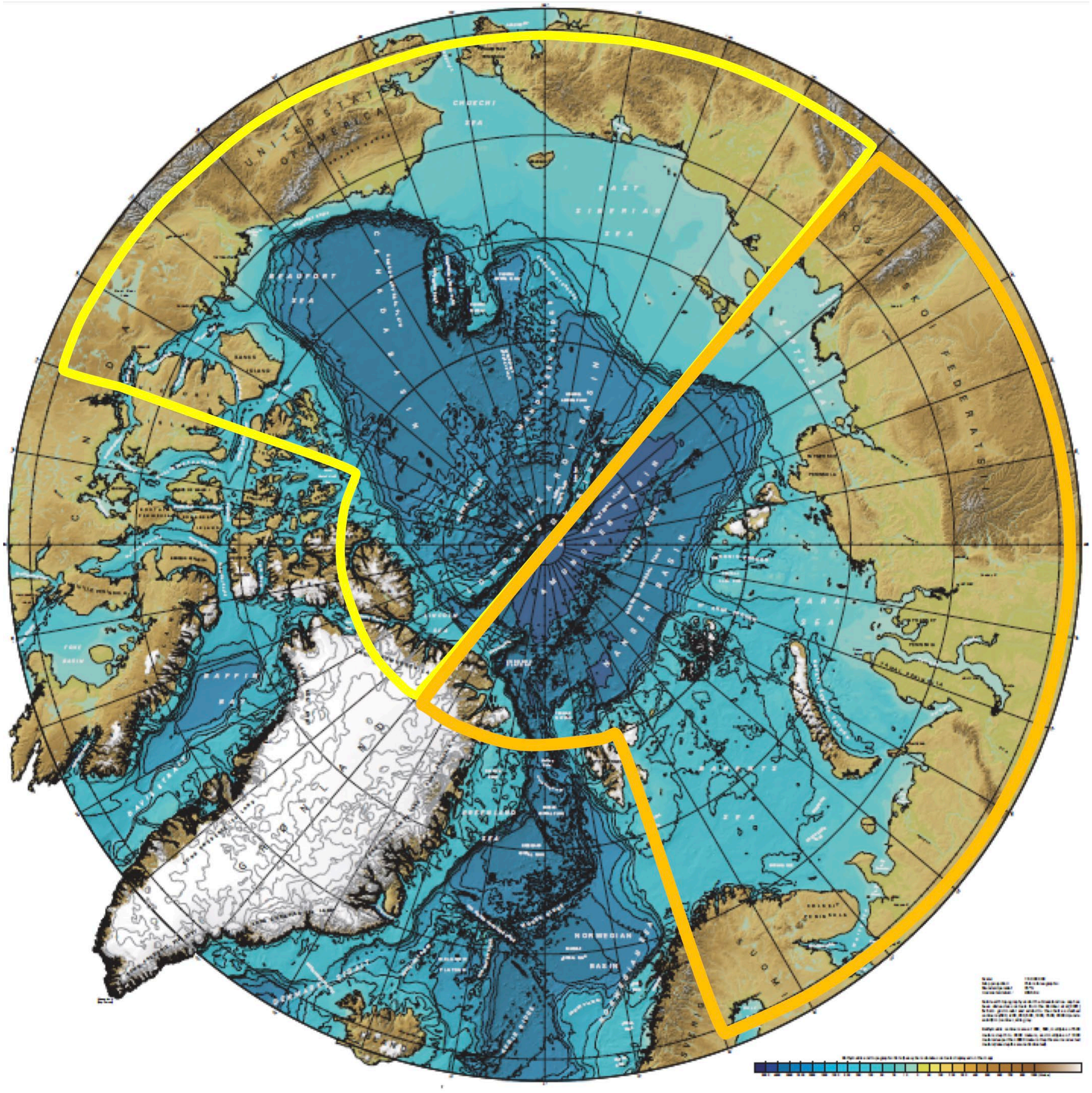

Figure 3-37: The Arctic ocean bathymetry with the Western (yellow) and Eastern (yellow-orange) basins delimited.

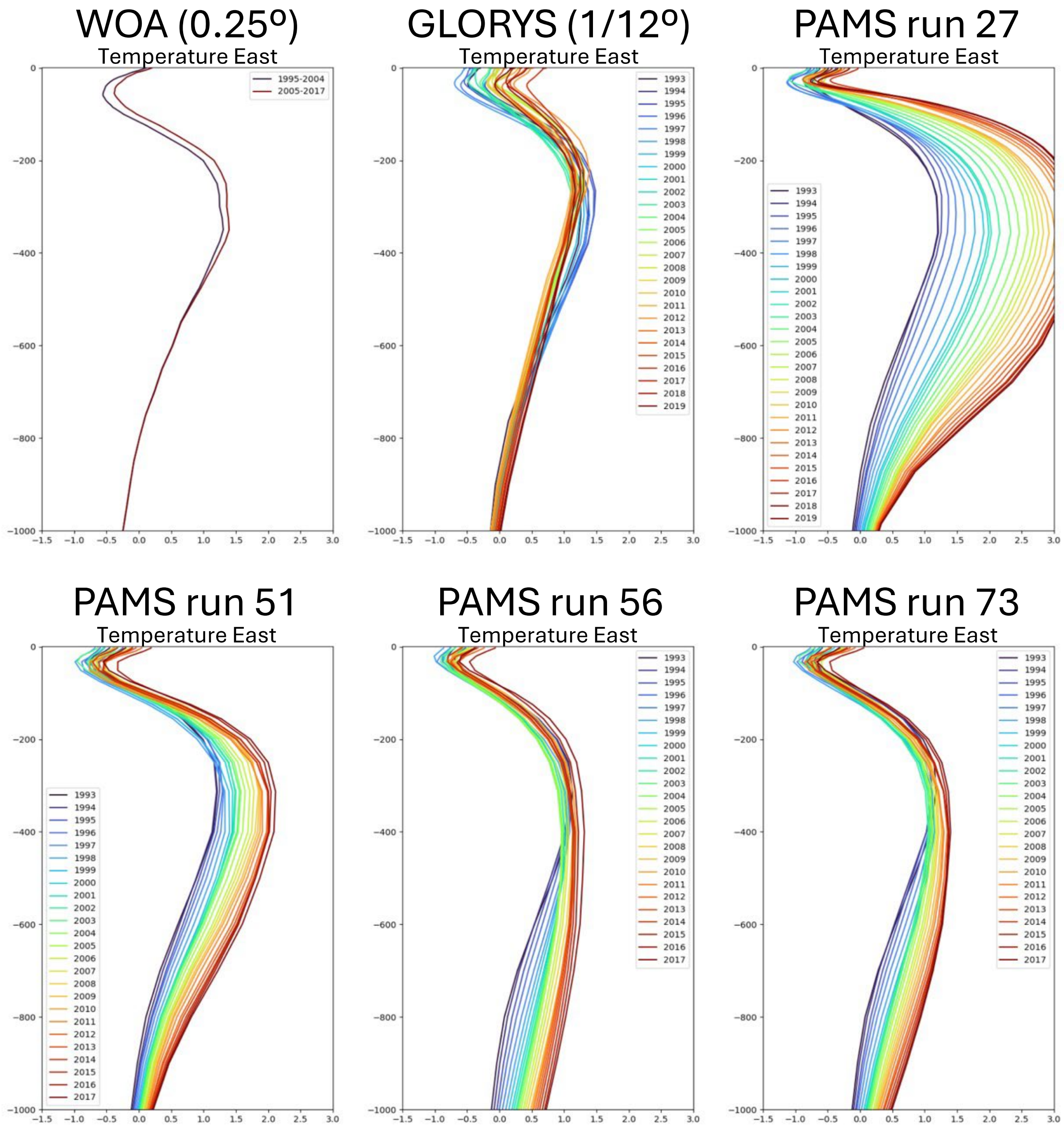

Figure 3-38: Vertical temperature profiles for the eastern Arctic basin by decade for WOA18, and yearly for GLORYS and four PAMS model runs.

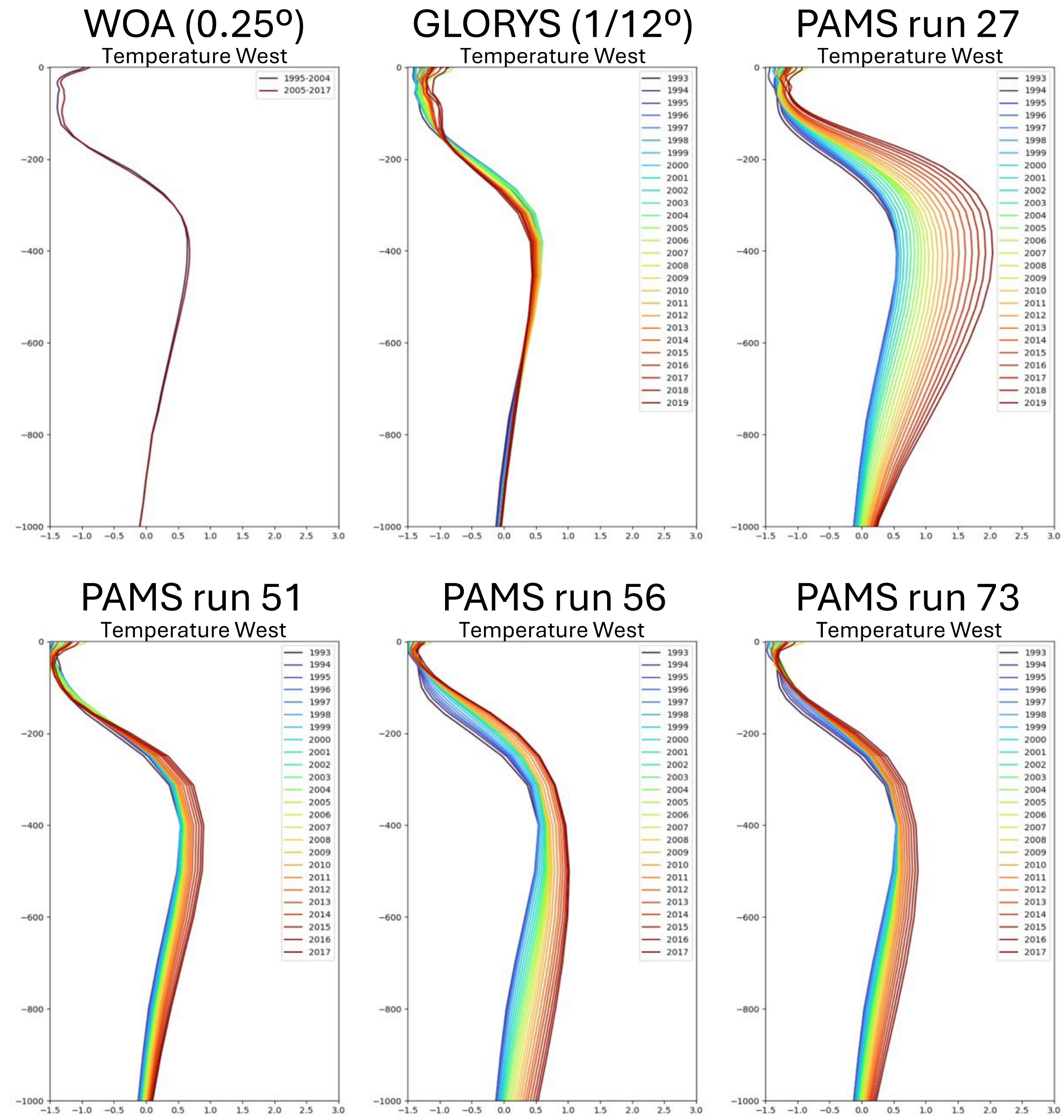

Figure 3-39: Vertical temperature profiles for the western Arctic basin by decade for WOA18, and yearly for GLORYS and four PAMS model runs.

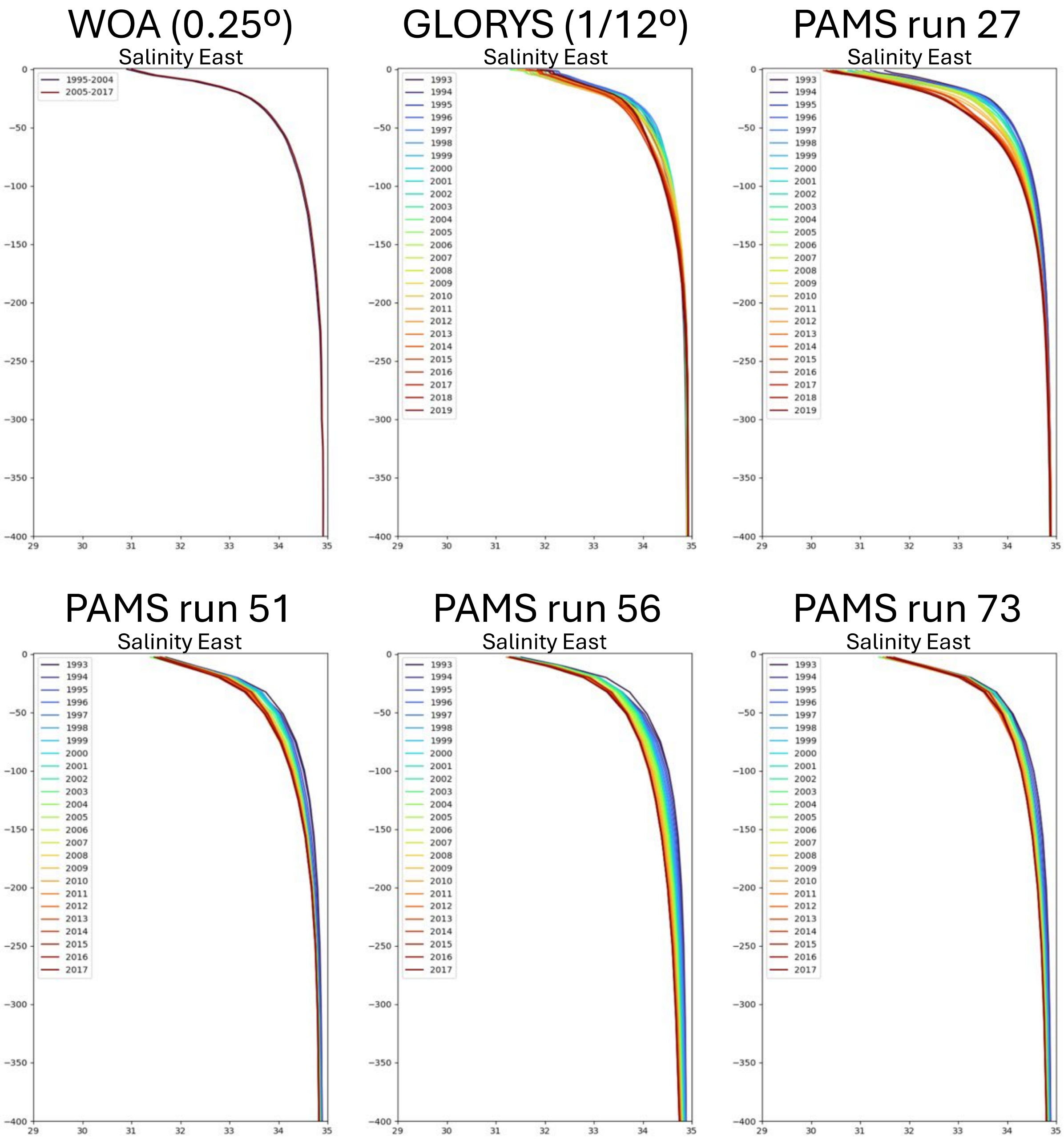

Figure 3-40: Vertical salinity profiles for the eastern Arctic basin by decade for WOA18, and yearly for GLORYS and four PAMS model runs.

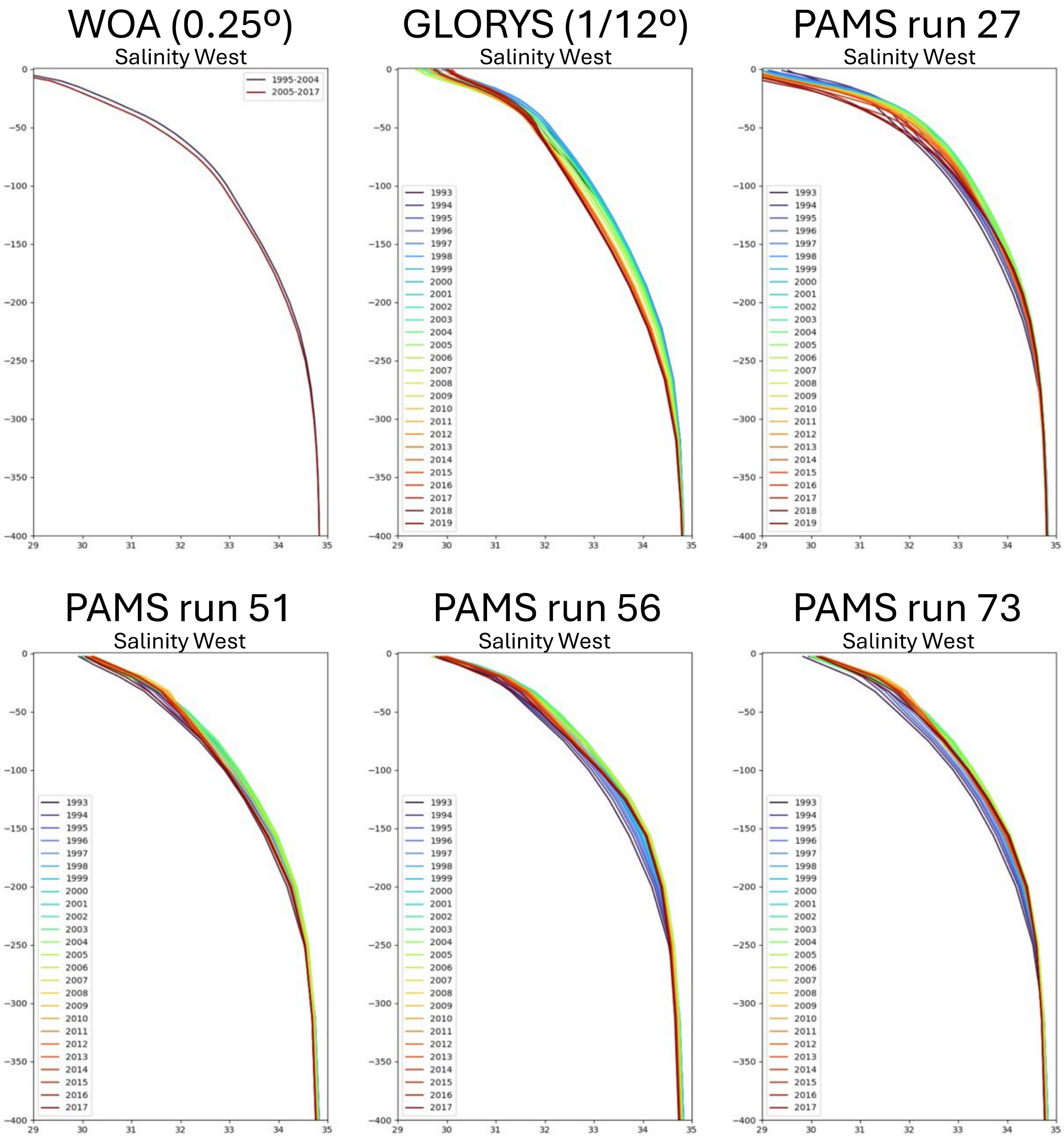

Figure 3-41: Vertical salinity profiles for the western Arctic basin by decade for WOA18, and yearly for GLORYS and four PAMS model runs.

3.5.3 Simulated landfast ice extent

Comparing median landfast ice extents for the month of April for all 25 years of the PAMS model time domain, model run 51 simulates more landfast ice than run 56 (Figure 3-42). However, the modeled extent in both runs is sensitive to the chosen velocity threshold such that Threshold 1 (0.001 cm s^{-1}) in run 51 (Figure 3-42a) produces an extent similar to that of Threshold 2 (0.005 cm s^{-1}) in run 56 (Figure 3-42b). Please refer to Section 2.7.4 for more information about these thresholds.

We also note that the sensitivity to the velocity threshold differs between model runs. In run 51, the difference in median extent between thresholds 2 and 3 is much smaller than the difference between thresholds 1 and 2, suggesting the model is more sensitive below a threshold of 0.005 cm s^{-1}. By comparison, in model run 56, the differences between adjacent thresholds are more equal. Another notable difference in median landfast ice between model runs 51 and 56 is the presence of stationary ice offshore. It does not meet our criteria for being considered landfast since it is not contiguous with the coast, but model run 51 shows a sizeable area of stationary ice in the vicinity of 72 ºN–172 ºW, which is where Hanna Shoal is located (see Figure 1-1). The existence of this feature, isolated from the shoreline, must be a function of the basal shear stress from the parameterized interaction between pressure ridge keels and the shallow seafloor (<20 m) in this location.

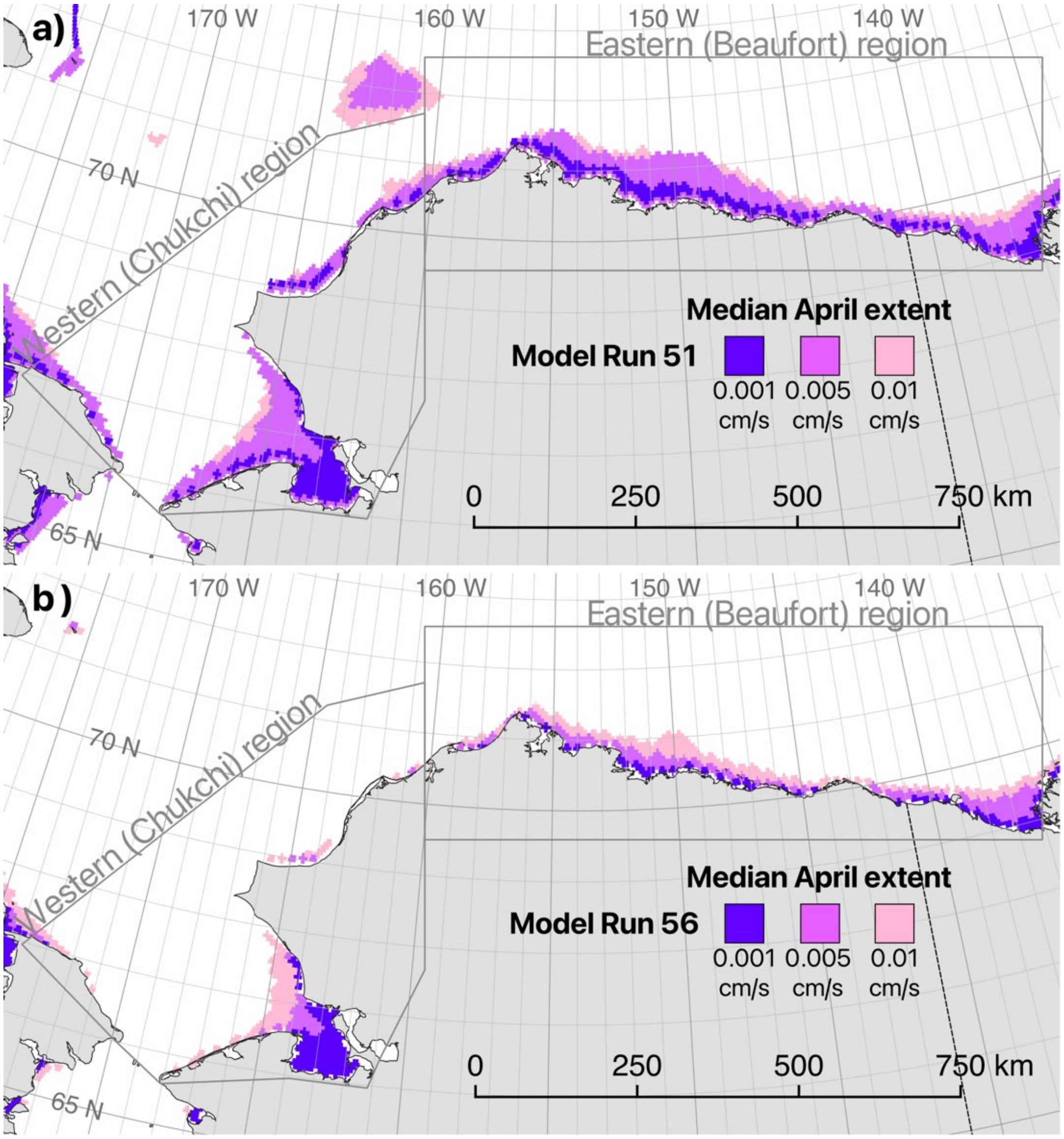

Figure 3-42: 1996 –2017 median April landfast ice extent derived from the PAMS model from a) run 51 and b) run 56. In both model runs, we use three different ice velocity thresholds is listed in Table 2-6.

Although the median extents shown in Figure 3-42 are broadly comparable to those derived from the EM2024 dataset (Figure 3-7), there are a number of occasions where the simulated landfast ice extends well beyond anything in the observed record (Figure 3-43). For velocity threshold 2 (0.005 cm s^{-1}), both model runs indicate that in at least 5% of the days in April between 1993 and 2017, landfast ice formed a bridge across the Bering Strait. Although ice arches are known to form across Bering Strait (e.g., Torgerson and Stringer 1985), it is unusual for them to remain in place for 20 consecutive days. More notable is the more regular formation of a bridge of landfast ice between the Alaska coastline and Hanna Shoal in model run 51, which also occurs in at least 5% of cases. The existence of these landfast bridges is less likely to be related to the basal shear stress parameterization and, instead is more likely to depend on the stiffness, or viscosity of the sea ice.

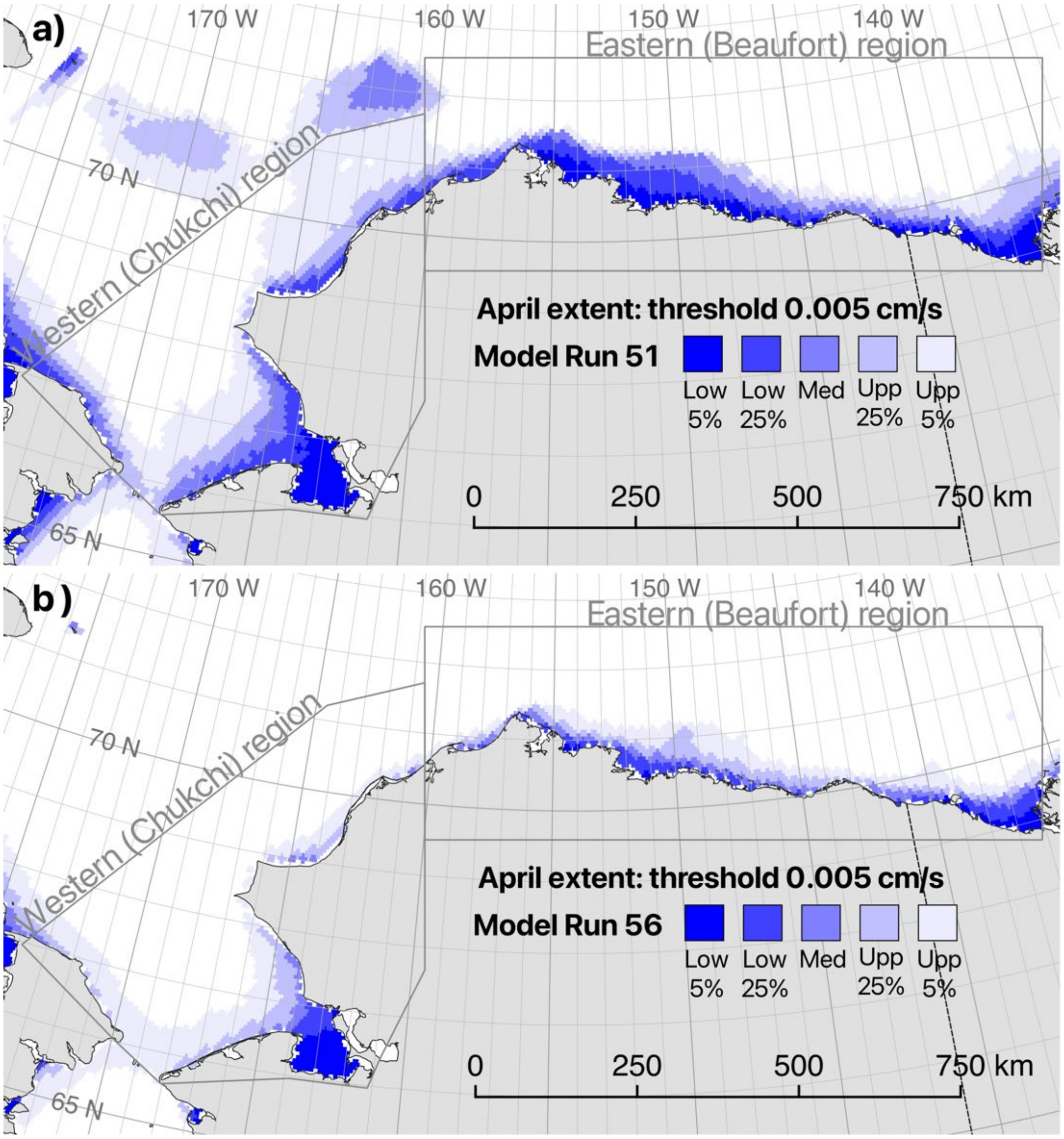

Figure 3-43: Minimum, lower quartile, median, upper quartile, and maximum April landfast ice extents for the period 1996 –2017 derived from the PAMS model from a) run 51 and b) run 56 using a velocity threshold of 0.005 cm s^{-1}.

4 Discussion

4.1 Recent changes in landfast ice in the Alaska Arctic OCS

4.1.1 Changes in landfast ice extent

For the purpose of understanding how the landfast ice regime has changed from 1996–2023 we partitioned the 27-year EM2024 dataset into three 9-year periods (1996–2005; 2005–2014; and 2014–2023) and calculated regional median annual cycles of landfast ice width for each period for the Chukchi and Beaufort regions (Figure 4-1). In all cases, the annual cycle follows a characteristically asymmetric pattern with a gradual advance of the SLIE over winter followed by a rapid retreat, but there are some notable differences between the 9-year periods and between regions.

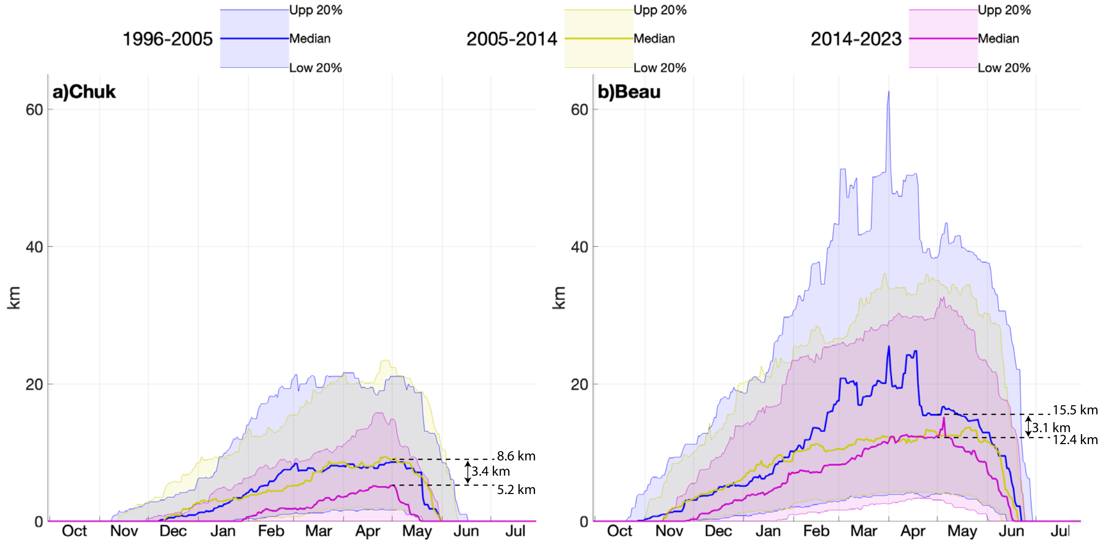

Figure 4-1: Daily median landfast ice width in a) the Chukchi region and b) the Beaufort region computed for the three periods 1996–2005, 2005–2014, and 2014–2023. Shaded regions represent the upper and lower 20th percentile for 1996–2005 and 2014–2023.

Both regions show a marked decline in median landfast ice width from the first period to the last. In the Chukchi region, this retreat of landfast ice appears to take place primarily between the second and third periods, with relatively little difference between the first and second (Figure 4-1a). In contrast, in the Beaufort region, the most substantial change in landfast ice width appears to occur between the first and second 9-year period (Figure 4-1b). Moreover, whereas the Chukchi region exhibits a relatively consistent decrease in landfast ice width in all months, there is a markedly larger change in the Beaufort region between February and April than in other months. It is therefore likely that this pronounced drop in landfast ice width is related to the absence of stable extensions since 2004 (Figure 3-4). These features are discussed in some detail by Mahoney et al., (2014; 2007) and they meet the definition of landfast ice used in the M2014 dataset (Section 2.1.2). However, we believe it is unlikely they would be classified as landfast ice by NIC and ASIP analysts due to their unusually broad extent. We therefore avoid further interpretation of any apparent changes in the landfast ice extent in the Beaufort Sea during these months.

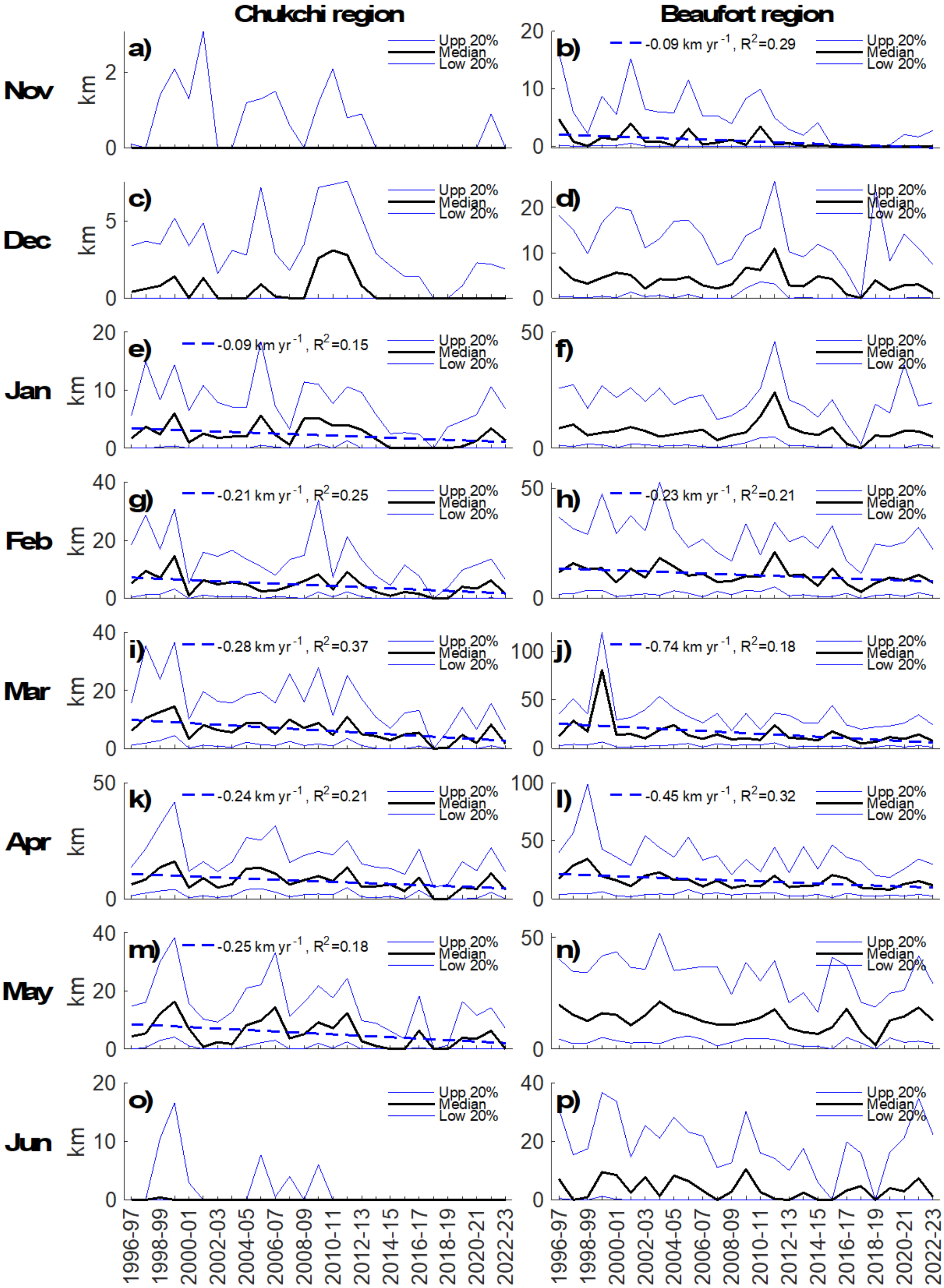

Figure 4-2: Monthly median landfast ice width from 1996–2023 in a) the Chukchi region and b) the Beaufort region.

Landfast ice in the Chukchi region exhibits significant ($p < 0.05$) negative linear trends in width in all months from January to May (Figure 4-2). These trends vary between -0.09 and -0.28 km yr^{-1}, which is consistent with a 3.4 km reduction in end-of-April median landfast ice between the 1996–2005 and 2014–2023 periods (Figure 4-1a). Landfast ice in the Beaufort region also exhibits a similar change in end-of-April median landfast ice width and there are significant negative trends for the months between February and April. However, we omit consideration of trends during these months for the reasons just discussed above. Instead, we note that there is trend of -0.09 km yr^{-1} in November (Figure 4-2b), when the median landfast ice width in the Beaufort region has been zero since 2015. This represents a potentially important transition to a state in which landfast sea ice is more often absent than present. A similar transition appears to have taken place for the month of December in the Chukchi region in 2013 (Figure 4-2c).

4.1.2 Changes in timing of landfast ice season

To evaluate interannual variability in the timing of the landfast sea ice season, we computed regional mean values for each of the 3 key events described in Section 2.2.5 for both the Chukchi and Beaufort regions (Figure 4-3). These results indicate significant linear trends ($p < 0.05$) for all events in the Chukchi region (Figure 4-3a) and in the date of landfast ice formation (first ice) in the Beaufort region (Figure 4-3b). The rates of these trends and their associated R^2 values are given in Table 4-1. With formation getting later by 1.6 d yr^{-1} and ice free conditions occurring 0.8 d yr^{-1} earlier, the average landfast sea ice season in the Chukchi region is getting shorter by around 2.4 d yr^{-1}, amounting to a total shortening of over two months over the 27-year duration of the dataset. In the Beaufort region, the trend toward later formation is weaker than in the Chukchi region (1.1 d yr^{-1}) and we see no significant trends in the timing of breakup or the onset of ice free conditions.

The year-to-year differences in the occurrence dates of key events within each region are considerable and, as a result linear trends describe 34% of the variability, at best (Table 4-1). Notably, formation of landfast ice was anomalously late in the 2017–18 season, with 80% of the coastline reportedly remaining free of landfast ice until March in the Chukchi region (Figure 4-3a) and January in the Beaufort region (Figure 4-3b). Also, breakup was anomalously early in 2018–19, commencing in some areas of the Chukchi region in January and in March in the Beaufort region. If observed trends toward later formation and earlier breakup continue, the likelihood of two such anomalies overlapping in the same season will increase, resulting in an effective absence of landfast ice in such areas.

Table 4-1: Linear regression values for regional mean occurrence dates of key landfast ice events

Region	First ice	Breakup	Ice free
Chukchi	1.6 d yr^{-1}, R^2 = 0.30	-0.6 d yr^{-1}, R^2 = 0.15	-0.8 d yr^{-1}, R^2 = 0.34
Beaufort	1.1 d yr^{-1}, R^2 = 0.21	*No significant trend*	*No significant trend*

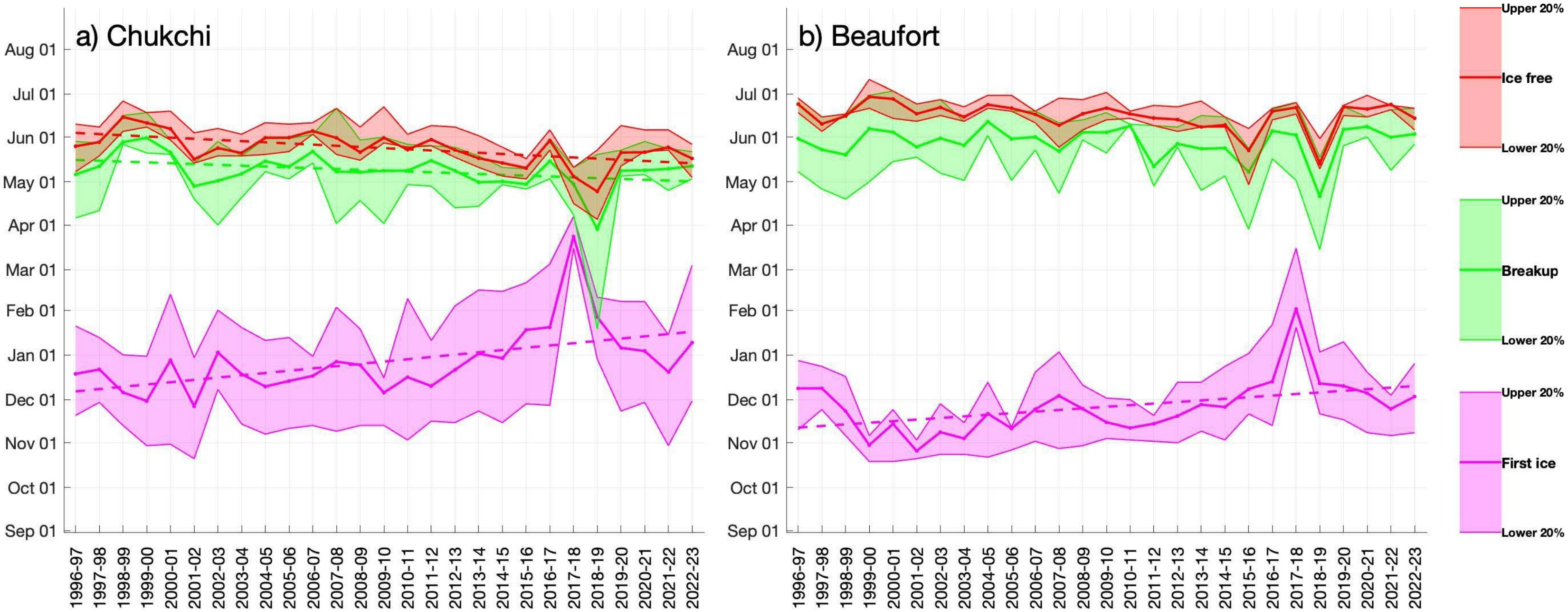

Figure 4-3: Timeseries of mean occurrence date for each key event in the landfast ice cycle over the period of 1996–2023 calculated for a) the Chukchi region and b) the Beaufort region. Dashed lines indicated a statistically significant (P-value < 0.05) trend in the event date.

4.1.3 Evidence of changes in landfast ice breakouts

The catalog of breakout events derived from the EM2024 dataset (Appendix A) shows significant interannual variability and even some evidence of periodicity at timescales of 7–8 years (Figure 3-12). However, there is no indication of a trend or persistent change in the number of breakouts in either region. Moreover, we found that the number of breakout events detected was sensitive to the application of the running minimum that was applied to the interpolated ice chart data products (Section 2.3). Specifically, we found that the number of breakout events cataloged in the ice chart era (i.e., after the 2007–08 season) was approximately 50% higher if the running minimum step was applied after averaging between the NIC- and ASIP-derived data products, instead of being applied to results of each ice chart before averaging as illustrated in Figure 3-12. We believe this sensitivity is caused by the mismatch in the reporting interval of the two charts, which can lead to inconsistent detection of events if a breakout is recorded by charts published on the different days. Applying the 20-day minimum to results from each chart source before averaging results in more consistent counts before and after the 2007–08 season, but due to this sensitivity we avoid making any conclusions about long term changes in breakout frequency. However, we note that 7–8 year fluctuations in breakout count appear robust features of the data such that they were evident even when the running minimum was applied after averaging the NIC and ASIP landfast ice width measurements.

4.2 InSAR detection of landfast ice extent and stability

4.2.1 Suitability of InSAR for routine identification of landfast sea ice

Landfast ice extent is captured well during the middle months of the landfast ice season using InSAR but does not capture any landfast ice at the beginning or end of the season. During the early months of December and January the average the monthly landfast ice width measured by the InSAR based method is slightly less than the average monthly landfast ice width from the EM2024 dataset from 2017–2021 (Figure 3-16a-b). The majority of the difference in the Beaufort region occurs, between Point Barrow and Kaktovik where our InSAR-derived results show the landfast ice is consistently 6–10 km narrower. In the Chukchi region, differences between InSAR-derived width and EM2024 monthly mean width exist in Kotzebue Sound. Similar to the area between Point Barrow and Kaktovik in the Beaufort region, The InSAR-derived width was on average 7.7 km less than the EM2024 width in Kotzebue Sound during January. Early season deviation is caused by thin newly formed ice whose dielectric properties change rapidly, causing the reduction in coherence.

Agreement between InSAR-derived landfast ice extent and the EM2024 dataset is best from February through April. In February and March, our InSAR-based method underestimated landfast ice width compared to the EM2024 dataset by an average of 2.1 km and 1.1 km, respectively for the combined Chukchi and Beaufort regions. In April the InSAR-derived landfast ice width exceeded EM2024 width by an average of 0.7 km across both study regions. The main areas where differences persisted from February through April were Kotzebue Sound and the Colville Delta. Finally, in May, the InSAR based method under measured the landfast ice width consistently across the study region. The consistent under measuring of landfast ice in May is attributed to surface melting causing a loss of coherence between acquisitions. Overall, the InSAR based identification of landfast ice measures the landfast ice width well however the there are certain areas where the 12 days between acquisitions prevent the methods from identifying landfast ice. On this basis, we find that 12-day repeat Sentinel-1 InSAR may be a useful tool for helping discriminate landfast ice sea ice extent during the coldest months of the year when the dielectric properties of the ice surface are most stable. With the imminent launch of the NISAR satellite, 12-day repeat L-band InSAR will be possible for all but the most northern regions of landfast ice in the Arctic. Meyer et al., (2011) showed that L-band coherence could be maintained for 45 days over landfast ice and so we anticipate that NISAR may allow us to extend the useful season of InSAR for this landfast ice detection.

4.2.2 Regional variability and annual evolution of landfast ice stability

In Figure 3-19 we showed how the apparent strain distribution for the whole study area varied month-by-month from December to May. By partitioning this analysis between the Beaufort and Chukchi regions and each of the 11 subregions (see Figure 2-1) we can see landfast ice stability varies around the coastline and over the course of a year. The results of this analysis are shown in Figure 4-4 with shaded regions representing the stability categories based on apparent strain thresholds derived in Section 3.2.3. The mode of the apparent strain distribution decreases monotonically over time in most subregions, achieving the greatest proportion of ice in the stabilized category in April or May. Subregions where the distribution does not decrease throughout the season were subregions 3, 5, and 7. Subregion 3, Outer Kotzebue Sound, did not have any landfast ice present during the month of May. In addition, subregion 3 is dissimilar to the majority of the other subregions. Subregion 3 does not contain much coastline and landfast ice typically ends this region via extending out of Kotzebue Sound rather than found within the region. Subregion 5, Cape Kruzenstern to Point Hope, is the only south facing subregion. While the exact reason the distribution is abnormal is not known, we suspect the small amount of landfast ice in this subregion resulted in the dispersed monthly distributions with poorly define modes. Subregion 7, Cape Lisburne to Wainwright, had the lowest distribution of landfast ice in December. The only landfast ice in this subregion during December occurred within lagoons. The lack of landfast ice outside the lagoon presented an artificially low distribution of apparent strain during December. The modal apparent strain values in the remaining subregions, Chukchi region, Beaufort region, and the entire study region all decreased from December through April or May. Further investigation is needed, but these results indicate landfast ice becomes more stable the longer a pixel is classified as landfast ice. The increase in stability over time could be attributed to the thickening observed by the SIMBs discussed in Section 3.3.

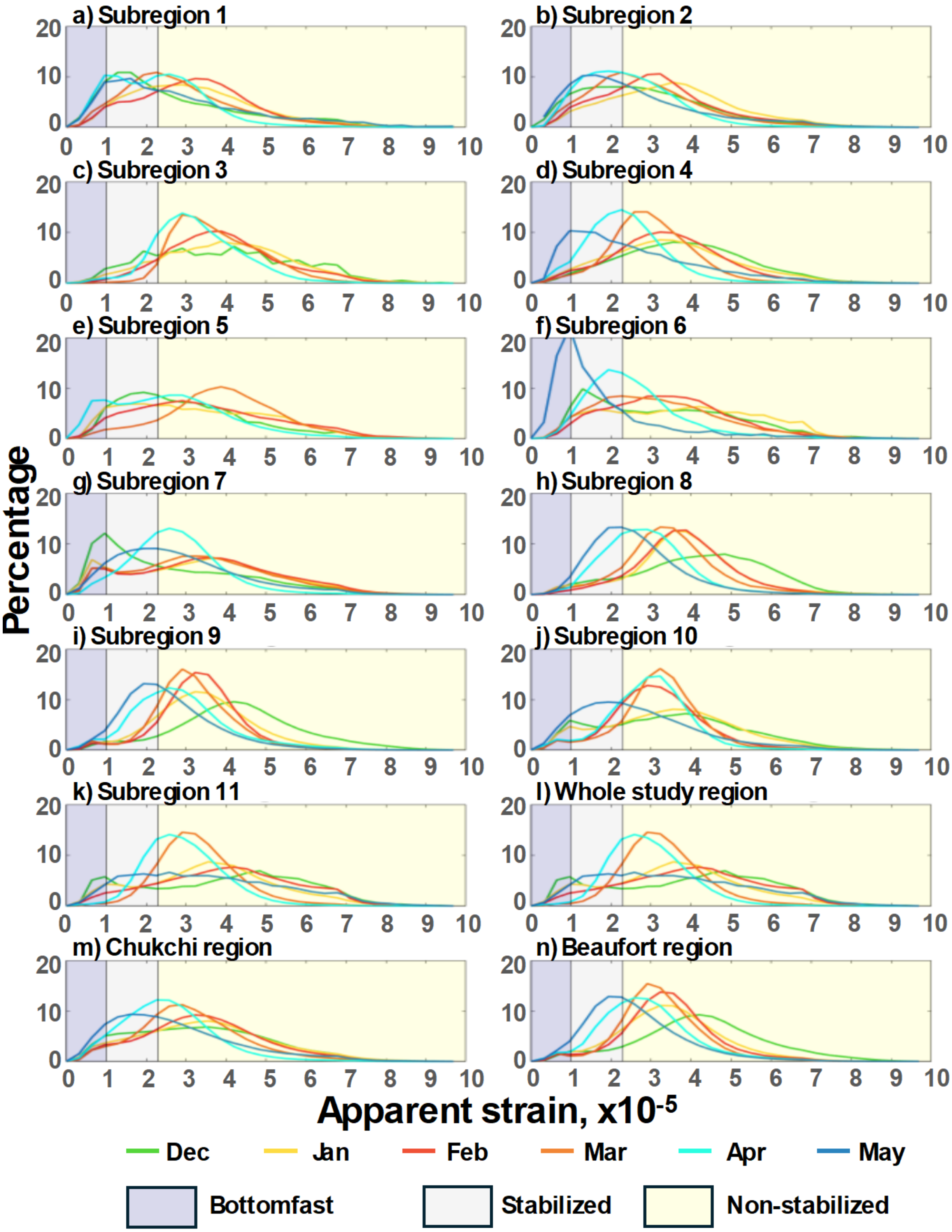

Figure 4-4: Monthly distribution of interferometric phase gradient in each of the 2 regions, 11 subregions, and entire study region. Shaded regions indicated the stability categories discussed in Section 3.2.3.

4.3 In situ observations of landfast ice

Our ability to discuss the oceanographic and thermodynamic processes that drive the breakup of landfast ice is limited by the challenges we faced deploying in-situ instruments in and beneath landfast ice. These challenges included travel restrictions and supply-chain delays during the COVID-19 pandemic as well as damage caused by polar bears, who commonly take an interest in items protruding from the ice. As a result, there is only a short period in early winter of 2022, when we have coincident data from both a SIMB and ADCP. Nonetheless, there are some relevant observations we can make from SIMB and ADCP data that we were able to obtain in Point Hope and Utqiagvik. First, it is clear from the SIMB data from Point Hope in 2020 (Figure 3-22a) and from Utqiagvik in 2024 (Figure 3-24c) that comparatively warm, above-freezing water can make its way under landfast ice even in shallow water and this can pause ice growth or cause bottom melt. However, closer examination of the water temperature before and after breakup of landfast near Point Hope in 2020 (Figure 4-5) suggests that landfast ice in shallow water (i.e., ≲10 m) may be less susceptible to bottom melt than adjacent pack ice. Specifically, the temperature of the water immediately below the ice (red line) started warming around May 22, which may have been related to pooling of fresher meltwater with higher freezing point (Polashenski et al., 2012). However, the water temperature more than 0.5 m below ice (blue line) did not increase substantially until the SIMB began to move (black line). The inset in Figure 4-5 shows a destratification at the moment of detachment (June 8, 08:00 UTC) resulting in a cooling immediately below ice the before the whole water column abruptly warmed. Although we do not know at what point the SIMB was released from its surrounding ice, it is clear that the temperature profile of the water changed abruptly once it ceased to be landfast.

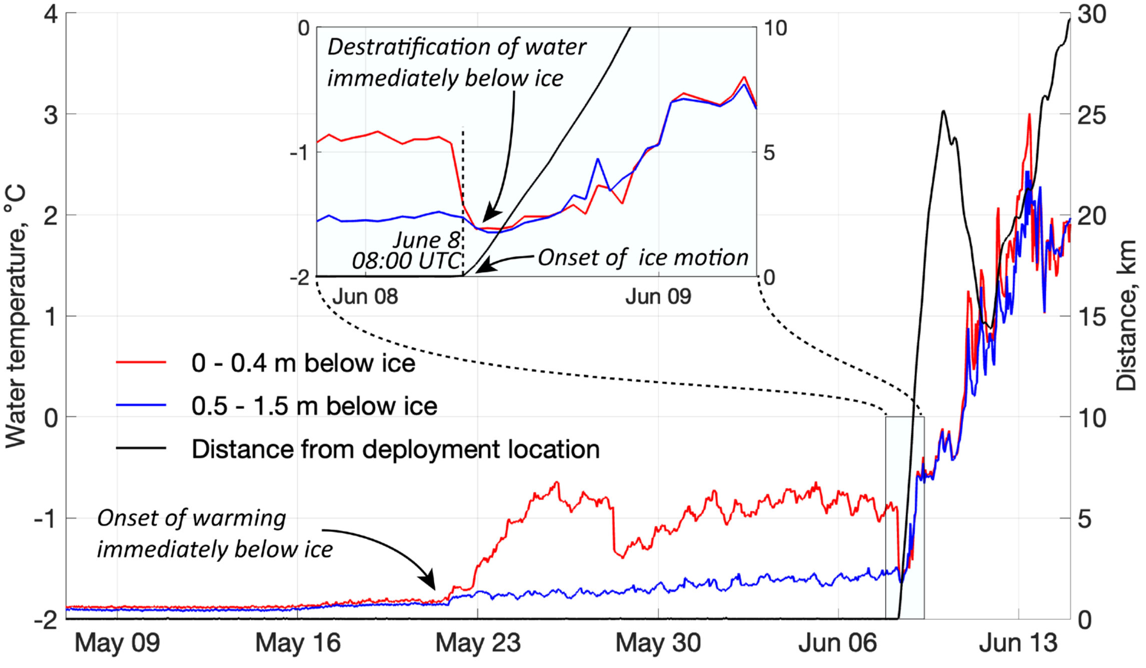

Figure 4-5: Timeseries of water temperature below the ice at different depths and SIMB position in the final 50 days of the data from the SIMB deployed near Point Hope in 2020. The inset shows a 36-hour period starting 12 hours before the detachment.

If the fastness of landfast ice bestows any protection from ocean heat transport, this is likely to depend upon the speed and direction of the currents. The loss of the ADCP deployed alongside the SIMB near Point Hope in 2020 prevents us from knowing what role currents played in either the breakup of landfast ice or the arrival of warm water beforehand. However, the data from the ADCP deployed in similar water depths near Utqiagvik in 2022 (Section 3.3.3) demonstrates that currents below landfast ice can be of sufficient magnitude and persistence to deliver water masses from substantial distances. In particular, the last 4 weeks of ADCP data show consistent northward flow beneath the ice (Figure 3-26h-i). Although the ADCP's temperature sensor does not indicate any pronounced warming and the instrument was recovered before detachment of the landfast ice, it is conceivable that this regime of circulation could effectively introduce warm water from more southerly latitudes to promote bottom melting like observed at Point Hope.

4.4 Impact of storms on landfast ice extent

The results showed that winds and storms account for many, but not all, landfast breakout events along the Beaufort and Chukchi Sea coasts. While the composite analysis showed the signal of Bering Sea storms being associated with these events, the statistical significance was limited in geographic extent. A daily synoptic map typing analysis of sea level pressure using SOM revealed that storms in the southern Bering Sea is the most common pattern associated with these events. This pattern leads to enhanced easterly winds along the northern coasts of Alaska. However, no type of SOM pattern clearly dominated the results. The patterns shown in Figure 3-28 and the Node 19 SOM results (Figure 3-29) suggest that remote wind forcing in the southeast Bering Sea may be a key component of some landfast ice breakout events. Together, these analyses are consistent with the suggestions of Danielson et al., (2020b; 2014) that continental shelf waves triggered by storms in the Bering Sea could be the driving mechanism, although these patterns also show local winds that could also contribute to landfast ice breakout events.

The findings of our analysis share key similarities with existing literature on atmospheric forcing of landfast breakout events in Alaska. Jones et al., (2016) noted enhanced wind stress occurred prior to two breakout case studies in 2009 and 2010 at Utqiagvik but with differences in wind direction. However, the 2010 case had easterly winds consistent with main SOM node noted in our results for the Beaufort Sea. Bogardus et al., (2020) found that strong southerly winds played an important role in a breakout event near Kotzebue in December 2016 in the Chukchi Sea. Southerly wind conditions were also noted to be important for some breakout events at St. Lawrence Island in northern Bering Sea as well (Jensen et al., 2023). Based on our SOM analysis these wind directions would typically fall under Nodes 1–2, which occurred more rarely in conjunction with the breakout events in the database. However, Nodes 1–2 occurred more frequently for the Chukchi than the Beaufort region.

4.5 Comparison between simulated and observed landfast sea ice extent

By reprojecting and rescaling the 12-km PAMS gridded landfast ice fields into the grid used for the EM2024 dataset, we were able to apply the SLIEalyzer tools (Section 2.2) to make directly comparable measurements of landfast width and related metrics for the period 1996–2017 when the model output overlap temporally with the EM2024 dataset. A comparison of the regional mean daily landfast ice width (Figure 4-6) shows that the model tends to underestimate the median landfast ice width in most months, resulting in a substantial underestimation in the duration of the landfast ice season. In the Chukchi region as a whole, the median daily landfast ice width remains zero throughout the year in all simulations except model run 51 for thresholds 1 and 2, when it is non-zero from early March to mid-May. In the Beaufort Region, all simulations achieve a non-zero median daily landfast ice width at some point during the year, but for a substantially shorter duration than shown by the EM2024 data.

Overall, the simulated landfast ice widths are in closest agreement with observations during April, when the curves of median landfast ice width from the PAMS model results often intersect with those derived from the observations in the EM2024 dataset. In months prior to April, landfast ice is consistently underestimated while May is the only month when there is a substantial overestimate in landfast ice width. This reflects another notable aspect of the model results, which is that the annual maximum extent of landfast ice in the Beaufort Region occurs consistently later than observed. This result is somewhat surprising and possibly indicates the model lacks a way represent processes associate with destabilization of landfast ice, such as thermal degradation of grounded ridge keels reducing the amount of basal shear stress they can exert on the ice. Discharge of terrestrial meltwater is another process strongly associated with breakup of landfast ice (e.g., Bareiss et al., 1999), which maybe underrepresented by the PAMS model due to the lack of reporting point data included in the GloFAS forcing data (Section 2.7.2).

Finally, when the PAMS model shows landfast ice is present, it tends to overestimate its extent. This results in the substantially greater variance in the model results, compared with the observations. The width of the shaded areas in Figure 4-6 represents both spatial and temporal variability. The overestimation of spatial variability in landfast ice extent results from a tendency to consistently overestimate landfast ice in some areas while underestimating in others, as illustrated for the month of April in Figures 3-42 and 3-43. At the same time, inspection of results from individual years shows considerable short-term variability where the landfast ice appears to completely breakout and reform multiple times in a single season. This type of behavior suggests that much of what is being identified as landfast ice is not actually securely anchored and may only exhibit sub-threshold velocity during periods of low wind and current. However, the exclusion of such ice is the principal reason we adopt a 20-day duration in our definition of landfast ice (Section 2.1.2). An alternative explanation might therefore be that the basal shear stress is varying over time, perhaps due to sensitivity in the mean thickness or thickness distribution within a grid cell. In reality, the thickness distribution of landfast ice should only evolve slowly through thermodynamic processes, but the non-zero velocity of the simulated ice may lead to internal deformation that should require some change to the thickness distribution.

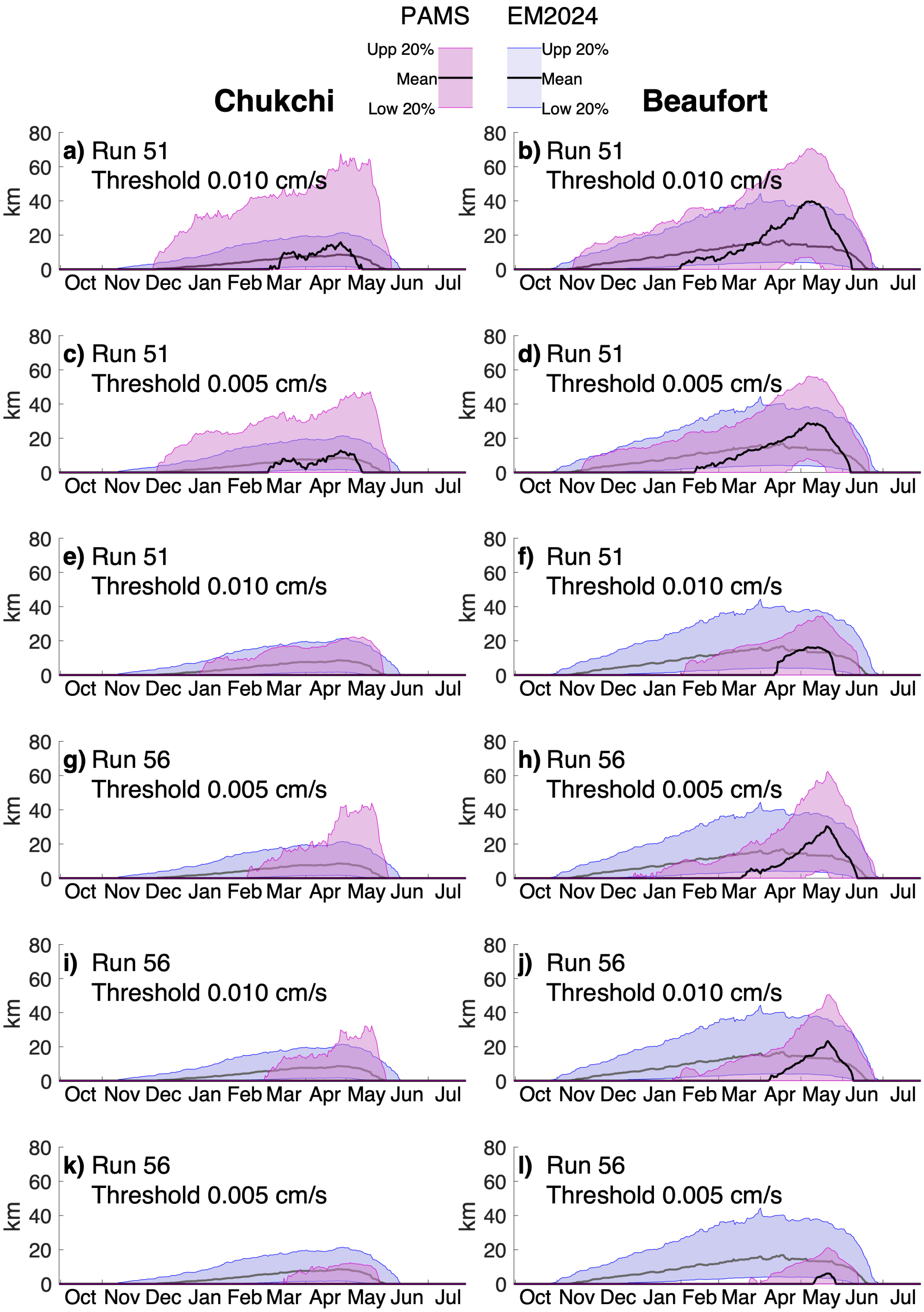

Figure 4-6: Regional mean landfast ice width from the PAMS model for (a-f) runs 51 and (g-i) runs 56 with the three velocity thresholds described in Section 2.7.4. Lefthand panels (a,c,e,g,i,k) show results for the Chukchi Region, while righthand panels (b,d,f,h,j,l) show results for the Beaufort Region.

5 Conclusions

5.1 Lessons from an updated climatology of landfast sea ice in the Arctic OCS

By extending the prior work of Mahoney et al., (2014), we have developed a 27-year climatology of daily landfast ice width in the Alaska Arctic OCS, spanning the Chukchi and Beaufort Seas. These data show that the duration and extent of landfast ice is declining throughout the region. During the 9-year period from 1996–2005, the median landfast ice extent in April occupied 3.8% of the area of the U.S. Arctic OCS, whereas for the period 2014–2023 this percentage had reduced to 2.1%, representing a total decrease by 9,950 km^2. However, we remind the reader that our study area extends outside the Arctic OCS (Figure 1-2) and so these numbers exclude landfast within 3 nautical miles of the coast or adjacent to the Russian and Canadian coastlines.

The changes in landfast ice appear most pronounced in the Chukchi Sea, where landfast sea ice is forming later and breakup earlier (Figure 4-3) and shows a significant decrease in extent during every month in between January and May (Figure 4-2). In the Beaufort Sea, there is a significant trend toward later formation (Figure 4-3b) and negative trend in region-wide median landfast ice width in the month of November. However, there is no evidence of a trend in the dates of breakup and ice-free conditions in the Beaufort Sea and we have reason to be cautious about interpreting negative trends in landfast ice width during the months of January–March due to possible discrepancies in the treatment of stable extensions between the M2014 dataset and the later NIC and ASIP ice chart-derived results.

Comparing landfast ice width measurements during the 2007–08 landfast ice season, when data from M2014, NIC, and ASIP datasets are available, we find good overall agreement in the timing of formation and breakup between all three parent data sources (Figure 3-1). In the Beaufort region, there is good agreement in landfast ice width between the M2014 and NIC datasets throughout the season, though in the Chukchi region year the NIC data underestimates the maximum annual width compared with the M2014 dataset. The ASIP datasets shows greater landfast ice width than either of the other two datasets in both the Chukchi and Beaufort regions, though this discrepancy is related to a few specific polygons in individual ice charts. For the remainder of the EM2024 period, we find no consistent bias between the NIC and ASIP datasets and we believe that an average of both data sources, when available, is likely to provide more consistent data for a climatology than data from a single chart-based source, since it will be less sensitive to missing or misidentified polygons. However, the existence of such irregularities in the ice charts highlights the value of a more consistent approach such as that used in the production of the M2014 dataset.

5.2 Application of InSAR for landfast ice mapping

Although prior work by Meyer et al., (2011) demonstrated the potential for using interferometric coherence as a means of automating landfast ice detection, our evaluation of Sentinel-1 InSAR products suggests that this is only likely to be practicable with currently available C-band SAR data during the coldest months of the year, when the landfast ice and its dielectric properties are most stable. The longer wavelength of L-band SAR is expected to be less sensitive to dielectric changes that take place during the earlier and later stages of the landfast ice, and we therefore anticipate this topic will be worth revisiting after the launch of the National Aeronautics and Space Administration (NASA)-Indian Space Research Organisation (ISRO) synthetic aperture radar (NISAR) satellite, which is expected later in 2024. Nonetheless, our quantitative analysis of phase gradients within landfast ice shows that we can use InSAR to classify the stability of landfast ice. Comparison between the location of SLIE nodes (Figure3-5) and the InSAR-derived extent of stabilized ice (Figure 3-21) demonstrates InSAR may be useful for identifying the location of grounded ridges. Moreover, our results show that landfast ice tends to become more stable the longer it remains in place. This suggests that a later onset of landfast ice formation, may contribute to a reduced stability and greater susceptibility to breakout.

5.3 Impact of the ocean on landfast ice mass balance and stability

Although our program of in-situ observations was curtailed by the COVID-19 pandemic, we obtained some valuable data on the sub-ice temperature profile immediately before and after detachment of landfast sea ice near Point Hope. The abrupt warming of water below the ice within hours of breakup suggests that the ice was buffered from the associated heat flux while it was landfast and that the mass balance of landfast ice may be markedly different from that of adjacent pack ice once sea surface temperatures rise above the freezing point. Had the SIMB deployed in February 2024 (Table 2-3) not been damaged by a polar bear in early May, we had been planning to leave it in place to obtain more data during breakup and transition to mobile pack ice. Nonetheless, more such SIMB deployments could provide valuable insights into the interrelation between ocean heat and landfast ice detachment. Ocean current data would also add significant value to such deployments, but ADCPs are unlikely to be suitable in this application. Instead, a less expensive instrument with satellite telemetry capabilities would be preferable.

5.4 Forecastability of breakout events

We find no evidence of long-term change in the occurrence of breakouts, though there is substantial interannual variability and possible evidence of sub-decadal periodicity in the frequency of such events (Figure 3-12). We also found that some regions are more prone to breakout than others (Figure 3-14) and a visual comparison suggests these regions may exhibit higher average interferometric phase gradients (Figure 3-17 and Figure 3-18). However, we found no evidence that the phase gradient in individual 12-day interferograms can be used to predict breakout events. However, analysis of ERA-5 SLP data suggests that breakout events are commonly associated with anomalously low pressure in the southern Bering Sea (Figure 3-28) related to storms in this region (Figure 3-29 and Figure 3-30). Together, these results suggest that storm predictions might be combined with the spatial distribution of breakout frequency to provide warnings of increased likelihood of landfast ice breakout.

5.5 Numerical simulation of landfast ice in the Arctic OCS

As of July 2024, we have completed numerous different runs of the PAMS coupled ice-ocean model and have analyzed landfast ice extent in two of these that reproduced acceptable results in terms of total ice concentration and temperature and salinity at depth. Although these results cannot be described as realistic simulations of landfast ice behavior, they provide valuable insights for ongoing model development. For example, each simulation achieves a characteristic annual of landfast ice extent with a gradual advance and rapid retreat (Figure 4-6), but in comparison with the EM2024 dataset, the modeled landfast ice season is consistently too short, and the short-term and regional variance is too great. In both model runs the timing of maximum landfast ice extent also occurs notably later than observed, particularly in the Beaufort Sea. This may suggest the basal shear stress parameterization fails to capture a seasonal process that reduces the coupling with the seafloor, such as preferential melting of ridge keels (e.g., Salganik et al., 2023). We also note that model run 56 produces considerably less landfast in the Arctic OCS than model run 51, which we attribute to the use of a new, experimental coupled ice-ocean driver (CIOD) in run 56 (see Section 2.7.5). A closer inspection of run 56 shows that the CIOD is driving some noise in the surface ocean velocity fields, which likely generates greater variance in the ice velocity field, thereby reducing the extent of ice that meets the 20-day criteria for being landfast.

The differences between the simulation and the EM2024 dataset notwithstanding, our results represent a useful testbed for further PAMS model development. Not only is the EM2024 dataset a benchmark against which we can assess model performance, the study region contains geographic features that should facilitate diagnosis of model behavior. For example, the occurrence of stationary ice over shallow features such as Hanna Shoal (Figures 3-42 and 3-43) allows us to assess the effects of changes to the basal shear stress parameterization (Section 2.7.3) largely independently from other model parameters. A realistic simulation in agreement with observations (i.e., Mahoney et al., 2012) would reproduce basal shear stress in a local area on top of the shoal without creating a large area of surrounding stationary ice. Conversely, the model should be able to reproduce short-lived regions of stationary ice across features like Bering Strait in accordance with observed ice-arching behavior (Torgerson and Stringer 1985), without creating persistent ice bridges spanning the southern Chukchi Sea.

5.6 Recommendation for future studies

5.6.1 Development of Pan-Arctic landfast ice dataset

Here we have demonstrated the feasibility of using existing ice charts to develop a climatology of landfast sea ice extent. We recommend extending this approach to provide pan-Arctic coverage using all available ice chart data. For example, the Canadian Ice Service, the Danish Meteorological Institute, Finnish Meteorological Institute, and Russia's Arctic and Antarctic Research Institute all routinely produce digital vector ice charts that identify the extent of landfast ice. With the definition of a new set of pan-Arctic coast vectors (segregated into as many subregions as necessary), it would be relatively straightforward to apply the SLIEalyzer to replicate our analysis to the whole Arctic.

5.6.2 Targeted post-detachment in-situ observations

The SIMB data from the Point Hope provides valuable insight into the mass balance of sea ice before and after detachment from the coast. Once the ice ceased to be landfast, it appears that it was exposed to a substantially warmer ocean. This raises the possibility that detachment of the ice allowed the incursion of warm water into the region formerly occupied by landfast ice. Additionally, it has been speculated that since landfast ice commonly persists after the retreat of pack ice from a region, it may serve as valuable habitat for walrus after it detaches (Mahoney 2018). We therefore recommend continued deployments of SIMBs with the goal of letting them detach with the ice to obtain valuable mass balance data from this under-observed period of the landfast and post-landfast ice season.

5.6.3 Application of NISAR data to landfast ice

The expected 2024 launch of NASA and ISRO's NISAR satellite should provide further opportunities for the application InSAR techniques to the study of landfast ice. The 12-day repeat interval will the same as that of the Sentinel-1 data we have used here, but there is reason to expect the data from NISAR's L-band radar will be less susceptible to decorrelation during the melt season. Once NISAR data become available, we therefore recommend an immediate assessment of its value for automated detection of landfast ice extent or categorization of stability through calculation of apparent strain.

5.6.4 Continued development and evaluation of simulated landfast ice in PAMS model

Development of the PAMS model is anticipated to continue and, as discussed in Section 5.5, the EM2024 dataset represents ideal product against which to validate its simulation of landfast ice. In conjunction with our recommendation described in Section 5.6.1, we therefore recommend continued assessment of simulated landfast ice extent, with particular attention paid to the timing of formation and breakup, the characteristics of short term variability in the location of the SLIE, and the potential for unrealistic ice bridges to form across channels and straights, or even between the coastline and shallow water regions offshore like Hanna Shoal.

6 References

Adcroft A. 2013. Representation of topography by porous barriers and objective interpolation of topographic data. Ocean Modelling. 67:13-27 doi: https://doi.org/10.1016/j.ocemod.2013.03.002.

Adcroft A, Anderson W, Balaji V, Blanton C, Bushuk M, Dufour CO, Dunne JP, Griffies SM, Hallberg R, Harrison MJ, Held IM, Jansen MF, John JG, Krasting JP, Langenhorst AR, Legg S, Liang Z, McHugh C, Radhakrishnan A, Reichl BG, Rosati T, Samuels BL, Shao A, Stouffer R, Winton M, Wittenberg AT, Xiang B, Zadeh N, Zhang R. 2019. The GFDL Global Ocean and Sea Ice Model OM4.0: Model Description and Simulation Features. Journal of Advances in Modeling Earth Systems. 11(10):3167-3211 doi: 10.1029/2019ms001726.

Alaska Sea Ice Program (ASIP). 2023. NWS Daily Sea Ice Concentration Analysis. Alaska Ocean Observing System (AOOS). https://portal.aoos.org/?ls=CGOnN2L_#metadata/f55d3d00-aa4e-11e3-8992-00219bfe5678/a5b58402-a9c1-11e3-a3fe-00219bfe5678[accessed 2023]

Avila-Diaz A, Bromwich DH, Wilson AB, Justino F, Wang S-H. 2021. Climate Extremes across the North American Arctic in Modern Reanalyses. Journal of Climate. 34(7):2385-2410 doi: https://doi.org/10.1175/JCLI-D-20-0093.1.

Bachand CL, Walsh JE. 2022. Extreme Precipitation Events in Alaska: Historical Trends and Projected Changes. Atmosphere.13(3)doi:10.3390/atmos13030388.

Bareiss J, Eicken H, Helbig A, Martin T. 1999. Impact of river discharge and regional climatology on the decay of sea ice in the Laptev Sea during spring and early summer. Arctic Antarctic and Alpine Research. 31(3):214-229 doi,

Bodner A, Balwada D, Zanna L. 2023. A Data-Driven Approach for Parameterizing Submesoscale Vertical Buoyancy Fluxes in the Ocean Mixed Layer. arXiv preprint arXiv:231206972. doi:

Bogardus R, Maio C, Mason O, Buzard R, Mahoney A, de Wit C. 2020. Mid-Winter Breakout of Landfast Sea Ice and Major Storm Leads to Significant Ice Push Event Along Chukchi Sea Coastline. Frontiers in Earth Science. 8 doi, https://www.frontiersin.org/articles/10.3389/feart.2020.00344

Bouillon S, Morales Maqueda MÁ, Legat V, Fichefet T. 2009. An elastic–viscous–plastic sea ice model formulated on Arakawa B and C grids. Ocean Modelling. 27(3):174-184 doi: https://doi.org/10.1016/j.ocemod.2009.01.004.

Cassano EN, Cassano JJ. 2010. Synoptic forcing of precipitation in the Mackenzie and Yukon River basins. International Journal of Climatology. 30(5):658-674 doi: https://doi.org/10.1002/joc.1926.

Cassano EN, Cassano JJ, Seefeldt MW, Gutowski Jr WJ, Glisan JM. 2017. Synoptic conditions during summertime temperature extremes in Alaska. International Journal of Climatology. 37(9):3694-3713 doi: https://doi.org/10.1002/joc.4949.

Copernicus Marine Service Information. 2023. Global Ocean Physics Reanalysis (GLORYS12v1). https://doi.org/10.48670/moi-00021. [accessed 2023/01/01]

Curchitser EN, Hedstrom K, Danielson S, Kasper JL. 2018. Development of a Very High-Resolution Regional Circulation Model of Beaufort Sea Nearshore Areas. (University of Alaska Fairbanks) U.S. Dept. of the Interior, Bureau of Ocean Energy Management, Alaska OCS Region, Anchorage, AK., OCS Study BOEM 2018-018. https://espis.boem.gov/final%20reports/BOEM_2018-018.pdf

Dammann DO, Eicken H, Mahoney AR, Meyer FJ, Freymueller JT, Kaufman AM. 2018. Evaluating landfast sea ice stress and fracture in support of operations on sea ice using SAR interferometry. Cold Regions Science and Technology. 149:51-64 doi: https://doi.org/10.1016/j.coldregions.2018.02.001.

Dammann DO, Eriksson LEB, Mahoney AR, Eicken H, Meyer FJ. 2019. Mapping pan-Arctic landfast sea ice stability using Sentinel-1 interferometry. The Cryosphere. 13(2):557-577 doi: 10.5194/tc-13-557-2019.

Danielson S. 2013. Alaska Region Digital Elevation Model version 2.0. University of Alaska Fairbanks, Fairbanks, Alaska., http://research.cfos.uaf.edu/bathy/[accessed January 1, 2022]

Danielson SL, Ahkinga O, Ashjian C, Basyuk E, Cooper LW, Eisner L, Farley E, Iken KB, Grebmeier JM, Juranek L, Khen G, Jayne SR, Kikuchi T, Ladd C, Lu K, McCabe RM, Moore GWK, Nishino S, Ozenna F, Pickart RS, Polyakov I, Stabeno PJ, Thoman R, Williams WJ, Wood K, Weingartner TJ. 2020a. Manifestation and consequences of warming and altered heat fluxes over the Bering and Chukchi Sea continental shelves. Deep Sea Research Part II: Topical Studies in Oceanography. 177:104781 doi: https://doi.org/10.1016/j.dsr2.2020.104781.

Danielson SL, Dobbins EL, Jakobsson M, Johnson MA, Weingartner TJ, Williams WJ, Zarayskaya Y. 2015. Sounding the northern seas. Eos. 96 doi: doi:10.1029/2015EO040975.

Danielson SL, Hedstrom KS, Weingartner TJ. 2016. Bering-Chukchi circulation pathways, North Pacific Research Board 2016 Final Report, NPRB project #1308. (University of Alaska Fairbanks) Fairbanks, AK.

Danielson SL, Hennon TD, Hedstrom KS, Pnyushkov AV, Polyakov IV, Carmack E, Filchuk K, Janout M, Makhotin M, Williams WJ, Padman L. 2020b. Oceanic Routing of Wind-Sourced Energy Along the Arctic Continental Shelves. Frontiers in Marine Science. 7(509) doi: 10.3389/fmars.2020.00509.

Danielson SL, Weingartner TJ, Hedstrom KS, Aagaard K, Woodgate R, Curchitser E, Stabeno PJ. 2014. Coupled wind-forced controls of the Bering–Chukchi shelf circulation and the Bering Strait throughflow: Ekman transport, continental shelf waves, and variations of the Pacific–Arctic sea surface height gradient. Progress in Oceanography. 125:40-61 doi: https://doi.org/10.1016/j.pocean.2014.04.006.

de Boyer Montégut C, Madec G, Fischer AS, Lazar A, Iudicone D. 2004. Mixed layer depth over the global ocean: An examination of profile data and a profile-based climatology. Journal of Geophysical Research: Oceans. 109(C12) doi: https://doi.org/10.1029/2004JC002378.

Dmitrenko IA, Tyshko KN, Churun VN, Hoelemann JA, Eicken H, Kassens H, Kirillov SA. 2005. Impact of flaw polynyas on the hydrography of the Laptev Sea. Global and Planetary Change. 48:9-27 doi,

Dupont F, Dumont D, Lemieux JF, Dumas-Lefebvre E, Caya A. 2022. A probabilistic seabed–ice keel interaction model. The Cryosphere. 16(5):1963-1977 doi: 10.5194/tc-16-1963-2022.

Egbert GD, Erofeeva SY. 2002. Efficient Inverse Modeling of Barotropic Ocean Tides. Journal of Atmospheric and Oceanic Technology. 19(2):183-204 doi: https://doi.org/10.1175/1520-0426(2002)019<0183:EIMOBO>2.0.CO;2.

Eicken H, Gradinger R, Graves A, Mahoney A, Rigor I, Melling H. 2005. Sediment transport by sea ice in the Chukchi and Beaufort Seas: Increasing importance due to changing ice conditions? Deep-Sea Res II. 52:3281-3302 doi,

Eicken H, Shapiro L, Gaylord A, Mahoney A, Cotter P. 2006. Mapping and characterization of recurring spring leads and landfast ice in the Beaufort and Chukchi Seas. (Geophysical Institute, University of Alaska Fairbanks) U.S. Department of the Interior, Minerals Management Service, Alaska OCS Region Final Report, OCS Study MMS 2005-068.180. https://espis.boem.gov/final%20reports/3482.pdf

Fedders ER, Mahoney AR, Dammann DO, Polashenski C, hutchings JK. 2024, in press. Two-dimensional thermal and dynamical strain in landfast sea ice from InSAR: results from a new analytical inverse method and field observations. Annals of Glaciology. 92 doi,

Flather RA. 1976. A Tidal Model of the North-west European Continental Shelf. Memoires de la Societe Royale de Sciences de Liege. 6:141-164 doi, https://books.google.com/books?id=KX40zwEACAAJ

Fox-Kemper B, Danabasoglu G, Ferrari R, Griffies SM, Hallberg RW, Holland MM, Maltrud ME, Peacock S, Samuels BL. 2011. Parameterization of mixed layer eddies. III: Implementation and impact in global ocean climate simulations. Ocean Modelling. 39(1):61-78 doi: https://doi.org/10.1016/j.ocemod.2010.09.002.

Fox-Kemper B, Ferrari R, Hallberg R. 2008. Parameterization of Mixed Layer Eddies. Part I: Theory and Diagnosis. Journal of Physical Oceanography. 38(6):1145-1165 doi: https://doi.org/10.1175/2007JPO3792.1.

Fox-Kemper B, Hewitt HT, Xiao C, Aðalgeirsdóttir G, Drijfhout SS, Edwards TL, Golledge NR, Hemer M, Kopp RE, Krinner G, Mix A, Notz D, Nowicki S, Nurhati IS, Ruiz L, Sallée JB, Slangen ABA, Yu Y. 2021. Ocean, Cryosphere and Sea Level Change. In: Masson-Delmotte V, Zhai P, Pirani A, Connors SL, Péan C, Berger S, Caud N, Chen Y, Goldfarb L, Gomis MI et al., editors. Climate Change 2021: The Physical Science Basis Contribution of Working Group I to the Sixth Assessment Report of the Intergovernmental Panel on Climate Change. Cambridge, United Kingdom and New York, NY, USA: Cambridge University Press. p. 1211–1362.

Galley RJ, Else BGT, Howell SEL, Lukovich JV, Barber DG. 2012. Landfast Sea Ice Conditions in the Canadian Arctic: 1983-2009. Arctic. 65(2):133-144 doi, http://www.jstor.org/stable/41638586

GEBCO Compilation Group. 2020. GEBCO 2020 Grid. doi:10.5285/a29c5465-b138-234d-e053-6c86abc040b9. [accessed]

George JC, Huntington HP, Brewster K, Eicken H, Norton DW, Glenn R. 2004. Observations on Shorefast Ice Dynamics in Arctic Alaska and the Responses of the Iñupiat Hunting Community. Arctic. 57(4):363-374 doi,

Glisan JM, Gutowski Jr WJ, Cassano JJ, Cassano EN, Seefeldt MW. 2016. Analysis of WRF extreme daily precipitation over Alaska using self-organizing maps. Journal of Geophysical Research: Atmospheres. 121(13):7746-7761 doi: https://doi.org/10.1002/2016JD024822.

Gough AJ, Mahoney AR, Langhorne PJ, Williams MJM, Robinson NJ, Haskell TG. 2012. Signatures of supercooling: McMurdo Sound platelet ice. Journal of Glaciology. 58(207):38-50 doi: 10.3189/2012JoG10J218.

Graham RM, Hudson SR, Maturilli M. 2019. Improved Performance of ERA5 in Arctic Gateway Relative to Four Global Atmospheric Reanalyses. Geophysical Research Letters. 46(11):6138-6147 doi: https://doi.org/10.1029/2019GL082781.

Granskog MA, Ehn J, Niemel‰ M. 2005. Characteristics and potential impacts of under-ice river plumes in the seasonally ice-covered Bothnian Bay (Baltic Sea). Journal of Marine Systems. 53(1-4):187-196 doi, http://www.sciencedirect.com/science/article/B6VF5-4D98K2P-1/2/69e0b87e758bf4ec0a74c0196daa0743

Griffies SM, Hallberg RW. 2000. Biharmonic Friction with a Smagorinsky-Like Viscosity for Use in Large-Scale Eddy-Permitting Ocean Models. Monthly Weather Review. 128(8):2935-2946 doi: https://doi.org/10.1175/1520-0493(2000)128<2935:BFWASL>2.0.CO;2.

Hartl L, Stuefer M. 2020. The Mountain Weather and Climate of Denali, Alaska-An Overview. Journal of Applied Meteorology and Climatology. 59:621-636 doi: 10.1175/JAMC-D-19-0105.1.

Hersbach H, Bell B, Berrisford P, Biavati G, Horányi A, Muñoz Sabater J, Nicolas J, Peubey C, Radu R, Rozum I, Schepers D, Simmons A, Soci C, Dee D, Thépaut J-N. 2023. ERA5 hourly data on single levels from 1940 to present. 10.24381/cds.adbb2d47. [accessed 2023]

Hersbach H, Bell B, Berrisford P, Hirahara S, Horányi A, Muñoz-Sabater J, Nicolas J, Peubey C, Radu R, Schepers D, Simmons A, Soci C, Abdalla S, Abellan X, Balsamo G, Bechtold P, Biavati G, Bidlot J, Bonavita M, De Chiara G, Dahlgren P, Dee D, Diamantakis M, Dragani R, Flemming J, Forbes R, Fuentes M, Geer A, Haimberger L, Healy S, Hogan RJ, Hólm E, Janisková M, Keeley S, Laloyaux P, Lopez P, Lupu C, Radnoti G, de Rosnay P, Rozum I, Vamborg F, Villaume S, Thépaut J-N. 2020. The ERA5 global reanalysis. Quarterly Journal of the Royal Meteorological Society. 146(730):1999-2049 doi: https://doi.org/10.1002/qj.3803.

Hibler WDI. 1980. Modeling a Variable Thickness Sea Ice Cover. Monthly Weather Review. 108(12):1943-1973 doi: 10.1175/1520-0493(1980)108<1943:mavtsi>2.0.co;2.

Hill DF, Bruhis N, Calos SE, Arendt A, Beamer J. 2015. Spatial and temporal variability of freshwater discharge into the Gulf of Alaska. Journal of Geophysical Research: Oceans. 120(2):634-646 doi: https://doi.org/10.1002/2014JC010395.

Hirano D, Fukamachi Y, Watanabe E, Ohshima KI, Iwamoto K, Mahoney AR, Eicken H, Simizu D, Tamura T. 2016. A wind-driven, hybrid latent and sensible heat coastal polynya off Barrow, Alaska. Journal of Geophysical Research-Oceans. 121(1):980-997 doi: 10.1002/2015jc011318.

Hogenson K, Arko SA, Buechler B, Hogenson R, Herrmann J, Geiger A. Year. Hybrid Pluggable Processing Pipeline (HyP3): A cloud-based infrastructure for generic processing of SAR data. AGU Fall Meeting Abstracts; 2016/12/1 2016. IN21B-1740. https://ui.adsabs.harvard.edu/abs/2016AGUFMIN21B1740H

Hunke E, Allard R, Bailey DA, Blain P, Craig A, Dupont F, DuVivier A, Grumbine R, Hebert D, Holland M, Jeffery N, Lemieux J-F, Osinski R, Rasmussen T, Ribergaard M, Roach L, Roberts A, Steketee A, Turner M, Winton M. 2024. CICE-Consortium/Icepack: Icepack 1.4.1 (1.4.1). . Zenodo. . [accessed

Hunke EC, Dukowicz JK. 1997. An Elastic–Viscous–Plastic Model for Sea Ice Dynamics. Journal of Physical Oceanography. 27(9):1849-1867 doi: https://doi.org/10.1175/1520-0485(1997)027<1849:AEVPMF>2.0.CO;2.

Ingram G, Larouche P. 1987. Changes in the under-ice characteristics of La Grande Rivière plume due to discharge variations. Atmosphere-Ocean. 25(3):242-250 doi: https://doi.org/10.1080/07055900.1987.9649273.

Itkin P, Losch M, Gerdes R. 2015. Landfast ice affects the stability of the Arctic halocline: Evidence from a numerical model. Journal of Geophysical Research: Oceans. 120(4):2622-2635 doi: 10.1002/2014JC010353.

Jackson L, Hallberg R, Legg S. 2008. A Parameterization of Shear-Driven Turbulence for Ocean Climate Models. Journal of Physical Oceanography. 38(5):1033-1053 doi: https://doi.org/10.1175/2007JPO3779.1.

Jensen DA, Nandan V, Mahoney AR, Yackel JJ, Resler LM. 2023. Landfast sea ice break out patterns in the northern Bering Sea observed from C-band Synthetic Aperture Radar. International Journal of Applied Earth Observation and Geoinformation. 117:103183 doi: https://doi.org/10.1016/j.jag.2023.103183.

Jones J, Eicken H, Mahoney A, Rohith M, Kambhamettu C, Fukamachi Y, Ohshima KI, George JC. 2016. Landfast sea ice breakouts: Stabilizing ice features, oceanic and atmospheric forcing at Barrow, Alaska. Continental Shelf Research. 126:50-63 doi,

Kasper JL, Weingartner TJ. 2015. The Spreading of a Buoyant Plume Beneath a Landfast Ice Cover. Journal of Physical Oceanography. 45(2):478-494 doi: 10.1175/jpo-d-14-0101.1.

Kohonen T. 1989. Self-Organization and Associative Memory: 3rd edition. Springer Berlin, Heidelberg.

Kohonen T. 1990. The self-organizing map. Proceedings of the IEEE. 78(9):1464-1480 doi: 10.1109/5.58325.

Laidre KL, Stern H, Kovacs KM, Lowry L, Moore SE, Regehr EV, Ferguson SH, Wiig Ø, Boveng P, Angliss RP, Born EW, Litovka D, Quakenbush L, Lydersen C, Vongraven D, Ugarte F. 2015. Arctic marine mammal population status, sea ice habitat loss, and conservation recommendations for the 21st century. Conservation Biology. 29(3):724-737 doi: 10.1111/cobi.12474.

Lantuit H, Pollard WH. 2008. Fifty years of coastal erosion and retrogressive thaw slump activity on Herschel Island, southern Beaufort Sea, Yukon Territory, Canada. Geomorphology. 95(1-2):84-102 doi, http://www.sciencedirect.com/science/article/B6V93-4NS0KH7-1/2/ceb10297f2c960ba3e380bd577ff1358

Lemieux J-F, Dupont F, Blain P, Roy F, Smith GC, Flato GM. 2016. Improving the simulation of landfast ice by combining tensile strength and a parameterization for grounded ridges. Journal of Geophysical Research: Oceans. 121(10):7354-7368 doi: doi:10.1002/2016JC012006.

Lemieux J-F, Tremblay LB, Dupont F, Plante M, Smith GC, Dumont D. 2015. A basal stress parameterization for modeling landfast ice. Journal of Geophysical Research: Oceans. 120(4):3157-3173 doi: 10.1002/2014JC010678.

Libert L, Wuite J, Nagler T. 2022. Automatic delineation of cracks with Sentinel-1 interferometry for monitoring ice shelf damage and calving. The Cryosphere. 16(4):1523-1542 doi: 10.5194/tc-16-1523-2022.

Lovvorn JR, Rocha AR, Mahoney AH, Jewett SC. 2018. Sustaining ecological and subsistence functions in conservation areas: eider habitat and access by Native hunters along landfast ice. Environmental Conservation. 10.1017/S0376892918000103:1-9 doi: 10.1017/S0376892918000103.

Mahoney A, Eicken H, Shapiro L, Graves A. Year. Dempsey JP, editor. Defining and locating the seaward landfast ice edge in northern Alaska. 18th International Conference on Port and Ocean Engineering under Arctic Conditions (POAC '05); 2006; Potsdam, N.Y. 991-1001.

Mahoney AR. 2018. Landfast Sea Ice in a Changing Arctic. In: Osborne E, Richter-Menge JA, Jeffries MO, editors. Arctic Report Card 2018. https://arctic.noaa.gov/Report-Card/Report-Card-2018/ArtMID/7878/ArticleID/788/Landfast-Sea-Ice-in-a-Changing-Arctic

Mahoney AR, Eicken H, Gaylord AG, Gens R. 2014. Landfast sea ice extent in the Chukchi and Beaufort Seas: The annual cycle and decadal variability. Cold Regions Science and Technology. 103(0):41-56 doi: http://dx.doi.org/10.1016/j.coldregions.2014.03.003.

Mahoney AR, Eicken H, Gaylord AG, Shapiro L. 2007. Alaska landfast sea ice: Links with bathymetry and atmospheric circulation. Journal of Geophysical Research-Oceans. 112(C02001) doi: C02001 doi 10.1029/2006jc003559.

Mahoney AR, Eicken H, Shapiro LH, Gens R, Heinrichs T, Meyer FJ, Gaylord A. 2012. Mapping and Characterization of Recurring Spring Leads and Landfast Ice in the Beaufort and Chukchi Seas. (University of Alaska Fairbanks) University of Alaska Coastal Marine Institute and U.S. Department of the Interior, Bureau of Ocean Energy Management, Alaska OCS Region Fairbanks, AK. Final Report, OCS Study BOEM 2012-067.179p. https://espis.boem.gov/final%20reports/5226.pdf

Mahoney AR, Hutchings JK, Eicken H, Haas C. 2019. Changes in the Thickness and Circulation of Multiyear Ice in the Beaufort Gyre Determined From Pseudo-Lagrangian Methods from 2003–2015. Journal of Geophysical Research: Oceans. 124(8):5618-5633 doi: 10.1029/2018jc014911.

Mahoney AR, Turner KE, Hauser DDW, Laxague NJM, Lindsay JM, Whiting AV, Witte CR, Goodwin J, Harris C, Schaeffer RJ, Schaeffer R, Betcher S, Subramaniam A, Zappa CJ. 2021. Thin ice, deep snow and surface flooding in Kotzebue Sound: landfast ice mass balance during two anomalously warm winters and implications for marine mammals and subsistence hunting. Journal of Glaciology. 10.1017/jog.2021.49:1-15 doi: 10.1017/jog.2021.49.

Manizza M, Le Quéré C, Watson AJ, Buitenhuis ET. 2005. Bio-optical feedbacks among phytoplankton, upper ocean physics and sea-ice in a global model. Geophysical Research Letters. 32(5) doi: https://doi.org/10.1029/2004GL020778.

Marchesiello P, McWilliams JC, Shchepetkin A. 2001. Open boundary conditions for long-term integration of regional oceanic models. Ocean Modelling. 3(1):1-20 doi: https://doi.org/10.1016/S1463-5003(00)00013-5.

Masterson DM. 2009. State of the art of ice bearing capacity and ice construction. Cold Regions Science & Technology. 58(3):99-112 doi: 10.1016/j.coldregions.2009.04.002.

Meyer FJ, Mahoney AR, Eicken H, Denny CL, Druckenmiller HC, Hendricks S. 2011. Mapping arctic landfast ice extent using L-band synthetic aperture radar interferometry. Remote Sensing of Environment. 115(12):3029-3043 doi, http://www.sciencedirect.com/science/article/pii/S0034425711002306

NCEP. 2023. 4x Daily Sigma Level 0.995 Air Temperatures. NOAA Physical Sciences Laboratory. http://www.psl.noaa.gov/data/gridded/data.ncep.reanalysis.html[accessed Sep 21, 2023]

Nguyen AT, Menemenlis D, Kwok R. 2009. Improved modeling of the Arctic halocline with a subgrid-scale brine rejection parameterization. Journal of Geophysical Research: Oceans. 114(C11) doi: https://doi.org/10.1029/2008JC005121.

Orlanski I. 1976. A simple boundary condition for unbounded hyperbolic flows. Journal of Computational Physics. 21(3):251-269 doi: https://doi.org/10.1016/0021-9991(76)90023-1.

Ovall B, Pickart RS, Lin P, Stabeno P, Weingartner T, Itoh M, Kikuchi T, Dobbins E, Bell S. 2021. Ice, wind, and water: Synoptic-scale controls of circulation in the Chukchi Sea. Progress in Oceanography. 199:102707 doi: https://doi.org/10.1016/j.pocean.2021.102707.

Peng G, Meier WN. 2018. Temporal and regional variability of Arctic sea-ice coverage from satellite data. Annals of Glaciology. 59(76pt2):191-200 doi: 10.1017/aog.2017.32.

Pickart RS, Moore GWK, Torres DJ, Fratantoni PS, Goldsmith RA, Yang JY. 2009. Upwelling on the continental slope of the Alaskan Beaufort Sea: Storms, ice, and oceanographic response. Journal of Geophysical Research-Oceans. 114 doi: Artn C00a13, doi10.1029/2008jc005009.

Pilfold NW, Derocher AE, Stirling I, Richardson E. 2014. Polar bear predatory behaviour reveals seascape distribution of ringed seal lairs. Population Ecology. 56(1):129-138 doi: Doi 10.1007/S10144-013-0396-Z.

Polashenski C, Perovich D, Courville Z. 2012. The mechanisms of sea ice melt pond formation and evolution. Journal of Geophysical Research-Oceans. 117 doi: Artn C01001. Doi 10.1029/2011jc007231.

Polzin KL. 2009. An abyssal recipe. Ocean Modelling. 30(4):298-309 doi: https://doi.org/10.1016/j.ocemod.2009.07.006.

Potter RE, Walden JT, Haspel RA. 1981. Design and construction of sea ice roads in the Alaskan Beaufort Sea. Paper presented at: Offshore Technology Conference. Houston, Texas.

Pratt JW. 2022. Mapping Bottomfast Sea Ice in Arctic Lagoons Using Sentinel-1 Interferometery [M.S.]. [http://hdl.handle.net/11122/13090]: University of Alaska Fairbanks.

Ravens TOM, Henke M, Ferreira C. 2023. ARCTIC COASTAL STORMS, UNIQUE IN CHARACTER AND IMPACT. Coastal Sediments 2023. WORLD SCIENTIFIC. p. 2434-2461. https://doi.org/10.1142/9789811275135_0223

Reichl BG, Hallberg R. 2018. A simplified energetics based planetary boundary layer (ePBL) approach for ocean climate simulations. Ocean Modelling. 132:112-129 doi: https://doi.org/10.1016/j.ocemod.2018.10.004.

Ross AC, Stock CA, Adcroft A, Curchitser E, Hallberg R, Harrison MJ, Hedstrom K, Zadeh N, Alexander M, Chen W, Drenkard EJ, du Pontavice H, Dussin R, Gomez F, John JG, Kang D, Lavoie D, Resplandy L, Roobaert A, Saba V, Shin SI, Siedlecki S, Simkins J. 2023. A high-resolution physical–biogeochemical model for marine resource applications in the northwest Atlantic (MOM6-COBALT-NWA12 v1.0). Geosci Model Dev. 16(23):6943-6985 doi: 10.5194/gmd-16-6943-2023.

Salganik E, Lange BA, Katlein C, Matero I, Anhaus P, Muilwijk M, Høyland KV, Granskog MA. 2023. Observations of preferential summer melt of Arctic sea-ice ridge keels from repeated multibeam sonar surveys. The Cryosphere. 17(11):4873-4887 doi: 10.5194/tc-17-4873-2023.

Selyuzhenok V, Krumpen T, Mahoney A, Janout M, Gerdes R. 2015. Seasonal and interannual variability of fast ice extent in the southeastern Laptev Sea between 1999 and 2013. Journal of Geophysical Research: Oceans. 120(12):7791-7806 doi: 10.1002/2015JC011135.

Smith TG, Hammill MO, Taugbøl G. 1991. A review of the developmental, behavioural and physiological adaptations of the ringed seal, Phoca hispida, to life in the Arctic winter. Arctic. 44:124–131 doi: doi: http://dx.doi.org/10.14430/arctic1528.

Stabeno PJ, McCabe RM. 2023. Re-examining flow pathways over the Chukchi Sea continental shelf. Deep Sea Research Part II: Topical Studies in Oceanography. 207:105243 doi: https://doi.org/10.1016/j.dsr2.2022.105243.

Thorndike AS, Rothrock DA, Maykut GA, Colony R. 1975. The thickness distribution of sea ice. J Geophys Res. 80:4501-4513 doi,

Torgerson LJ, Stringer WJ. 1985. Observations of Double Arch Formation in the Bering Strait. Geophys Res Lett. 12(10):677-680 doi: https://doi.org/10.1029/GL012i010p00677.

Tsujino H, Urakawa S, Nakano H, Small RJ, Kim WM, Yeager SG, Danabasoglu G, Suzuki T, Bamber JL, Bentsen M, Böning CW, Bozec A, Chassignet EP, Curchitser E, Boeira Dias F, Durack PJ, Griffies SM, Harada Y, Ilicak M, Josey SA, Kobayashi C, Kobayashi S, Komuro Y, Large WG, Le Sommer J, Marsland SJ, Masina S, Scheinert M, Tomita H, Valdivieso M, Yamazaki D. 2018. JRA-55 based surface dataset for driving ocean–sea-ice models (JRA55-do). Ocean Modelling. 130:79-139 doi: https://doi.org/10.1016/j.ocemod.2018.07.002.

U.S. National Ice Center. 2022. U.S. National Ice Center Arctic and Antarctic Sea Ice Charts in SIGRID-3 Format, Version 1 National Snow and Ice Data Center, Boulder, CO. https://doi.org/10.7265/4b7s-rn93. . [accessed 01-01-2023]

Vettigli G. 2018. Minisom: Self organizing maps. GitHub. https://github.com/JustGlowing/minisom. [accessed 2023]

Weingartner T, Aagaard K, Woodgate R, Danielson S, Sasaki Y, Cavalieri D. 2005. Circulation on the north central Chukchi Sea shelf. Deep-Sea Research Part Ii-Topical Studies in Oceanography. 52(24-26):3150-3174 doi: 10.1016/j.dsr2.2005.10.015.

Woodgate RA, Weingartner T, Lindsay R. 2010. The 2007 Bering Strait oceanic heat flux and anomalous Arctic sea-ice retreat. Geophys Res Lett. 37(1):L01602 doi: 10.1029/2009gl041621.

Wright DG. 1997. An Equation of State for Use in Ocean Models: Eckart's Formula Revisited. Journal of Atmospheric and Oceanic Technology. 14(3):735-740 doi: https://doi.org/10.1175/1520-0426(1997)014<0735:AEOSFU>2.0.CO;2.

Yu Y, Stern H, Fowler C, Fetterer F, Maslanik J. 2014. Interannual Variability of Arctic Landfast Ice between 1976 and 2007. Journal of Climate. 27(1):227-243 doi: 10.1175/JCLI-D-13-00178.1.

Zhang X, Walsh JE, Zhang J, Bhatt US, Ikeda M. 2004. Climatology and Interannual Variability of Arctic Cyclone Activity: 1948–2002. Journal of Climate. 17(12):2300-2317 doi: https://doi.org/10.1175/1520-0442(2004)017<2300:CAIVOA>2.0.CO;2.

Appendix A Catalog of Breakout Events

A.1 Chukchi region breakout events

The 161 breakout events identified the Chukchi region from the EM2024 according to the criteria described in Section 2.2.7 are listed in Table A-1 below. The columns in this table are explained below:

ID: Each breakout is assigned a number based on its chronological sequence in the dataset.
SLIE file: This the image in which the reduced landfast ice extent can be seen.
SLIE date: This is the date corresponding to this image, as discussed in Section 2.2.2.
V_0: The first coast vector bounding the breakup region.
V_1: The last coast vector bounding the breakup region.
W: the mean width reduction (km) measured across all coast vectors between V_0 and V_1.
L: The length (km) along the coast between the origin points of V_0 and V_1.
A: The area (km^2)of landfast ice involved in the breakout.
Latitude: The latitude (in decimal degrees) of the centroid of the breakout area.
Longitude: The longitude (in decimal degrees) of the centroid of the breakout area.

Table A-1: Catalog of breakout events identified in the Chukchi region.

ID	Season	SLIE file	SLIE date	v_0	v_1	W (km)	L (km)	A (km^2)	Latitude	Longitude
1	1996-97	r19970108_dailyslie.tif	1997-01-08	5064	5190	2.9	52.4	126.9	69.419	-163.178
2	1996-97	r19970329_dailyslie.tif	1997-03-29	949	1195	3.2	72.3	154.8	66.236	-169.980
3	1996-97	r19970407_dailyslie.tif	1997-04-07	773	865	0.6	25.4	18.6	66.540	-170.984
4	1997-98	r19980103_dailyslie.tif	1998-01-03	6159	6331	1.2	12	9.5	70.531	-160.318
5	1997-98	r19980413_dailyslie.tif	1998-04-13	6009	6331	6.7	78.9	402.7	70.458	-160.893
6	1998-99	r19990122_dailyslie.tif	1999-01-22	6900	6956	1.8	36.5	24	66.519	-163.566
7	1998-99	r19990130_dailyslie.tif	1999-01-30	844	1349	3.2	108.8	318.4	66.334	-170.276
8	1999-00	r20000113_dailyslie.tif	2000-01-13	550	638	4	26.7	114.8	66.854	-171.533
9	2000-01	r20010107_dailyslie.tif	2001-01-07	5185	5244	1.5	7.6	9.2	69.628	-163.111
10	2000-01	r20010107_dailyslie.tif	2001-01-07	5769	6026	1.9	31.9	45.8	70.326	-161.747
11	2000-01	r20010126_dailyslie.tif	2001-01-26	2	365	8.2	86.2	786.6	67.102	-172.882
12	2000-01	r20010204_dailyslie.tif	2001-02-04	587	624	2	13.5	25.9	66.849	-171.592
13	2000-01	r20010204_dailyslie.tif	2001-02-04	782	1111	7	111.6	521.7	66.391	-170.401
14	2000-01	r20010204_dailyslie.tif	2001-02-04	1628	2052	11.8	98.6	727.1	65.866	-167.719
15	2000-01	r20010204_dailyslie.tif	2001-02-04	2629	2812	4.2	167.9	209.1	66.543	-164.490
16	2000-01	r20010204_dailyslie.tif	2001-02-04	4800	5072	4.8	90.5	436.4	69.042	-164.036
17	2000-01	r20010204_dailyslie.tif	2001-02-04	5701	6010	2.2	40	84	70.285	-161.995
18	2000-01	r20010204_dailyslie.tif	2001-02-04	6064	6096	1.8	13.6	21	70.334	-161.055
19	2000-01	r20010219_dailyslie.tif	2001-02-19	6673	6711	1.3	23.9	23.9	66.046	-162.417
20	2001-02	r20020303_dailyslie.tif	2002-03-03	2	39	2.4	13.6	29.5	67.116	-173.452
21	2001-02	r20020421_dailyslie.tif	2002-04-21	550	1343	6.4	179.5	1072.2	66.513	-170.693

ID	Season	SLIE file	SLIE date	v_0	v_1	W (km)	L (km)	A (km^2)	Latitude	Longitude
22	2001-02	r20020428_dailyslie.tif	2002-04-28	747	782	0.4	12.7	5.2	66.617	-171.203
23	2001-02	r20020428_dailyslie.tif	2002-04-28	1832	1988	0.6	40.3	16.2	65.849	-167.460
24	2002-03	r20030219_dailyslie.tif	2003-02-19	1787	2262	11.3	121.6	874.8	66.033	-167.347
25	2002-03	r20030301_dailyslie.tif	2003-03-01	512	638	0.7	27	25.8	66.842	-171.548
26	2002-03	r20030301_dailyslie.tif	2003-03-01	789	1055	6.2	71.9	381.9	66.425	-170.488
27	2002-03	r20030403_dailyslie.tif	2003-04-03	490	869	3.8	80.5	371.1	66.670	-171.156
28	2002-03	r20030403_dailyslie.tif	2003-04-03	1690	2748	25.4	264.5	4464.8	66.274	-166.727
29	2004-05	r20050102_dailyslie.tif	2005-01-02	980	1044	0.3	3.9	1.5	66.287	-170.221
30	2004-05	r20050102_dailyslie.tif	2005-01-02	2656	2765	1	30.8	29	66.541	-164.700
31	2004-05	r20050102_dailyslie.tif	2005-01-02	5861	6077	3.2	49.7	169.5	70.334	-161.474
32	2004-05	r20050102_dailyslie.tif	2005-01-02	6664	6708	1.8	25.5	40.2	66.054	-162.344
33	2004-05	r20050102_dailyslie.tif	2005-01-02	6849	6952	3.4	71.3	99	66.408	-163.665
34	2004-05	r20050111_dailyslie.tif	2005-01-11	5051	5107	0.4	22.1	9.1	69.293	-163.273
35	2004-05	r20050203_dailyslie.tif	2005-02-03	947	1064	1.6	35.9	22.6	66.306	-170.219
36	2005-06	r20060204_dailyslie.tif	2006-02-04	430	1329	7.9	179.5	1582.8	66.509	-170.633
37	2005-06	r20060204_dailyslie.tif	2006-02-04	1502	2929	30.6	582.3	10487	66.420	-165.160
38	2005-06	r20060204_dailyslie.tif	2006-02-04	4765	5218	6	149.1	834.6	69.158	-163.873
39	2005-06	r20060204_dailyslie.tif	2006-02-04	5678	6097	9.9	90.7	595.3	70.354	-161.712
40	2005-06	r20060204_dailyslie.tif	2006-02-04	6140	6331	0.6	19	17.6	70.492	-160.424
41	2005-06	r20060204_dailyslie.tif	2006-02-04	6346	6956	39	384.9	4256.9	66.393	-162.859
42	2005-06	r20060214_dailyslie.tif	2006-02-14	2	236	6.4	67.5	333.9	67.090	-172.851
43	2006-07	r20070124_dailyslie.tif	2007-01-24	5056	5084	0.6	11.4	5.8	69.262	-163.342
44	2006-07	r20070203_dailyslie.tif	2007-02-03	5752	6003	2	17.6	20.2	70.329	-161.919
45	2007-08	r20080114_dailyslie.tif	2008-01-14	2376	2496	1.3	14.7	21.5	66.376	-165.615
46	2007-08	r20080114_dailyslie.tif	2008-01-14	2673	2838	1.8	197.3	143.1	66.433	-163.261
47	2007-08	r20080114_dailyslie.tif	2008-01-14	4331	5090	9.5	145.2	1327	68.977	-164.793
48	2007-08	r20080114_dailyslie.tif	2008-01-14	5154	5274	1.6	37.5	40.9	69.625	-163.096
49	2007-08	r20080114_dailyslie.tif	2008-01-14	5282	5548	3.1	43.8	234.5	69.943	-162.692
50	2007-08	r20080114_dailyslie.tif	2008-01-14	5737	6151	6	89.6	419.4	70.338	-161.474
51	2007-08	r20080114_dailyslie.tif	2008-01-14	6721	6941	6.8	118.9	438.8	66.269	-163.445
52	2007-08	r20080305_dailyslie.tif	2008-03-05	357	576	1.4	16.5	45.8	66.977	-171.795
53	2007-08	r20080324_dailyslie.tif	2008-03-24	2137	2939	13.1	480.5	2180.7	66.581	-165.245
54	2007-08	r20080403_dailyslie.tif	2008-04-03	2	970	25.9	220.7	4471.9	67.094	-171.891
55	2007-08	r20080413_dailyslie.tif	2008-04-13	717	1323	9.4	144.6	1258.1	66.461	-170.510
56	2007-08	e20080430_dailyslie.tif	2008-04-30	1019	1047	0.2	2.6	0.9	66.280	-170.195
57	2007-08	e20080430_dailyslie.tif	2008-04-30	2483	2561	0.8	7.9	6.1	66.401	-165.488
58	2007-08	e20080430_dailyslie.tif	2008-04-30	4986	5101	5.7	43.6	220.2	69.233	-163.530
59	2008-09	c20090104_dailyslie.tif	2009-01-04	1987	2848	12.9	386.9	3363.3	66.453	-164.123
60	2008-09	c20090104_dailyslie.tif	2009-01-04	3117	3731	2.2	154.8	332.1	68.088	-165.875

ID	Season	SLIE file	SLIE date	v_0	v_1	W (km)	L (km)	A (km^2)	Latitude	Longitude
61	2008-09	c20090104_dailyslie.tif	2009-01-04	6892	6956	2.1	39.9	32.1	66.506	-163.580
62	2008-09	c20090125_dailyslie.tif	2009-01-25	3549	4351	5.1	136.8	645.6	68.458	-166.417
63	2008-09	c20090308_dailyslie.tif	2009-03-08	764	1190	2.6	121.5	282	66.388	-170.495
64	2008-09	c20090419_dailyslie.tif	2009-04-19	104	378	3	54.6	188	67.011	-172.224
65	2008-09	c20090419_dailyslie.tif	2009-04-19	582	636	1.5	21	28.1	66.832	-171.584
66	2008-09	c20090419_dailyslie.tif	2009-04-19	718	856	1.4	44.5	64.2	66.629	-171.202
67	2009-10	c20100207_dailyslie.tif	2010-02-07	1	767	1.6	149.6	247.9	67.005	-172.419
68	2009-10	c20100311_dailyslie.tif	2010-03-11	640	1115	3.5	142	403	66.394	-170.502
69	2009-10	c20100401_dailyslie.tif	2010-04-01	264	377	0.4	12.5	7.2	66.962	-171.862
70	2010-11	c20110104_dailyslie.tif	2011-01-04	1765	2830	2.5	414.2	715	66.365	-164.616
71	2010-11	c20110224_dailyslie.tif	2011-02-24	6774	6956	1.4	115.6	61	66.376	-163.466
72	2012-13	c20130221_dailyslie.tif	2013-02-21	261	1112	4	190	698.5	66.517	-170.773
73	2012-13	c20130221_dailyslie.tif	2013-02-21	5998	6162	1.6	74.7	91.3	70.358	-161.241
74	2012-13	c20130331_dailyslie.tif	2013-03-31	6124	6183	0.6	22.1	11.5	70.468	-160.488
75	2013-14	c20140115_dailyslie.tif	2014-01-15	250	372	0.8	16.1	14.3	66.969	-171.920
76	2013-14	c20140122_dailyslie.tif	2014-01-22	6152	6183	0.6	11	6.5	70.496	-160.411
77	2013-14	c20140216_dailyslie.tif	2014-02-16	1799	2245	6.2	109.9	453.9	65.995	-167.238
78	2013-14	c20140406_dailyslie.tif	2014-04-06	485	605	0.2	16.5	4.6	66.870	-171.657
79	2013-14	c20140427_dailyslie.tif	2014-04-27	3158	3240	1	27.4	22.1	67.779	-164.637
80	2014-15	c20150128_dailyslie.tif	2015-01-28	264	427	0.7	16	12.5	66.961	-171.827
81	2014-15	c20150204_dailyslie.tif	2015-02-04	6386	6452	3.9	54.8	86.8	66.822	-162.798
82	2014-15	c20150311_dailyslie.tif	2015-03-11	14	374	2.5	85.4	203.8	67.029	-172.478
83	2014-15	c20150311_dailyslie.tif	2015-03-11	3618	3701	1.4	29.7	40.1	68.309	-166.614
84	2014-15	c20150311_dailyslie.tif	2015-03-11	6749	6797	0.7	22.3	14.4	66.075	-163.252
85	2014-15	c20150318_dailyslie.tif	2015-03-18	6607	6723	0.9	99.6	46.1	66.169	-162.282
86	2014-15	c20150401_dailyslie.tif	2015-04-01	3629	3685	1.1	19.9	20.4	68.303	-166.499
87	2015-16	c20160104_dailyslie.tif	2016-01-04	6785	6941	3.2	89.8	170.3	66.264	-163.626
88	2015-16	c20160106_dailyslie.tif	2016-01-06	2904	2930	1.7	38.6	24.7	66.964	-162.771
89	2015-16	c20160106_dailyslie.tif	2016-01-06	5788	6139	1.2	77.6	76.8	70.331	-161.309
90	2015-16	c20160124_dailyslie.tif	2016-01-24	6846	6956	3.5	75.4	121.2	66.403	-163.725
91	2015-16	c20160210_dailyslie.tif	2016-02-10	2421	2606	1.1	23	27.6	66.412	-165.467
92	2015-16	c20160210_dailyslie.tif	2016-02-10	6332	6471	12.8	99.8	772.3	66.934	-163.215
93	2015-16	c20160221_dailyslie.tif	2016-02-21	5065	5096	1.1	12.7	12.2	69.290	-163.280
94	2015-16	c20160323_dailyslie.tif	2016-03-23	3094	3377	1.3	79	88.3	67.782	-164.659
95	2015-16	c20160323_dailyslie.tif	2016-03-23	5043	5177	1.3	56	62.1	69.381	-163.239
96	2015-16	c20160324_dailyslie.tif	2016-03-24	4297	5070	6.8	138.4	730.3	68.955	-164.974
97	2015-16	c20160324_dailyslie.tif	2016-03-24	5079	6143	2.5	231	534.9	70.140	-162.085
98	2015-16	c20160329_dailyslie.tif	2016-03-29	2798	2928	14.1	273.1	1205.7	66.512	-162.633
99	2015-16	c20160329_dailyslie.tif	2016-03-29	6385	6795	16.8	254.9	1094.6	66.467	-162.660

ID	Season	SLIE file	SLIE date	v_0	v_1	W (km)	L (km)	A (km^2)	Latitude	Longitude
100	2015-16	c20160329_dailyslie.tif	2016-03-29	6385	6805	16.8	261.8	1123.4	66.464	-162.673
101	2015-16	c20160329_dailyslie.tif	2016-03-29	6819	6854	23.3	22.4	100.1	66.372	-163.250
102	2015-16	c20160330_dailyslie.tif	2016-03-30	5249	5440	0.6	22.5	12.5	69.737	-163.037
103	2015-16	c20160330_dailyslie.tif	2016-03-30	5712	6331	1.9	113.7	161.7	70.365	-161.204
104	2015-16	c20160427_dailyslie.tif	2016-04-27	1526	3116	8.6	680	4489.5	66.616	-164.130
105	2016-17	c20170111_dailyslie.tif	2017-01-11	1071	1108	1.2	25.8	16.3	66.161	-169.980
106	2016-17	c20170125_dailyslie.tif	2017-01-25	5870	6110	4.6	62.7	190.3	70.341	-161.427
107	2016-17	c20170208_dailyslie.tif	2017-02-08	925	965	1.4	27.8	20.5	66.319	-170.456
108	2016-17	c20170208_dailyslie.tif	2017-02-08	1053	1108	1.4	34	28.3	66.179	-170.026
109	2016-17	c20170222_dailyslie.tif	2017-02-22	6717	6882	2	97	129.5	66.152	-163.423
110	2016-17	c20170412_dailyslie.tif	2017-04-12	251	595	1.1	36.2	30.6	66.945	-171.713
111	2017-18	a20180403_dailyslie.tif	2018-04-03	1	382	3.7	92.9	360.7	67.052	-172.831
112	2017-18	a20180410_dailyslie.tif	2018-04-10	2823	2938	16.7	172.1	1211.5	66.651	-162.468
113	2017-18	a20180410_dailyslie.tif	2018-04-10	6340	6715	10.7	245	1778.3	66.493	-162.396
114	2017-18	a20180418_dailyslie.tif	2018-04-18	920	957	1.9	14.1	25.3	66.346	-170.494
115	2017-18	a20180418_dailyslie.tif	2018-04-18	2290	2556	1.9	75.4	76.1	66.329	-165.811
116	2017-18	a20180418_dailyslie.tif	2018-04-18	2663	2724	0.9	12	15	66.524	-164.810
117	2017-18	a20180422_dailyslie.tif	2018-04-22	1816	1892	2	27.5	31.2	65.818	-167.573
118	2017-18	a20180423_dailyslie.tif	2018-04-23	958	1198	1.9	62.5	132.7	66.209	-170.036
119	2017-18	a20180429_dailyslie.tif	2018-04-29	2778	2811	1.2	24.7	17.4	66.599	-163.967
120	2018-19	a20190109_dailyslie.tif	2019-01-09	199	382	8	38.2	224.1	67.062	-172.048
121	2018-19	a20190119_dailyslie.tif	2019-01-19	1670	2811	10	304	2027	66.162	-166.657
122	2018-19	a20190120_dailyslie.tif	2019-01-20	719	1117	5.3	137.3	571.3	66.448	-170.640
123	2018-19	a20190201_dailyslie.tif	2019-02-01	6609	6643	4.2	35.9	68.5	66.229	-161.934
124	2018-19	a20190204_dailyslie.tif	2019-02-04	2101	2232	3.9	15.2	70.8	66.125	-166.628
125	2018-19	a20190216_dailyslie.tif	2019-02-16	2472	2561	1.7	11.5	22.3	66.400	-165.518
126	2018-19	a20190216_dailyslie.tif	2019-02-16	2643	2685	2.3	17.7	32.5	66.509	-164.903
127	2018-19	a20190216_dailyslie.tif	2019-02-16	5947	6153	5.2	79.3	296.5	70.353	-161.341
128	2018-19	a20190220_dailyslie.tif	2019-02-20	6578	6608	2.3	14.8	29.2	66.366	-161.934
129	2018-19	a20190224_dailyslie.tif	2019-02-24	1796	1950	1.6	43.6	50	65.831	-167.557
130	2018-19	a20190309_dailyslie.tif	2019-03-09	2880	2931	21.4	76.2	622.7	66.878	-162.769
131	2018-19	a20190309_dailyslie.tif	2019-03-09	6367	6507	11.8	87.5	660.3	66.887	-162.767
132	2018-19	a20190312_dailyslie.tif	2019-03-12	5935	5965	4.2	0.8	6.6	70.362	-161.878
133	2018-19	a20190318_dailyslie.tif	2019-03-18	6622	6688	1.2	50	37.5	66.112	-162.109
134	2018-19	a20190322_dailyslie.tif	2019-03-22	1831	1946	0.9	31.1	22	65.849	-167.466
135	2018-19	a20190323_dailyslie.tif	2019-03-23	2378	2472	1.7	6	10.6	66.357	-165.683
136	2018-19	a20190326_dailyslie.tif	2019-03-26	1	269	2.5	80.5	192.4	67.031	-172.777
137	2019-20	c20200306_dailyslie.tif	2020-03-06	893	1106	1.4	82.3	79.1	66.270	-170.205
138	2019-20	c20200306_dailyslie.tif	2020-03-06	1655	1990	1.8	72.4	82.4	65.800	-167.736

ID	Season	SLIE file	SLIE date	v_0	v_1	W (km)	L (km)	A (km^2)	Latitude	Longitude
139	2019-20	c20200311_dailyslie.tif	2020-03-11	154	196	0.8	11.2	10	67.016	-172.595
140	2019-20	c20200315_dailyslie.tif	2020-03-15	581	892	0.6	78.5	52	66.639	-171.162
141	2019-20	c20200316_dailyslie.tif	2020-03-16	1870	2011	0.7	32.5	22.4	65.913	-167.253
142	2019-20	c20200325_dailyslie.tif	2020-03-25	65	119	1.2	14.3	17.6	67.062	-172.932
143	2019-20	c20200325_dailyslie.tif	2020-03-25	1071	1108	1.2	25.8	16	66.172	-169.965
144	2019-20	c20200419_dailyslie.tif	2020-04-19	1	70	1.7	24.7	39.7	67.113	-173.293
145	2020-21	c20210114_dailyslie.tif	2021-01-14	6688	6749	1.2	37.6	30.8	66.064	-162.643
146	2020-21	c20210218_dailyslie.tif	2021-02-18	5747	6056	1.3	47.4	39.9	70.311	-161.678
147	2020-21	c20210224_dailyslie.tif	2021-02-24	5465	6331	1.1	163.4	180.6	70.246	-161.769
148	2020-21	c20210228_dailyslie.tif	2021-02-28	5540	5689	1.3	12.4	18	70.106	-162.470
149	2020-21	c20210228_dailyslie.tif	2021-02-28	5708	5798	1.4	18.5	29.5	70.243	-162.125
150	2020-21	c20210303_dailyslie.tif	2021-03-03	3893	4172	1.8	24	28.9	68.412	-166.489
151	2021-22	c20220225_dailyslie.tif	2022-02-25	6332	6456	6.8	94.1	281.5	66.861	-162.971
152	2022-23	a20230120_dailyslie.tif	2023-01-20	37	373	2.1	76.7	165.6	67.056	-172.524
153	2022-23	a20230120_dailyslie.tif	2023-01-20	6659	6913	19.9	151.6	1255.2	66.238	-163.040
154	2022-23	a20230215_dailyslie.tif	2023-02-15	1548	2420	11.8	203.4	1605.7	65.988	-167.376
155	2022-23	a20230215_dailyslie.tif	2023-02-15	6661	6773	3.4	64.1	145.6	66.123	-162.714
156	2022-23	a20230217_dailyslie.tif	2023-02-17	1880	1989	0.8	20.9	12.6	65.884	-167.335
157	2022-23	a20230217_dailyslie.tif	2023-02-17	2421	2485	2.4	9.3	22	66.371	-165.640
158	2022-23	a20230217_dailyslie.tif	2023-02-17	2491	2557	1.7	4	6.1	66.410	-165.468
159	2022-23	a20230220_dailyslie.tif	2023-02-20	2812	2842	3.4	55.1	84.9	66.227	-162.069
160	2022-23	a20230220_dailyslie.tif	2023-02-20	6605	6676	3	68.7	91.6	66.222	-162.087
161	2022-23	a20230329_dailyslie.tif	2023-03-29	5012	5066	1.1	19.7	20.6	69.168	-163.517

A.2 Beaufort region breakout events

The 202 breakout events identified the Beaufort region from the EM2024 according to the criteria described in Section 2.2.7 are listed in Table A-2 below. The columns in this table are explained above in Section A.1.

Table A-2: Catalog of breakout events identified in the Beaufort region

ID	Season	SLIE file	SLIE date	v_0	v_1	W (km)	L (km)	A (km^2)	Latitude	Longitude
1	1996-97	r19970306_dailyslie.tif	1997-03-06	333	373	1.9	20	37.6	71.340	-156.791
2	1997-98	r19980105_dailyslie.tif	1998-01-05	2	78	0.7	25.8	17.1	70.630	-160.077
3	1997-98	r19980105_dailyslie.tif	1998-01-05	2	207	1	50.8	48.5	70.751	-159.736
4	1997-98	r19980105_dailyslie.tif	1998-01-05	1246	1272	1.2	32.6	32.5	70.052	-144.803
5	1997-98	r19980105_dailyslie.tif	1998-01-05	1407	1439	0.6	16	13.6	70.079	-142.885
6	1997-98	r19980116_dailyslie.tif	1998-01-16	216	253	0.7	19.3	9.7	70.894	-159.023
7	1997-98	r19980207_dailyslie.tif	1998-02-07	369	644	12.9	142.7	1782.3	71.383	-155.288
8	1997-98	r19980428_dailyslie.tif	1998-04-28	327	357	0.6	15.2	12	71.264	-156.889
9	1998-99	r19990113_dailyslie.tif	1999-01-13	271	329	3.3	67.9	215.2	70.999	-157.571

ID	Season	SLIE file	SLIE date	v_0	v_1	W (km)	L (km)	A (km^2)	Latitude	Longitude
10	1998-99	r19990113_dailyslie.tif	1999-01-13	552	658	10.9	98.9	704.1	71.147	-154.563
11	1998-99	r19990113_dailyslie.tif	1999-01-13	730	1028	17	232.9	3075.8	70.796	-150.544
12	1998-99	r19990113_dailyslie.tif	1999-01-13	1074	1267	6.3	184.4	879.8	70.297	-146.456
13	1998-99	r19990113_dailyslie.tif	1999-01-13	1453	1565	3.4	111.2	359.2	69.846	-141.846
14	1998-99	r19990113_dailyslie.tif	1999-01-13	1754	1799	11.4	78.8	654.9	69.226	-137.890
15	1998-99	r19990312_dailyslie.tif	1999-03-12	1212	1274	11.3	77.9	647.4	70.164	-145.120
16	1998-99	r19990312_dailyslie.tif	1999-03-12	1363	1524	8.6	87.4	807.7	70.073	-142.186
17	1998-99	r19990421_dailyslie.tif	1999-04-21	878	1936	81.2	885.4	49353	70.349	-140.979
18	1999-00	r20000106_dailyslie.tif	2000-01-06	216	248	1.5	13.3	9	70.891	-159.114
19	1999-00	r20000106_dailyslie.tif	2000-01-06	569	666	6.1	100.5	500.8	71.105	-154.421
20	1999-00	r20000402_dailyslie.tif	2000-04-02	533	1936	77.4	1215.9	61395	70.660	-143.156
21	2000-01	r20010110_dailyslie.tif	2001-01-10	551	780	16.6	183.7	2315.7	71.175	-153.949
22	2000-01	r20010110_dailyslie.tif	2001-01-10	1172	1248	3.8	51.1	253.7	70.112	-145.347
23	2000-01	r20010110_dailyslie.tif	2001-01-10	1309	1360	1.8	20.7	34	70.160	-143.475
24	2000-01	r20010121_dailyslie.tif	2001-01-21	1295	1323	2.2	8	11.2	70.151	-143.717
25	2000-01	r20010201_dailyslie.tif	2001-02-01	1174	1218	1.5	7.9	12.8	70.164	-145.783
26	2000-01	r20010201_dailyslie.tif	2001-02-01	1393	1540	10.8	104.3	1011.6	69.978	-142.173
27	2000-01	r20010306_dailyslie.tif	2001-03-06	164	252	1.1	33.5	26.7	70.876	-159.234
28	2000-01	r20010306_dailyslie.tif	2001-03-06	295	321	1.7	30.6	48.9	71.027	-157.381
29	2000-01	r20010316_dailyslie.tif	2001-03-16	199	253	0.4	27.6	8.2	70.889	-159.098
30	2000-01	r20010327_dailyslie.tif	2001-03-27	2	96	1.5	32.1	46.3	70.646	-160.061
31	2000-01	r20010327_dailyslie.tif	2001-03-27	109	174	0.8	4.9	4.6	70.813	-159.610
32	2000-01	r20010327_dailyslie.tif	2001-03-27	109	179	0.7	9	5.4	70.815	-159.595
33	2000-01	r20010327_dailyslie.tif	2001-03-27	207	233	0.2	7.2	1.6	70.870	-159.220
34	2000-01	r20010327_dailyslie.tif	2001-03-27	314	439	1.1	45.1	66	71.259	-156.886
35	2001-02	r20020104_dailyslie.tif	2002-01-04	1	62	1.5	20.8	30.2	70.628	-160.130
36	2001-02	r20020104_dailyslie.tif	2002-01-04	255	282	3	33.3	92.2	70.860	-158.464
37	2001-02	r20020111_dailyslie.tif	2002-01-11	1908	1936	1.6	0	7.4	69.821	-135.413
38	2001-02	r20020119_dailyslie.tif	2002-01-19	1487	1524	2.3	29.7	65.8	69.859	-141.901
39	2001-02	r20020127_dailyslie.tif	2002-01-27	16	54	0.9	14	10.9	70.643	-160.063
40	2001-02	r20020219_dailyslie.tif	2002-02-19	28	60	0.5	10	5.3	70.667	-159.994
41	2001-02	r20020219_dailyslie.tif	2002-02-19	1889	1936	5.5	0	67.4	69.848	-135.480
42	2001-02	r20020301_dailyslie.tif	2002-03-01	1525	1584	8.4	70.6	478.8	69.738	-140.882
43	2001-02	r20020311_dailyslie.tif	2002-03-11	1	97	0.7	33.1	22.9	70.643	-160.079
44	2001-02	r20020311_dailyslie.tif	2002-03-11	1849	1936	2.6	13.3	68.2	69.826	-135.807
45	2001-02	r20020319_dailyslie.tif	2002-03-19	12	82	0.6	24	13.9	70.663	-160.025
46	2001-02	r20020420_dailyslie.tif	2002-04-20	517	1076	18	481.2	5995.9	71.061	-152.683
47	2001-02	r20020420_dailyslie.tif	2002-04-20	1631	1720	0.4	14.1	3.2	69.646	-139.137
48	2002-03	r20030118_dailyslie.tif	2003-01-18	280	306	0.7	30.7	22.9	70.912	-157.680

ID	Season	SLIE file	SLIE date	v_0	v_1	W (km)	L (km)	A (km^2)	Latitude	Longitude
49	2002-03	r20030118_dailyslie.tif	2003-01-18	1530	1569	1.8	49.4	70.8	69.674	-140.962
50	2002-03	r20030118_dailyslie.tif	2003-01-18	1626	1730	0.4	24.9	9.2	69.618	-139.167
51	2002-03	r20030127_dailyslie.tif	2003-01-27	331	516	3	27.1	132.7	71.355	-156.738
52	2002-03	r20030214_dailyslie.tif	2003-02-14	1682	1734	0.4	11.8	6.1	69.614	-138.922
53	2002-03	r20030222_dailyslie.tif	2003-02-22	1607	1714	0.7	43.7	26.9	69.598	-139.425
54	2002-03	r20030303_dailyslie.tif	2003-03-03	1733	1763	1.5	60.6	52.8	69.417	-138.496
55	2002-03	r20030313_dailyslie.tif	2003-03-13	1631	1690	0.5	10.2	5.1	69.631	-139.177
56	2002-03	r20030401_dailyslie.tif	2003-04-01	303	336	1.2	37.5	45	71.113	-157.205
57	2003-04	r20040202_dailyslie.tif	2004-02-02	251	289	5	46.3	214.4	70.886	-158.309
58	2003-04	r20040212_dailyslie.tif	2004-02-12	80	162	0.5	11.4	4.6	70.781	-159.700
59	2003-04	r20040313_dailyslie.tif	2004-03-13	61	179	0.5	23.8	12.7	70.769	-159.741
60	2004-05	r20050101_dailyslie.tif	2005-01-01	1128	1212	2.7	41.9	112	70.231	-146.240
61	2005-06	r20060104_dailyslie.tif	2006-01-04	1543	1575	7.4	39.4	241	69.692	-140.840
62	2005-06	r20060104_dailyslie.tif	2006-01-04	1587	1691	0.7	51.4	37.1	69.606	-139.528
63	2005-06	r20060114_dailyslie.tif	2006-01-14	315	368	0.7	34.9	19.5	71.250	-156.916
64	2005-06	r20060114_dailyslie.tif	2006-01-14	498	672	31.4	182.7	3317.5	71.355	-154.687
65	2005-06	r20060114_dailyslie.tif	2006-01-14	1425	1492	0.7	41.3	22.2	69.966	-142.429
66	2005-06	r20060203_dailyslie.tif	2006-02-03	2	177	1.9	41.9	89.4	70.708	-159.937
67	2005-06	r20060203_dailyslie.tif	2006-02-03	731	845	11.3	73.8	637.7	70.945	-151.876
68	2005-06	r20060308_dailyslie.tif	2006-03-08	1907	1935	3.2	0	26.5	69.898	-135.399
69	2006-07	r20070101_dailyslie.tif	2007-01-01	1626	1691	0.6	19.6	25.5	69.621	-139.253
70	2006-07	r20070113_dailyslie.tif	2007-01-13	1173	1232	1.5	27.2	41.6	70.150	-145.606
71	2006-07	r20070123_dailyslie.tif	2007-01-23	223	296	4.9	70.2	389.5	70.886	-158.209
72	2006-07	r20070123_dailyslie.tif	2007-01-23	223	300	4.6	74.9	391.3	70.886	-158.206
73	2006-07	r20070221_dailyslie.tif	2007-02-21	517	701	14.3	194.9	1705.1	71.213	-154.341
74	2006-07	r20070221_dailyslie.tif	2007-02-21	1361	1579	8.6	153.6	1275.1	69.888	-141.691
75	2006-07	r20070221_dailyslie.tif	2007-02-21	1743	1794	11.7	83	740.1	69.274	-138.065
76	2006-07	r20070303_dailyslie.tif	2007-03-03	664	723	4.3	39.2	78.5	71.029	-153.165
77	2006-07	r20070323_dailyslie.tif	2007-03-23	304	358	2.1	42.9	96.1	71.200	-157.053
78	2006-07	r20070323_dailyslie.tif	2007-03-23	1420	1590	13.2	143.1	1491.7	69.921	-141.634
79	2006-07	r20070410_dailyslie.tif	2007-04-10	1619	1690	1.2	27.3	51.2	69.639	-139.313
80	2007-08	r20080114_dailyslie.tif	2008-01-14	54	80	0.2	7.8	1.6	70.713	-159.873
81	2007-08	r20080114_dailyslie.tif	2008-01-14	292	364	1.1	61	67.4	71.105	-157.202
82	2007-08	r20080114_dailyslie.tif	2008-01-14	550	733	8.5	168.8	1048.4	71.090	-154.168
83	2007-08	r20080114_dailyslie.tif	2008-01-14	968	1106	5.6	110.8	490.4	70.488	-148.249
84	2007-08	r20080114_dailyslie.tif	2008-01-14	1202	1251	2.2	50.6	108.4	70.071	-145.318
85	2007-08	r20080114_dailyslie.tif	2008-01-14	1415	1533	4.8	80.4	318.8	69.954	-142.247
86	2007-08	r20080114_dailyslie.tif	2008-01-14	1542	1576	1.6	41.7	58.2	69.653	-140.799
87	2007-08	r20080114_dailyslie.tif	2008-01-14	1763	1933	9.7	225.6	1058.4	69.381	-136.742

ID	Season	SLIE file	SLIE date	v_0	v_1	W (km)	L (km)	A (km^2)	Latitude	Longitude
88	2007-08	r20080124_dailyslie.tif	2008-01-24	11	37	0.6	9	4.7	70.618	-160.107
89	2007-08	r20080124_dailyslie.tif	2008-01-24	48	84	0.4	12.9	5.2	70.712	-159.862
90	2007-08	r20080124_dailyslie.tif	2008-01-24	216	254	0.7	20.5	10.7	70.897	-159.024
91	2007-08	r20080124_dailyslie.tif	2008-01-24	1290	1327	1.1	15.6	10.6	70.141	-143.759
92	2007-08	r20080124_dailyslie.tif	2008-01-24	1496	1588	1.9	94.9	154.3	69.707	-141.214
93	2007-08	r20080124_dailyslie.tif	2008-01-24	1682	1731	0.4	8.5	3.6	69.630	-139.003
94	2008-09	c20090113_dailyslie.tif	2009-01-13	252	358	2.8	105.7	303.1	71.005	-157.757
95	2008-09	c20090208_dailyslie.tif	2009-02-08	1759	1791	3.5	53.8	146.9	69.198	-138.059
96	2008-09	c20090222_dailyslie.tif	2009-02-22	1769	1796	3.2	43.2	119.3	69.127	-137.774
97	2008-09	c20090308_dailyslie.tif	2009-03-08	548	1133	4.1	512.7	1441.2	70.844	-150.951
98	2008-09	c20090308_dailyslie.tif	2009-03-08	1637	1744	0.5	40.7	16.7	69.557	-138.897
99	2008-09	c20090329_dailyslie.tif	2009-03-29	1361	1539	4.1	105.1	434.1	69.971	-142.257
100	2008-09	c20090329_dailyslie.tif	2009-03-29	1585	1691	1	53.6	57	69.643	-139.564
101	2008-09	c20090416_dailyslie.tif	2009-04-16	1129	1246	2.5	83.9	165.5	70.161	-145.717
102	2009-10	c20100103_dailyslie.tif	2010-01-03	1633	1735	0.9	34	17.9	69.627	-139.011
103	2009-10	c20100317_dailyslie.tif	2010-03-17	1631	1733	0.5	19.8	8.8	69.634	-139.051
104	2010-11	c20110123_dailyslie.tif	2011-01-23	335	649	5.8	165.8	897.6	71.328	-155.111
105	2010-11	c20110127_dailyslie.tif	2011-01-27	520	708	6.9	191.1	870.9	71.187	-154.722
106	2012-13	c20130101_dailyslie.tif	2013-01-01	360	511	0.6	12.8	8.7	71.374	-156.561
107	2012-13	c20130106_dailyslie.tif	2013-01-06	7	89	0.9	29.4	26.7	70.700	-159.914
108	2012-13	c20130106_dailyslie.tif	2013-01-06	136	202	0.5	13	5.9	70.825	-159.517
109	2012-13	c20130113_dailyslie.tif	2013-01-13	1799	1936	11.6	164.2	1096.8	69.567	-136.285
110	2012-13	c20130120_dailyslie.tif	2013-01-20	179	258	0.7	36.5	17.1	70.885	-159.126
111	2012-13	c20130217_dailyslie.tif	2013-02-17	260	535	2.8	140.9	609.1	71.069	-157.699
112	2012-13	c20130217_dailyslie.tif	2013-02-17	1610	1806	1.6	180.7	258.8	69.405	-138.282
113	2012-13	c20130221_dailyslie.tif	2013-02-21	251	332	5.7	96.1	513.4	70.958	-157.801
114	2012-13	c20130414_dailyslie.tif	2013-04-14	2	94	1.7	32.1	56.1	70.669	-159.999
115	2013-14	c20140107_dailyslie.tif	2014-01-07	216	299	0.9	75.1	82.1	70.893	-158.125
116	2013-14	c20140115_dailyslie.tif	2014-01-15	54	108	0.4	14.9	7.3	70.740	-159.798
117	2013-14	c20140122_dailyslie.tif	2014-01-22	50	76	0.2	8	1.8	70.699	-159.902
118	2013-14	c20140122_dailyslie.tif	2014-01-22	50	79	0.2	9.5	1.9	70.701	-159.894
119	2013-14	c20140122_dailyslie.tif	2014-01-22	85	114	0.2	5.6	1	70.778	-159.701
120	2013-14	c20140129_dailyslie.tif	2014-01-29	23	56	0.5	12.1	5.6	70.654	-160.021
121	2013-14	c20140129_dailyslie.tif	2014-01-29	109	161	0.5	2.6	1	70.805	-159.633
122	2013-14	c20140205_dailyslie.tif	2014-02-05	1626	1783	0.9	122.2	130.2	69.343	-138.341
123	2013-14	c20140212_dailyslie.tif	2014-02-12	178	248	0.6	25.3	9.8	70.863	-159.304
124	2013-14	c20140216_dailyslie.tif	2014-02-16	1594	1636	1.1	38.5	47	69.607	-139.409
125	2013-14	c20140305_dailyslie.tif	2014-03-05	1636	1777	0.9	98.3	96.4	69.421	-138.464
126	2013-14	c20140316_dailyslie.tif	2014-03-16	90	199	0.7	15.1	11.1	70.817	-159.558

ID	Season	SLIE file	SLIE date	v_0	v_1	W (km)	L (km)	A (km^2)	Latitude	Longitude
127	2013-14	c20140326_dailyslie.tif	2014-03-26	135	269	1	58.1	60.7	70.897	-159.057
128	2013-14	c20140326_dailyslie.tif	2014-03-26	319	464	0.5	39.5	29.8	71.292	-156.864
129	2013-14	c20140327_dailyslie.tif	2014-03-27	42	98	0.7	19	14.7	70.733	-159.885
130	2013-14	c20140402_dailyslie.tif	2014-04-02	1636	1731	0.2	10.9	2.7	69.628	-139.007
131	2013-14	c20140423_dailyslie.tif	2014-04-23	25	96	0.9	24	23.1	70.707	-159.899
132	2013-14	c20140423_dailyslie.tif	2014-04-23	247	369	1.9	118.2	237.5	70.966	-158.030
133	2013-14	c20140427_dailyslie.tif	2014-04-27	52	88	0.5	12.8	5.9	70.719	-159.847
134	2013-14	c20140427_dailyslie.tif	2014-04-27	201	281	0.9	60.2	50.6	70.854	-158.742
135	2013-14	c20140427_dailyslie.tif	2014-04-27	525	939	23.3	399.2	5260.7	71.197	-152.579
136	2013-14	c20140430_dailyslie.tif	2014-04-30	1614	1741	0.7	67.7	50.4	69.609	-139.244
137	2014-15	c20150102_dailyslie.tif	2015-01-02	1417	1560	5.6	114.8	591.1	69.867	-141.797
138	2014-15	c20150115_dailyslie.tif	2015-01-15	1108	1292	5.6	168.7	763.7	70.161	-145.514
139	2014-15	c20150128_dailyslie.tif	2015-01-28	1472	1620	1.5	148.8	187.7	69.748	-141.229
140	2014-15	c20150217_dailyslie.tif	2015-02-17	1137	1173	1.9	26.7	55.4	70.207	-146.179
141	2014-15	c20150218_dailyslie.tif	2015-02-18	1682	1749	1.5	46	64.5	69.555	-138.782
142	2014-15	c20150414_dailyslie.tif	2015-04-14	544	704	10.1	155.2	875.4	71.249	-154.509
143	2014-15	c20150429_dailyslie.tif	2015-04-29	1682	1750	1.2	48.1	56.8	69.543	-138.717
144	2015-16	c20160106_dailyslie.tif	2016-01-06	2	48	0.4	15.8	6.3	70.614	-160.105
145	2015-16	c20160106_dailyslie.tif	2016-01-06	179	261	0.6	40	23.8	70.889	-159.038
146	2015-16	c20160109_dailyslie.tif	2016-01-09	1590	1730	2.1	53.5	142.6	69.618	-139.491
147	2015-16	c20160120_dailyslie.tif	2016-01-20	324	458	0.2	33.9	11.4	71.268	-156.882
148	2015-16	c20160127_dailyslie.tif	2016-01-27	267	317	1	60	57.1	70.932	-157.826
149	2015-16	c20160127_dailyslie.tif	2016-01-27	1526	1592	1.4	78.1	86.2	69.720	-140.509
150	2015-16	c20160212_dailyslie.tif	2016-02-12	258	337	1	93.1	94.1	70.948	-157.723
151	2015-16	c20160330_dailyslie.tif	2016-03-30	178	294	1.9	81.2	163.7	70.893	-158.370
152	2015-16	c20160402_dailyslie.tif	2016-04-02	1	276	1.1	103.5	212.6	70.864	-158.902
153	2015-16	c20160406_dailyslie.tif	2016-04-06	179	221	0.3	11.6	4.1	70.854	-159.323
154	2015-16	c20160406_dailyslie.tif	2016-04-06	1560	1720	0.8	83	55.9	69.655	-139.826
155	2015-16	c20160413_dailyslie.tif	2016-04-13	323	421	0.4	34.7	14.8	71.284	-156.836
156	2015-16	c20160414_dailyslie.tif	2016-04-14	1307	1358	1.1	17.6	14.2	70.172	-143.556
157	2015-16	c20160429_dailyslie.tif	2016-04-29	247	278	6	38.5	203.6	70.885	-158.617
158	2015-16	c20160430_dailyslie.tif	2016-04-30	1573	1636	1.6	61.9	102.2	69.595	-139.663
159	2015-16	c20160430_dailyslie.tif	2016-04-30	1682	1767	1.1	79.8	54.3	69.559	-138.590
160	2016-17	c20170118_dailyslie.tif	2017-01-18	1690	1733	0.3	9.6	2.3	69.624	-138.962
161	2016-17	c20170125_dailyslie.tif	2017-01-25	332	516	0.8	26	16.7	71.351	-156.634
162	2016-17	c20170125_dailyslie.tif	2017-01-25	1637	1734	0.3	12.8	4	69.62188	-138.972
163	2016-17	c20170215_dailyslie.tif	2017-02-15	263	338	2.7	88.1	219.5	71.03411	-157.651
164	2016-17	c20170221_dailyslie.tif	2017-02-21	1	231	1.3	56.9	88	70.70619	-159.934
165	2016-17	c20170221_dailyslie.tif	2017-02-21	260	375	4.9	108.6	576.8	71.05096	-157.522

ID	Season	SLIE file	SLIE date	v_0	v_1	W (km)	L (km)	A (km^2)	Latitude	Longitude
166	2017-18	a20180202_dailyslie.tif	2018-02-02	1360	1437	1.3	25	43.4	70.12016	-142.935
167	2017-18	a20180208_dailyslie.tif	2018-02-08	1669	1813	3.5	159.5	590.4	69.32687	-138.34
168	2017-18	a20180208_dailyslie.tif	2018-02-08	1843	1936	5.4	40.2	115.4	69.59889	-135.729
169	2017-18	a20180212_dailyslie.tif	2018-02-12	374	731	9.2	225.3	1891.6	71.21232	-154.813
170	2017-18	a20180424_dailyslie.tif	2018-04-24	818	1151	13.8	334.4	2723.5	70.69621	-149.606
171	2018-19	a20190106_dailyslie.tif	2019-01-06	440	542	4.4	46.2	206.6	71.41144	-156.084
172	2018-19	a20190114_dailyslie.tif	2019-01-14	1626	1732	0.8	27.1	19.2	69.6123	-139.172
173	2018-19	a20190131_dailyslie.tif	2019-01-31	1480	1574	5.5	100.5	425.5	69.76578	-141.375
174	2018-19	a20190203_dailyslie.tif	2019-02-03	1773	1803	7.4	49.8	298	69.14783	-137.647
175	2018-19	a20190217_dailyslie.tif	2019-02-17	262	338	2.9	89.4	248.3	70.89947	-158.078
176	2018-19	a20190217_dailyslie.tif	2019-02-17	1491	1522	0.9	22.7	16.2	69.83983	-141.881
177	2018-19	a20190314_dailyslie.tif	2019-03-14	425	536	5.6	33	172.7	71.40868	-156.175
178	2018-19	a20190320_dailyslie.tif	2019-03-20	617	671	9.7	98.4	504.9	71.13207	-154.374
179	2018-19	a20190322_dailyslie.tif	2019-03-22	560	617	4.7	17.5	58.2	71.20501	-155.096
180	2018-19	a20190429_dailyslie.tif	2019-04-29	409	538	5.2	35.1	250.7	71.42044	-156.073
181	2019-20	c20200102_dailyslie.tif	2020-01-02	377	617	1.7	84.4	175.3	71.27565	-155.456
182	2019-20	c20200108_dailyslie.tif	2020-01-08	618	652	5.4	62.9	178.3	71.12546	-154.5
183	2019-20	c20200108_dailyslie.tif	2020-01-08	1170	1228	0.8	27.2	25.8	70.14205	-145.659
184	2019-20	c20200109_dailyslie.tif	2020-01-09	523	829	3.7	258.3	689.4	71.07228	-154.106
185	2019-20	c20200311_dailyslie.tif	2020-03-11	1622	1689	0.2	22.4	11.7	69.63173	-139.298
186	2019-20	c20200326_dailyslie.tif	2020-03-26	1404	1506	2.3	77.1	138.9	69.97814	-142.377
187	2019-20	c20200326_dailyslie.tif	2020-03-26	1753	1825	8.4	131.9	713.2	69.30489	-137.658
188	2019-20	c20200405_dailyslie.tif	2020-04-05	847	1633	6	641.5	3405.6	70.33975	-146.682
189	2019-20	c20200405_dailyslie.tif	2020-04-05	1735	1936	17.8	269	2843.4	69.50817	-136.703
190	2020-21	c20210105_dailyslie.tif	2021-01-05	1794	1936	10.4	175.3	910.2	69.57912	-136.321
191	2020-21	c20210114_dailyslie.tif	2021-01-14	324	872	13.2	381.2	3899.7	71.16064	-152.832
192	2020-21	c20210114_dailyslie.tif	2021-01-14	903	1356	18.3	337.4	5153.6	70.41059	-146.211
193	2020-21	c20210114_dailyslie.tif	2021-01-14	1502	1584	2.7	81.9	210.2	69.70953	-141.003
194	2020-21	c20210114_dailyslie.tif	2021-01-14	1502	1622	1.9	112.2	216.2	69.70705	-140.971
195	2020-21	c20210116_dailyslie.tif	2021-01-16	1545	1573	1.4	29.6	42	69.63359	-140.73
196	2020-21	c20210127_dailyslie.tif	2021-01-27	375	470	0.6	1.9	1.5	71.40026	-156.488
197	2022-23	a20230108_dailyslie.tif	2023-01-08	1560	1587	2	28.9	56.2	69.60861	-140.459
198	2022-23	a20230117_dailyslie.tif	2023-01-17	48	96	1	16.3	18	70.73146	-159.846
199	2022-23	a20230214_dailyslie.tif	2023-02-14	1692	1810	13.8	149.6	1822.1	69.36654	-137.983
200	2022-23	a20230215_dailyslie.tif	2023-02-15	597	822	11.6	179	1551.6	71.11189	-153.352
201	2022-23	a20230215_dailyslie.tif	2023-02-15	1765	1791	3.4	41.1	119.9	69.14607	-137.911
202	2022-23	a20230301_dailyslie.tif	2023-03-01	1165	1221	2.8	24.9	43.5	70.19803	-145.862

U.S. Department of the Interior (DOI)

DOI protects and manages the Nation's natural resources and cultural heritage; provides scientific and other information about those resources; and honors the Nation’s trust responsibilities or special commitments to American Indians, Alaska Natives, and affiliated island communities.

Bureau of Ocean Energy Management (BOEM)

BOEM’s mission is to manage development of U.S. Outer Continental Shelf energy and mineral resources in an environmentally and economically responsible way.

BOEM Environmental Studies Program

The mission of the Environmental Studies Program is to provide the information needed to predict, assess, and manage impacts from offshore energy and marine mineral exploration, development, and production activities on human, marine, and coastal environments. The proposal, selection, research, review, collaboration, production, and dissemination of each of BOEM’s Environmental Studies follows the DOI Code of Scientific and Scholarly Conduct, in support of a culture of scientific and professional integrity, as set out in the DOI Departmental Manual (305 DM 3).